Associate Professorship of Molecular Electronics
Department of Electrical and Computer Engineering
Technical University of Munich

Fakultät für Elektrotechnik und Informationstechnik
Professur für Molekularelektronik

Electronic transport studies on hybrid organic-inorganic semiconductor devices on the nanoscale

Simon K. Pfaehler

Vollständiger Abdruck der von der Fakultät für Elektrotechnik und Informationstechnik der Technische Universität München zur Erlangung des akademischen Grades eines
Doktors der Naturwissenschaften (Dr. rer. nat.)
genehmigten Dissertation.

Vorsitzende(r): Prof. Dr. Bernhard Wolfrum
Prüfer der Dissertation:
1. Prof. Dr. Marc Tornow
2. Prof. Dr. Martin Stutzmann

Die Dissertation wurde am 06.05.2019 bei der Technische Universität München eingereicht und durch die Fakultät für Elektrotechnik und Informationstechnik am 15.11.2019 angenommen.

Abstract

Understanding the electronic properties of novel hybrid organic-inorganic nano materials is essential on their way to electrical device applications. In this context, the development of suitable measurement platforms allows their systematic electrical characterization on the nanoscale. In this thesis, we present the fabrication and electrical characterization of all-silicon electrode devices which served as platform to study the electronic properties both, of thin films of functionalized silicon nanocrystals (SiNCs) and of self-assembled monolayers (SAMs) of aromatic organophosphonate molecules. Planar, highly doped silicon (Si) electrodes were fabricated from silicon-on-insulator (SOI) substrates, by either utilizing anisotropic etching in potassium hydroxide (KOH) solution or by the combination of electron beam lithography (EBL) and reactive ion etching (RIE).

Contact separations as small as 30 nm were achieved in case of the electrodes prepared by EBL/RIE based on systematic optimization of etching parameters. The gaps between the electrodes of height 110 nm were filled with thin films of either hexyl- (Hex-), phenyl- (Phen-) or phenylacetylene- (PA-) functionalized SiNCs (diameter 3 nm) from colloidal dispersions, via a pressure-transducing PDMS (polydimethylsiloxane) membrane. This novel approach allowed the formation of homogeneous SiNC films with precise control of their thickness in the range of 15 nm to 90 nm depending on the SiNC solution concentration, without any voids or cracks. X-ray photoelectron spectroscopy (XPS) measurements showed a constant relative Si/Carbon ratio for all investigated film thicknesses and almost no oxidation of the SiNCs after film preparation. The measured conductance of the highly resistive SiNC films at high bias voltages up to 60 V scaled approximately linearly with gap width (5 to 50 μm) and gap filling height, with little device-to-device variance. We attribute the observed, pronounced hysteretic current-voltage (I-V) characteristics to space-charge-limited current transport (SCLC), which - after about twenty cycles - eventually blocked the current almost completely. Numerical kinetic Monte Carlo (kMC) simulations matched the experimental I-V data well for randomly distributed, energetically deep lying trap states with a trap density in the order of $1 \times 10^{17}\,\mathrm{cm}^{-3}$ in the SiNC film. Charge transport was described by a hopping process of the charge carriers between adjacent, weakly bound SiNCs by employing the Miller-Abrahams hopping rate. Additional impedance measurements on planar, SiNC coated highly doped Si samples were realized by a hanging mercury droplet electrode. For Hex-SiNC thin films, a relative permittivity of 4.43 was determined by modeling the impedance data with an equivalent network of resistor-capacitor circuits, indicating a rather close packing of the SiNCs in the film with an estimated volume

fraction of 0.73.

Besides SiNCs, we coated the nanogaps with SAMs of 2-phosphono-9,10-diphenyl-anthracene (PAphenyl) molecules. Water contact angle (CA) and atomic force microscopy (AFM) measurements on planar SAM coated Si/SiO_2 reference samples revealed a uniform and dense monolayer with a thickness of (1.22 ± 0.34) nm obtained by an AFM nanolithography scratching method. Lateral conductance was greatly improved compared to an untreated device, and distinct field-effect induced modulation of the source drain current was observed for negative gate voltages which indicated p-type transport supported by finite element simulations of the electrostatic characteristics of the nanogap. A first estimation of the mobility in the order of $1 \times 10^{-4}\,cm^2/Vs$ for SAMs of PAphenyl was obtained.
The gaps fabricated by KOH, with accomplished contact separations in the range of 200 nm, were coated with SAMs of 2,6-diphosphono-9,10-dianthracene anthracene (PAanthrac) and 1-hexadecanephosphonic acid (PAC16) molecules. SAM characterization by CA, AFM and ellipsometry measurements revealed uniform and dense SAMs accordingly, with a measured thickness of (1.12 ± 0.22) nm for the PAanthrac SAM. The theoretical length of the PAanthrac molecule in gas phase was determined as 1.29 nm by ab-initio calculations based on density functional theory (DFT). The DFT simulations additionally revealed the anthracene sidegroups of the molecule to be rotated by $\sim 90°$ with respect to the molecule backbone and that the highest occupied molecular orbital (HOMO) is mainly located at these sidegroups. The corresponding HOMO-LUMO gap (LUMO: lowest unoccupied molecular orbital) was calculated as 3.05 eV. Electrical *I-V* characterization showed a significantly increased lateral conductance of PAanthrac SAMs compared to PAC16 SAMs as well as to the empty (as-fabricated) gap, possibly due to the efficient overlap of the aromatic anthracene side groups of adjacent molecules.
We propose our demonstrated device scheme as prototype for charge transport investigations of novel hybrid materials at the nanoscale, involving all-silicon contact electrodes.

Zusammenfassung

Das grundlegende Verständnis der elektronischen Eigenschaften neuartiger hybrider organisch-anorganischer Nanomaterialien ist unerlässlich mit Blick auf deren zukünftige Verwendung in neuartigen elektrischen Bauelementen. In diesem Zusammenhang ermöglicht die Entwicklung geeigneter Messplattformen deren systematische elektrische Charakterisierung im Nanobereich.

In dieser Arbeit stellen wir die Herstellung und elektrische Charakterisierung von Siliziumelektroden vor, die als Plattform zur Untersuchung der elektronischen Eigenschaften von dünnen Schichten funktionalisierter Silizium-Nanokristalle (SiNCs) und von sich selbst organisierenden Monolagen (SAMs) von aromatischen Organophosphonatmolekülen dienen. Planare, hochdotierte Silizium (Si) Elektroden wurden aus Silizium-auf-Isolator (SOI) Substraten hergestellt, entweder durch anisotropes Ätzen in Kaliumhydroxid (KOH) Lösung oder durch die Kombination von Elektronenstrahlithographie (EBL) und reaktivem Ionenätzen (RIE). Kontaktabstände von bis zu 30 nm wurden durch Optimierung der Ätzparameter erreicht.

Die Gräben zwischen den Elektroden wurden mit dünnen Filmen aus Hexyl- (Hex-), Phenyl- (Phen-) oder Phenylacetylen- (PA-) funktionalisierten SiNCs (Durchmesser: 3 nm) aus kolloidalen Dispersionen über eine druckübertragende PDMS (Polydimethylsiloxan) Membran gefüllt. Dieser neuartige Ansatz ermöglichte die Bildung homogener SiNC Schichten mit exakter Kontrolle ihrer Dicken (15-90 nm), ohne Hohlräume oder Risse. Röntgenphotoelektronenspektroskopie (XPS) Messungen zeigten ein konstantes relatives Si/Kohlenstoff Verhältnis für alle Schichtdicken und nahezu keine Oxidation der SiNCs. Die Leitfähigkeit der hochohmigen SiNC Schichten skalierte in etwa linear mit der Grabenbreite und der Füllhöhe. Wir führen die beobachteten hysteretischen Strom-Spannungs Messungen (I-V) auf einen Raumladungsbegrenzten Stromtransport (SCLC) zurück, der den Strom schließlich fast vollständig blockierte. Numerische kinetische Monte Carlo (kMC) Simulationen stimmten gut mit den experimentellen I-V Daten überein unter der Annahme von zufällig verteilten, energetisch tief liegenden Störstellen mit einer Dichte von ca. $1 \times 10^{17}\,\mathrm{cm}^{-3}$. Der Ladungstransport wurde dabei durch einen Sprungprozess der Ladungsträger zwischen benachbarten, schwach gebundenen SiNCs beschrieben. Impedanzmessungen an planaren, SiNC beschichteten, hochdotierten Si Proben wurden mit einer Quecksilbertropfen Elektrode durchgeführt. Für Hex-SiNC Schichten wurde eine relative Dielektrizitätskonstante von $4,43$ bestimmt, was auf eine recht enge Packungsdichte der SiNC hinweist.

Neben SiNCs haben wir die Si Elektroden mit SAMs bestehend aus 2-Phosphono-9,10-diphenylanthracen (PAphenyl) Molekülen beschichtet. Charakterisierungsmessungen ergaben eine gleichmäßige und dichte Monolage mit einer Dicke von $(1,22 \pm 0,34)$ nm. Die laterale Leitfähigkeit wurde im Vergleich zu unbehandelten Elektroden stark verbessert, und es wurde eine ausgeprägte durch Feldeffekt induzierte Modulation des Stroms bei negativer Gatter Spannung beobachtet, die auf einen p-Typ Transport hindeutet. Die Mobilität wurde dabei auf $1 \times 10^{-4}\,\mathrm{cm}^2/\mathrm{Vs}$ für SAMs aus PAphenyl geschätzt.
Die mit Hilfe von KOH hergestellten Elektroden wurden mit SAMs bestehend aus 2,6-Diphosphono-9,10-dianthracen-Anthracen (PAanthrac) und 1-Hexadecanphosphonsäure (PAC16) Molekülen beschichtet. Die SAM Dicke betrug $(1,12 \pm 0,22)$ nm für PAanthrac SAMs. Ergänzende Simulationen auf der Grundlage der Dichtefunktionaltheorie (DFT) ergaben, dass die Anthracen-Seitengruppen um 90° verdreht sind, bezogen auf das Molekülgerüst und das sich dort hauptsächlich das höchstbesetzte Molekülorbital (HOMO) befindet. Die elektrische Charakterisierung zeigte eine signifikant erhöhte Leitfähigkeit von PAanthrac SAMs im Vergleich zu PAC16 SAMs sowie zu den leeren Gräben, möglicherweise aufgrund der effizienten Überlappung der aromatischen Anthracen Seitengruppen benachbarter Moleküle.

Wir schlagen unser demonstrierten Si Elektroden als Prototyp für Ladungstransportuntersuchungen neuartiger hybrider Materialien im Nanobereich vor.

Contents

List of abbreviations

I-V	current-voltage
AC	alternating current
AFM	atomic force microscopy
Al	aluminium
Au	gold
B3LYP	Becke, three-parameter, Lee-Yang-Parr
CA	contact angle
CAD	computer-aided design
CCP	capacitively coupled plasma
CGME	controlled growth mercury electrode
Cr	chromium
DC	direct current
DFT	density functional theory
DI Water	deionized water
DUT	device under test
ebeam	electron beam
EBL	electron-beam lithography
FET	field-effect transistor
FTIR	Fourier-Transform Infrared
Hex-SiNC	hexyl functionalized silicon nano crystal
HF	hydrogen fluoride

HMDS	hexamethyldisilazane
HOMO	highest occupied molecular orbital
HSQ	hydrogen silsesquioxane
ICP	inductively coupled plasma
ICP-RIE	inductively coupled plasma reactive ion etching
kMC	kinetic Monte Carlo
KOH	potassium hydroxide
LUMO	lowest unoccupied molecular orbital
MA	Miller-Abrahams
MOSFET	metal oxide semiconductor field-effect transistor
NC	nano crystal
OFET	organic field-effect transistor
P3HT	poly(3-hexylthiophene)
PA-SiNC	phenylacetylene functionalized silicon nano crystal
PAanthrac	2,6-diphosphono-9,10-dianthracene anthracene
PAC16	1-hexadecanphosphonic acid
PAphenyl	2-phosphono-9,10-diphenyl-anthracene
PDMS	polydimethylsiloxane
Phen-SiNC	phenyl functionalized silicon nano crystal
PL	photoluminescence
PVD	physical vapor deposition
RF	radio frequency
RIE	reactive ion etching
RMS	root mean square
SAM	self-assembled monolayer
SEM	scanning electron microscopy

Si	silicon
SiNC	silicon nano crystal
SiO_2	silicon dioxide
SMU	source measure unit
SOI	silicon-on-insulator
SPL	single pixel line
T-BAG	Tethering By Aggregation and Growth
TEM	Transmission electron microscopy
THF	tetrahydrofuran
Ti	titanium
TiO_2	titanium dioxide
TiO_x	titanium oxide
TLM	transmission line model
TMAH	tetramethylammonium hydroxide
TOPO	trioctylphosphine oxide
XPS	x-ray photoelectron spectroscopy

1 Introduction

The miniaturization of electronic devices in semiconductor technology is still ongoing and has reached dimensions in the range of $\sim 10\,\mathrm{nm}$ up to now. This development is characterized by an empirical description of Gordon Moore which predicts that the device density in integrated circuits would double roughly every one and a half year [1]. Until now, this prediction holds quite well. However, it is clear that the continuous down scaling will eventually lead to fundamental limits. That is why new approaches and new technologies are necessary which may not replace directly the existing bulk silicon based microtechnology, but rather complement it for specialized purposes. Technologies beyond classical Si technology such as flexible, or transparent electronics can offer completely new use cases which are likely impossible to cover by conventional Si technology only. New devices like flexible screens or wearable electronics [2] are appealing ideas which offer the possibility for, e.g., sensors to be placed directly on the skin [3] or printable electronics which can even be realized directly on paper [4].
One major advantage of most of these techniques is, that they are not based on energy intensive top-down fabrication processes but on processing from solutions. As a result, cost savings are likely if fabrication processes such as roll-to-roll are possible.

In this context, new materials are extensively studied, ranging from fundamental studies on the electrical transport phenomena as well towards future applications. One widely investigated material class are semiconducting nanocrystals (NCs) [5]. Among a huge variety of different materials, the most prominently studied semiconductor NC systems are compound systems based on either group III-V (e.g. InP and GaAs), II-VI (e.g. CdSe and CdTe), or IV-VI (e.g. PbS and PbSe) materials both, for fundamental research on nanocrystals as well as for different applications such as solar cells [6–8], LEDs [9–11], lasers [12–14], sensors [15–17] and fluorescent labels [18–20].
However, these materials have several disadvantages since they contain either rare materials such as, e.g., indium and selenium or some of them contain toxic heavy metals as, e.g., arsenic, cadmium or lead. That is why there is an increasing effort to replace these materials by non-toxic, abundant alternatives. Additionally, the utilization of some of these materials is already banned from consumer products by law due to their toxicity. In the European Union the Restriction of Hazardous Substances directive limits, e.g., the lead and cadmium content to a maximum of $0.1\,\mathrm{wt.\,\%}$ [21].
Among the variety of semiconductor materials under investigation, Si has adopted a particular

role due to its dominating relevance in microelectronics, its abundance and low toxicity [22]. Silicon nanocrystals (SiNCs) show distinct optical properties such as size-tunable photoluminescence (PL) in the visible range with high quantum yields when their size is reduced below the Bohr radius of Si ($d < 5\,\mathrm{nm}$) [23–25]. For this reason, photoluminescent SiNCs have evolved as promising material for electronic and optoelectronic applications. In order to prevent oxidation of the SiNC surface as well as to control their (opto-) electronic properties, a well-tailored surface functionalization is essential [26, 27]. Methods to synthesize SiNCs and functionalize their surfaces with a variety of different molecules are well developed [28, 29], as predominantly demonstrated in optical studies [30–32]. For electrical device applications covering for example novel (ultra) thin film transistors, sensors or non-volatile memories, based on hybrid inorganic-organic 2D or 3D networks of functionalized SiNCs, the characterization and understanding of their electronic transport properties is mandatory [33, 34]. There are several studies about the electrical characterization of networks of either hydrogen-terminated SiNCs or oxidized SiNCs [35–42] but only a few reports about the electrical characterization of functionalized SiNCs, mostly focusing on alkyl-functionalized, doped SiNC networks, exist [43].

Besides NCs, another widely studied material class in the context of novel electronic devices are semiconducting organic molecules. There are early reports about conductivity in organic molecules already from the beginning of the last century, but this topic came into major focus starting from the $1950's$ [44, 45]. There is a huge class of well-known organic molecule material systems which are well studied and used in device applications, such as thin films of anthracene, pentacene or poly(3-hexylthiophene) (P3HT) and other related polymer molecules. These molecules have been widely studied in, e.g., transistor devices [46–49]. In such organic field effect transistors (OFET), the major contribution to the charge transport takes place in close vicinity of the gate dielectric, namely within the first two monolayers [50]. In this sense, the realization of a device with only one monolayer as active channel is the ultimate miniaturization of an OFET [51]. One approach to realize such a device is to employ self-assembled monolayers (SAMs) which intrinsically consists of only one molecular layer. This provides the possibility of controlling the channel thickness to molecular dimensions. At the same time, the high degree of molecular order in such SAMs may potentially lead to higher charge carrier mobilities compared to traditional (polycrystalline) organic thin films. Such self-assembled monolayer field effect transistors (SAMFETs) based on, e.g., aromatic silanes have been the subject of several recent studies [52, 53]. Due to their low temperature fabrication process, SAMFET devices offer the opportunity of low cost production and large area applications on rigid as well as on flexible substrates [54, 55]. Additionally, they may provide the basis for novel sensing devices since its chemical behavior can be well controlled [56].
Interesting molecules that may serve as precursors for SAM formation are organophosphonic acids [57]. They form well–ordered, strongly bound films (organophosphonate SAMs) with

molecular densities close to those found in single crystals [58]. Additionally, they offer a similar quality as thiol-based SAMs on gold but bind to many different oxide types (AgO, Al_2O_3, ITO, SiO_2, etc.) [59] which makes them excellent candidates for different applications in organic electronics [60]. This includes in particular SAMFET devices to be directly incorporated into silicon technology based integrated circuitry. Device architectures with channel length below the average domain size of 2D-crystalline SAM areas are expected to reveal enhanced transistor characteristics. Such phosphonates have previously found application, for example for the growth of three-dimensional, stacked multilayer structures, or as efficient attenuating layers for tunneling currents [61, 62].

In order to study the electrical properties of either thin films of SiNCs or organophosphonate SAMs, a suitable test system is needed. The systematic investigation of undoped functionalized SiNCs poses a particular challenge on the experimental realization: 1) Due to the high resistance of the SiNCs films, the spacing between the electrical contacts needs to be small (100 nm regime), 2) The space between the contacts (gap) needs to be filled with the SiNC material in a controlled, homogeneous and reproducible manner, and 3) the electrode contact material has to be inert, both chemically and physically with respect to the high electric fields that need to be applied.
For SAMs based on organophosphonate molecules, similar considerations are valid.
There are several approaches in the literature to study hybrid organic materials or molecules on the nanoscale, e.g., mechanical break junctions [63, 64], nanogaps formed by metal electromigration [65], scanning tunneling microscopy [63] or vertical [66] as well as lateral nanogap electrodes [67] and several more [68]. Most of these techniques use metal electrodes which may suffer from artifacts arising from, e.g., electromigration of metal ions from the contacts into the film [69]. Unlike commonly employed metals, semiconductors offer a wider range towards tailored electronic properties, by choice of material, doping concentration and doping polarity. This way, an optimal matching of energy levels between contact and molecular system may be achieved. One strategy to integrate, e.g., SAMFETs seamlessly with silicon micro-technology is to use the silicon, itself, to contact directly to the organic monolayer [66, 70–72].
Thus, silicon nanogap electrode devices are a promising platform to study both, thin films of SiNCs as well as organophosphonate SAMs.

This thesis is structured as follows:
Chapter 2 gives a brief introduction about the main theoretical aspects of charge transport related to Si nanocrystal networks as well as to charge transport in organic thin films.
In **Chapter 3**, an overview about the employed materials in this work as well about the main fabrication and characterization techniques used in the course of this work is given.
Chapter 4 describes the fabrication process of silicon-on-insulator (SOI) based nanogap electrode devices fabricated by either anisotropically etching in potassium hydroxide (KOH) solution

or by a combination of electron beam lithography (EBL) and reactive ion etching (RIE). The last section of the chapter describes in detail the outcome of several different coating methods, which were investigated with the aim of reliably filling the fabricated nanogap devices with thin films of functionalized SiNCs. This includes spin coating, drop casting, vertical evaporation and a novel membrane based coating technique, particularly developed during the course of this thesis.

Chapter 5 covers the electrical characterization of the Si nanogap devices, filled with thin films of functionalized SiNCs. The electrical current-voltage (I-V) measurements are complemented by kinetic Monte Carlo (kMC) simulations of the obtained I-V data to study the underlying charge transport mechanisms in more detail. Additionally, the SiNC thin film composition is studied via X-ray photoelectron spectroscopy (XPS) and impedance measurements.

In **Chapter 6**, the electrical characterization of Si nanogap devices fabricated by both, anisotropically etching in KOH solution as well as by EBL/RIE is reported. They are coated with in total two different SAMs of aromatic organophosphonate molecules. The molecular structure of one molecule is additionally investigated by density functional theory (DFT) simulations. In case of nanogap devices fabricated by EBL/RIE, electrical characterization of the SAMs in field effect operation is reported. For this purpose the electrical characterization of the nanogap devices is complemented with finite element simulations of the electrostatic characteristics under applied gate potential.

Chapter 7 summarizes this work and gives an outlook towards possible future experiments.

2 Theoretical background

2.1 Silicon nanocrystal optical properties

There is a growing interest in SiNCs due to several advantageous inherent properties. First of all, Si is highly abundant unlike many other elements studied as nanocrystals such as, e.g., indium or selenium. Additionally, Si is non-toxic, even in the form of SiNCs [22] which makes them an ideal candidate for life-science applications.
One of the most appealing properties of SiNCs is the fact, that unlike bulk Si, SiNCs show luminescence due to the quantum confinement effect for small SiNCs. The emission properties of SiNCs can be tuned via, e.g., changing the SiNC size, the SiNC shape or the SiNC doping. Dasog *et al.* demonstrated photo-luminescence (PL) of SiNCs in the 3-4 nm (diameter) regime which was tuned from blue to red via the functionalization with dodecylamine, acetal, diphenylamine, trioctylphosphine oxide (TOPO), and dodecyl molecules. The corresponding PL quantum yields were in the range of $\sim$ 20 % and the underlying PL mechanism was studied in detail [73].
Functionalization of the SiNCs with different surface groups can be achieved via a variety of techniques thanks to the well studied chemistry of the Si surface [74]. Successful SiNC functionalization has been realized via e.g. hydrosilylation reactions [75, 76], organolithium reagents [77] or halogenated Si surfaces [78], and other methods.
The PL of the SiNCs can be also tuned by the SiNC size as shown by Ledoux *et al.* [23] for SiNCs of diameter between 2.5 nm to 8 nm. PL followed closely the quantum confinement model with maximum PL quantum yields for SiNCs in the size range of 3 nm to 4 nm.

One additional advantage of SiNCs is the fact that they are in principle compatible with the existing Si micro-fabrication processes and technologies which is beneficial towards future application and integrated device development.

2.2 Charge transport in semiconductor nanocrystal networks

Unlike charge transport in inorganic semiconductors, there is no commonly accepted, complete theory which covers all different aspects of charge transport in disordered, hybrid inorganic/organic systems such as SiNC networks. There are several charge transport models (e.g. space charge limited, trap limited, hopping transport, Fowler-Nordheim tunneling, Pool-Frenkel con-

duction etc.) which can describe these systems in various regimes. A detailed discussion of these processes can be found, e.g., in the book of Köhler and Bässler [79]. In the following sections, the main aspects of the corresponding models will be introduced, as related to the discussion of the experimental data.

2.2.1 Charge injection mechanisms

Since the NCs are undoped in this work, all mobile charge carriers need to be injected from the electrodes to the NC film. The key parameter which controls mainly the injection is the height of the barrier between electrode and NC film. This barrier needs to be overcome by the injected charge carriers, either by thermal activation or by tunneling. The barrier height is mainly determined by the difference in the work-functions of the materials. There are several charge injection mechanism known, two of them are briefly presented in the following.

Fowler-Nordheim tunneling

In the presence of a strong electric field, the barrier exhibits a triangular shape instead of a rectangular one. Thus, charge carriers can tunnel through this barrier at an enhanced tunnel rate since the effective barrier thickness is decreased because of the changed shape. The injection current density j depends therefore on the applied electric field F [79]:

$$j_{\mathrm{FN}} \cong F^2 \exp\left(-\frac{4\sqrt{2m_{\mathrm{eff}}\Phi^3}}{3\hbar eF}\right) \tag{2.1}$$

where m_{eff} is the effective mass of the charge carrier, Φ the barrier height, $\hbar$ the reduced Planck constant and e the elementary charge.

Richardson-Schottky thermionic injection

For the Richardson-Schottky thermionic injection, a charge carrier gets thermally excited from the Fermi level of the electrode material. This charge induces an image charge at an equal distance at the opposite side of the barrier which lowers eventually the barrier. As a result the charge carrier can overcome the barrier and will be injected in the transport material.

$$j_{\mathrm{RS}} = T^2 \exp\left(-\frac{\Phi - E_a - \sqrt{Fe^3/\pi\varepsilon_0\varepsilon_r}}{k_B T}\right) \tag{2.2}$$

with temperature T, electron affinity of the transport material (semiconductor) E_a, ε_r the relative permittivity of the material, ε_0 is the vacuum permittivity and k_B the Boltzmann constant.

2.2.2 Space charge limited current

If the current is not limited by injection effects at the electrodes, it is the charge transport material itself which ultimately limits the current. The total charge carried by all charge carriers traversing the material builds up a space charge. This space charge shields the external electric field which is applied between the injecting electrodes. As a consequence, the external field is attenuated and hence charge transport is limited by the charge carriers themselves. This mechanism is known as space charge limited current (SCLC) transport. It is expressed by the Mott-Gurney equation or Child's law [79]:

$$j = \frac{9}{8}\varepsilon_r \varepsilon_0 \mu \frac{V^2}{l^3} \tag{2.3}$$

Here, ε_r is the relative permittivity of the material, ε_0 is the vacuum permittivity, μ the mobility of the charge carriers, V the applied voltage and l the distance between the electrodes which enclose the active material.
Equation 2.3 is only valid for materials without any traps. This is in most cases not realistic, most disordered systems such as NC films contain usually a substantial amount of trap sites. In this case, μ is rather an effective mobility which depends on the trap density and their energy levels in the material. If the energy levels of all trap states are equal, then the main relation of Equation 2.3 still holds. However, this is almost certainly not the case for disordered systems such as NC films which are expected to rather show a distribution of energies for the trap states. In case of an exponential distribution of the trap energies, it can be expressed as [80]:

$$n(E_t) = \frac{N_t}{k_B T_c} \exp\left(-\frac{E_t}{kT_c}\right) \tag{2.4}$$

where T_c is related to the steepness of the distribution, N_t is the total density of traps, k_B is the Boltzmann constant and E_t is the energy level of the traps. For such a distribution, it was shown that the general dependence of j can be expressed as

$$j(V) \propto \frac{V^{k+1}}{k^{2k+1}} \tag{2.5}$$

with

$$k = \frac{T_c}{T} > 1 \tag{2.6}$$

where T is the temperature. As a consequence, j increases faster with increasing V compared to the Mott-Gurney equation without traps. For other energy trap distributions besides the discussed exponential one, as e.g. Gaussian trap distributions, there is no exact solution and j needs to be solved numerically.

2.2.3 Hopping transport

NCs in disordered films are usually only weakly coupled by e.g. van der Waals forces. Therefore, a band-like transport model can not describe charge transport in these systems. There are most certainly numerous trap states present due to defects in the NCs or at the interface to the organic shell. Additionally, the (small) SiNCs themselves, surrounded by an organic shell, form a potential well with localized states. That means, that charge carriers need to overcome a potential barrier (e.g. the organic shell) by a phonon-assisted process which is called hopping transport. There are several descriptions of the hopping process, for several experimental conditions [81–85]. Disordered systems are mostly described with an incoherent hopping process which takes static energy disorder into account. That means, if a charge carrier gains energy ΔE_{ij} while jumping from site i to an adjacent site j, the jump back would require energy. This scenario is frequently described through the Miller-Abrahams (MA) hopping rate [85]:

$$a_{ij}^{\text{hop}} = a_0 \exp\left(-2\gamma r_{ij}\right) \begin{cases} 1 \quad \text{for} \quad \Delta E_{ij} \leq 0 \\ \exp\left(-\frac{\Delta E_{ij}}{k_B T}\right) \text{ for } \Delta E_{ij} > 0 \end{cases} , \tag{2.7}$$

with the hopping prefactor a_0, the inverse of the localization length γ, Boltzmann constant k_B, and the jump distance r_{ij}.
We use this hopping rate in the kinetic Monte Carlo (kMC) simulations in Section 5.3.

2.3 Charge transport in organic thin films

In the following the main aspects of charge transport in molecules and organic films are briefly discussed. A detailed discussion can be found in [79] or [86].

2.3.1 Conjugated organic molecules

An organic molecule contains per definition carbon atoms which usually act as the backbone of the organic molecule. A single carbon atom has 6 electrons which fill the atomic orbitals according to the well known electron configuration of carbon atoms with a maximum of 2 electrons of opposite spin per orbital according to the Pauli principle: $1s^2 2s^2 2p_x^1 2p_y^1$. The shape and energy levels of the orbitals are determined by solving Schrödinger's equation for the electron wave function Ψ. The probability density $|\Psi|^2$ is then a measure of the location of the corresponding electron. The resulting shape for the s- and p-orbitals is schematically depicted in Fig. 2.1(a) (s-orbital) and (b) (p_z-orbital). The s-orbital is spherically symmetric, whereas the p-orbital is dumb-bell shaped. Since the p-orbital is not spherically symmetric, there are 3 different variants, p_x, p_y and p_z, one alongside each space coordinate.
However, if carbon atoms bond to each other or to different atoms while forming a molecule, the description of the new molecule by the single atom orbitals loses its validity. For carbon in this

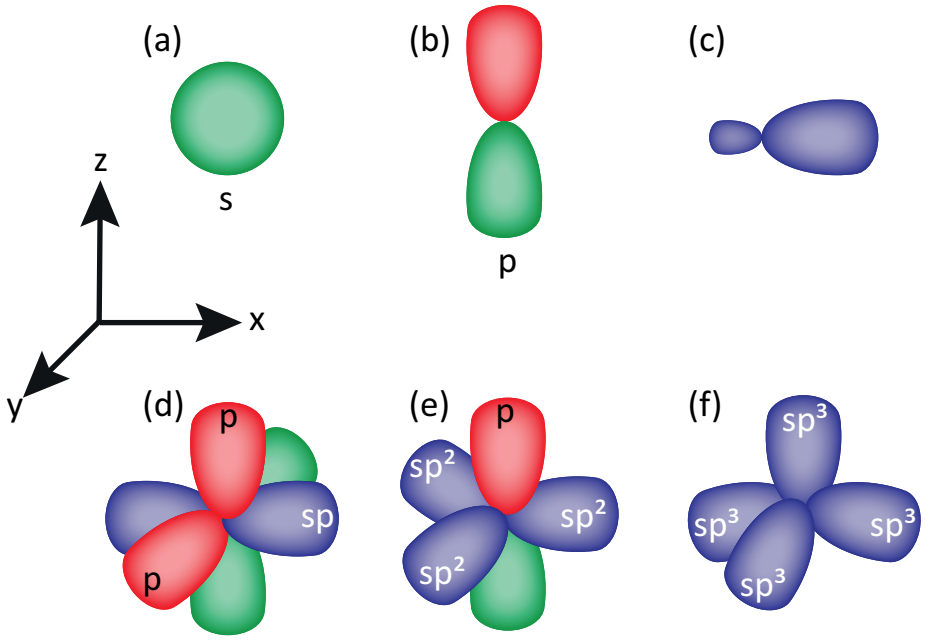

Figure 2.1 Sketch of the geometrical shape of different orbitals. The red/green orbitals represent the unchanged atomic orbitals and the blue orbitals are the hybrid orbitals. (a) s-orbital; (b) p_z-orbital; (c) hybridization of s- and p-orbital; (d) spatial arrangement of hybrid sp-orbitals; (e) spatial arrangement of hybrid sp^2 orbitals and (f) spatial arrangement of sp^3 orbitals.

case, it is energetically more favorable to generate new orbitals by mixing the existing s- and p-orbitals. This process is called hybridization. The energy level of the new hybrid orbitals is between those of the original s- and p-orbitals. The shape of such a hybrid sp-orbital has a distorted dumb-bell form as schematically shown in Fig. 2.1(c). If only one of the three p-orbitals (e.g. p_x) is mixed with the s-orbital, two hybrid sp-orbitals are formed, while leaving the other two p-orbitals (p_y, p_z) unchanged. If two p-orbitals participate in the hybridization process, there are three sp^2 hybrid orbitals and one unchanged p_z orbital. If finally all three p-orbitals mix with the s-orbital, they are transformed into 4 hybrid sp^3 orbitals. The hybridization of the orbitals has important consequences for the spatial distribution of the orbitals and as a consequence also for the bonding process while forming molecules. All orbitals will maximize their distance to each other to achieve the energetical most favorable state. Fig. 2.1(d)-(f) shows the spatial distribution for all three hybridization cases: the two sp-orbitals will arrange themselves in opposite direction, enclosing an angle of 180° to each other while standing perpendicular to the plane of the remaining two p-orbitals (p_y, p_z) (d). The three sp^2 orbitals lie in one plane while enclosing an angle of 120°, respectively. The non-hybrid orbital p_z stands perpendicular to this plane (e). In case of the sp^3 hybridization, there are only hybrid orbitals available. Thus,

the energetically best distribution of the orbitals is a tetrahedral arrangement, where all sp^3 orbitals enclose an angle of 109.5° to each other.

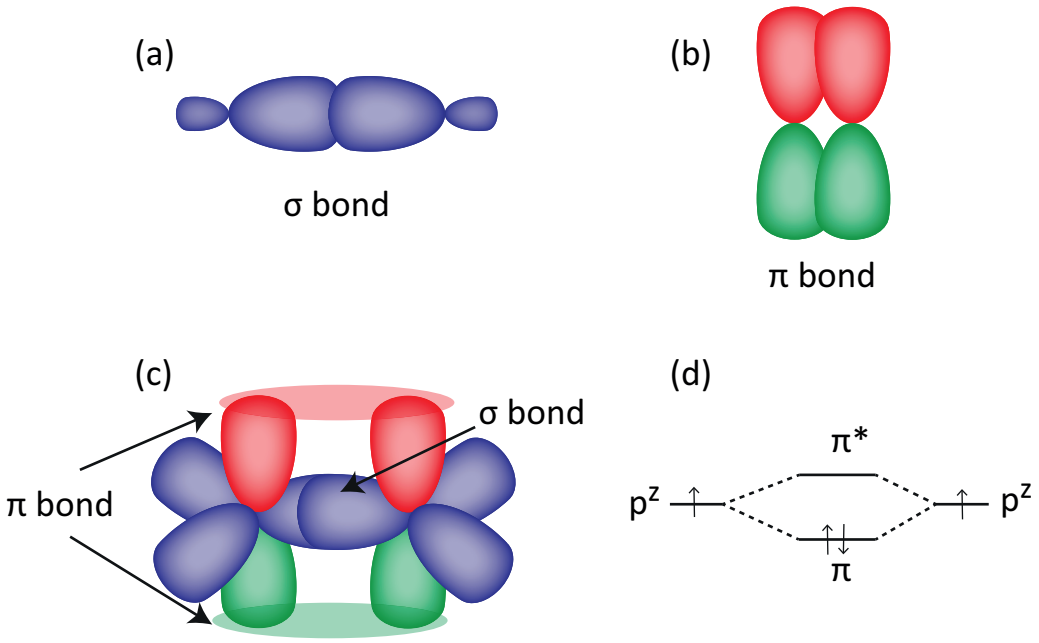

Figure 2.2 Schematic of (a) σ-bond and (b) π-bond. (c) Structure of a double carbon bond in ethene and (d) the corresponding molecular orbital diagram for the p_z orbitals.

In principle there are two major bonding types present in organic molecules. If the (hybrid) orbitals bond along their major geometrical axis, a so called σ-bond is formed as depicted in Fig. 2.2(a) for the case of two hybrid orbitals. Because of its spherical geometry, this is the only possible bond type if an s-orbital is involved. For non-spherically symmetric orbitals, as e.g. the hybrid orbitals, there is a second bond type possible, the π-bond. In this case, the bond is between the parallel main axis of the corresponding orbitals as shown in Fig. 2.2(b). Generally, the σ-bond is the stronger bond compared to the π-bond. If carbon forms a double bond two a second carbon atom in a molecule, the first bond is a σ-bond and the second one is a π-bond. Organic molecules consist often of a sequence of carbon atoms which alternately bond with one or two bonds to each other. The carbon atoms in these so-called conjugated molecules have therefore 3 σ-bonds and are thus sp^2 hybridized. Fig. 2.2(c) shows the example of the simple molecule ethene which has two carbon atoms which are double bonded: the first bond is a σ-bond between the sp^2 orbitals, one of each carbon atom. This bond is rather strong and keeps the molecule together. Due to the large overlap of the corresponding orbitals the resulting splitting of the energy levels is large. The second bond is a π-bond between the not hybridized p_z which are oriented perpendicular to the plane of the sp^2 orbitals. Because of this geometry, the overlap of the p_z is not as large as for the σ-bond and as a consequence, the energy splitting of the corresponding levels is less. Because of this weaker bonding and because of the

alternating structure of the double bonds, the electrons can move between the atoms and are therefore delocalized. This delocalization is the origin of (semi)conducting organic molecules. The energy levels of the molecular orbitals can be calculated via a variety of methods such as the valence-bond (VB) method or density functional theory (DFT). For larger molecules this can be only solved numerically. One common approach is to calculate the molecular orbitals by the linear combination of atomic orbitals (LCAO) method. According to LCAO, molecular orbitals can be classified in bonding orbitals with lower energies and antibonding orbitals with higher energies. The corresponding schematic of the molecular orbital diagram of the p_z orbitals (in case of ethene) is shown in Fig. 2.2(d). The π-bond leads to an occupied molecular bonding π orbital and a corresponding unoccupied molecular $\pi^\star$ orbital. Since the π orbital is the energetic highest occupied molecular orbital this is referred to as HOMO. On the other side the $\pi^\star$ orbital is referred to as the lowest unoccupied molecular orbital (LUMO). These two molecular orbitals largely determine the electronic properties of the molecule and are therefore often seen in analogy to the conduction and valence band in inorganic semiconductors. For cyclic organic molecules such as phenyl or anthracene, the π-bonds lead to delocalized electrons all over the cyclic ring. Such systems are therefore also called π systems and are the main building blocks of electrically active organic molecules.

2.3.2 Self-assembled monolayers

The general aspects of self-assembled monolayers (SAMs) are discussed briefly. A detailed introduction can be found in [87].
SAMs consist of molecules which bond to a substrate typically from solutions via a functional group. The general structure of self-assembling molecule is depicted in Fig. 2.3(a). They consist of a head group which forms a covalent bond to the substrate, a spacer and an end group. Hence, the head group determines to which substrates the molecule can bond. Fig. 2.3(b) schematically shows the process of self-assembly: molecules are bonding via the head group to the substrate. The main driving force of the spontaneous formation of SAMs is the affinity of the head group to bond to the substrate. Due to intermolecular interactions between adjacent molecules and molecule-solvent interactions there is a self-organization of the molecules to achieve the energetically most favorable state. This leads to the highly ordered structure of a SAM. For this reason, the molecules are typically tilted by the tilting angle Θ with respect to the surface normal. As a consequence, the SAM thickness is different from the molecule length.
Fig. 2.3(c) schematically shows the molecules of an organophosphonate SAM bonded to a SiO_2 substrate via two oxygen atoms.

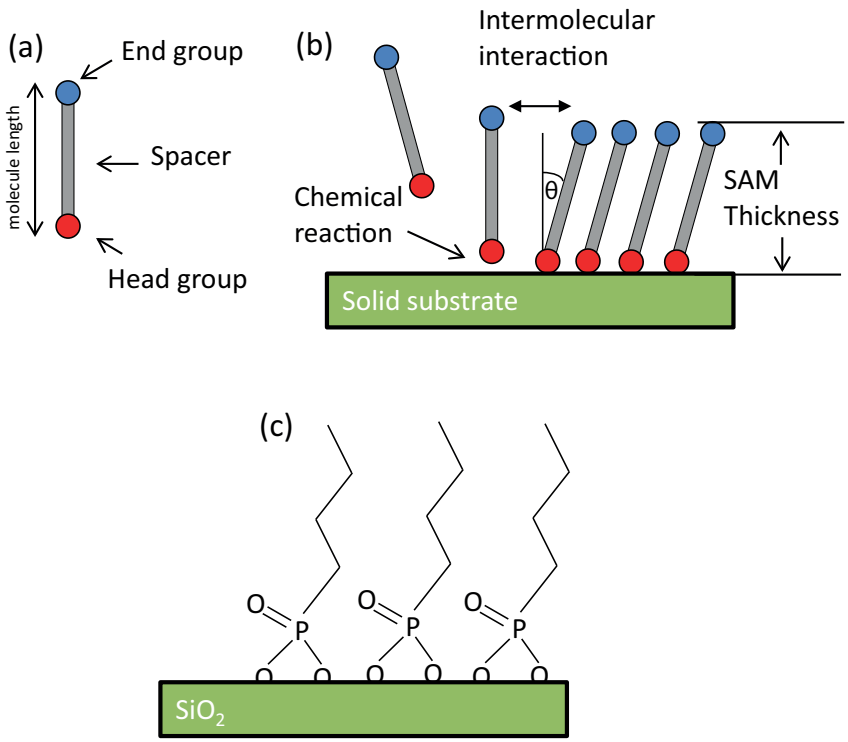

Figure 2.3 (a) Schematic of a molecule used for SAMs. (b) Schematic which shows the self-assmbly process on a solid substrate. Θ is the tilting angle of the corresponding molecules in the SAM. (c) Schematic of organophosphonate molecules forming a SAM on a SiO_2 substrate.

2.3.3 Theory of organic field-effect transistors

In contrast to inorganic field-effect transistors (FET) as e.g. the metal oxide semiconductor FET (MOSFET), organic FETs (OFETs) are operated in a different mode. MOSFETs benefit from a high density of charge carriers which are typically available through doping of the bulk material. The charge carrier density is then modulated by creating depletion zones in the vicinity of the electrodes via the gate potential. A MOSFET is thus operated in inversion mode. The density of free charge carriers is typically low in organic semiconductors since they have a large band gap and are usually undoped. Charge carriers need to be injected from the electrodes and charge carrier density is modulated by accumulating them at the interface to the gate oxide. OFETs are therefore operated in the accumulation mode. A good introduction to the general principles of OFET operation is given in [79, ch. 4.4.1] and [88].
OFETs are characterized electrically by measuring their output characteristics (source-drain current I_{DS} vs. source-drain voltage V_{DS}) at fixed gate voltages V_{GS} and by measuring their transfer characteristics (I_{DS} vs. V_{GS}). The output characteristics of an ideal OFET operated in accumulation regime starts with a linear increase in I_{DS} while increasing V_{DS} if V_{GS} is greater than the corresponding threshold voltage V_{th}: The first injected charge carriers from the electrodes need to fill any charge traps present in the organic semiconductor or at the interface to the gate dielectric before an accumulation layer of mobile charge carriers is created. That means that as long as $V_{DS} < V_{GS} - V_{th}$ (absolute voltages), the linear regime of the output characteristics can be observed. However, if V_{DS} is increased sufficiently ($V_{DS} \approx V_{GS} - V_{th}$), the channel is pinched-off at the drain electrode and a depletion region is formed. Charge carriers are now pulled through the depletion region by the electric field between the pinch-off point and the drain electrode. While increasing V_{DS} further, the pinch-off point is shifted towards the source electrode. The OFET is now operated in the saturation regime, that is, I_{DS} does not change for an increased V_{DS} because I_{DS} is controlled by the potential drop from the source contact to the pinch-off point in the channel which is constant for a fixed V_{GS}.
In the gradual channel approximation (electric field of gate $F_{GS} \gg {}^{V_{DS}}/_{l}$), the I-V relations for the linear and saturation regime are given by:

$$I_{DS,lin} = \frac{w}{l}\mu C\left(V_{GS} - V_{th} - \frac{V_{DS}}{2}\right)V_{DS} \tag{2.8}$$

$$I_{DS,sat} = \frac{w}{2l}\mu C(V_{GS} - V_{th})^2 \tag{2.9}$$

μ is the mobility of the charge carriers and C the gate insulator (SiO_2) capacitance. Equation 2.8 holds for the linear regime and Equation 2.9 holds for the saturation regime.
From the slope g (transconductance)

$$g = \left.\frac{\partial I_{DS}}{\partial V_{GS}}\right|_{V_{DS}} \tag{2.10}$$

of the transfer characteristics in the linear regime, we can then calculate μ

$$\mu = \frac{gl}{WCV_{DS}} \tag{2.11}$$

2.3.4 Charge transport in monolayers

As discussed in Section 2.3.1 charge transport in molecules benefit from a π-system of delocalized electrons. Charge can then be transported via the delocalized charge carriers through the corresponding molecule. Aromatic moieties such as phenyl or anthracene are examples of such π-systems. For lateral charge transport in SAMs, an efficient transport between adjacent molecules is necessary. In principle charge carriers may be transferred from one molecule to the adjacent one by several processes such as hopping or tunneling as discussed in Section 2.2 if the distance of the adjacent molecules is not too far. The packing density and the order of the molecules is therefore a crucial parameter for lateral transport in SAMs. Charge transport can be enhanced through the interaction of π-systems of adjacent molecules [89]. These interactions can lead to a splitting of the HOMO and LUMO levels depending on the inter molecular distance [90–92]. The splitting is dominant for the interaction of overlapping π-systems as e.g. phenyl rings. For an ideal dense and ordered SAM consisting of molecules with aromatic moieties, this π-π stacking may lead to the formation of HOMO/LUMO bands similar to bands in inorganic semiconductors [93]. However, the exact nature of the π-interactions depends on the specific molecular situation [94]. In real SAMs, there are often defects, grain boundaries or variations in the packing density present which impairs charge transport. In real devices, charge transport might be therefore rather a combination of delocalized charge carriers and hopping/tunneling processes over existing barriers which depend on the SAM quality.

3 Materials and Methods

In this chapter, all materials, fabrication techniques and major characterization methods are introduced which were employed during this work.

3.1 Materials

3.1.1 Silicon-on-insulator wafer

The starting wafer material for the fabrication of all Si nanogap electrodes in this work was silicon-on-insulator (SOI). Generally, a SOI wafer consists of a Si device layer at the top separated by a buried silicon dioxide (SiO_2) layer from the Si handle wafer at the bottom. In this work, SOI wafers with two different specifications were used. For the fabrication of nanogap samples by reactive ion etching (RIE) as described in Section 4.2, we used a SOI wafer from *Soitec, France* with a $d = (110.0 \pm 7.5)$ nm thick Si device layer (100) and a (200 ± 5) nm thick buried SiO_2 layer (Fig. 3.1(a)). While the Si top layer and the Si handle wafer were originally p-doped (Boron, resistivity ca. $15\,\Omega\,\mathrm{cm}$), the top Si layer was additionally heavily p-doped by ion implantation (p^+, Boron, doping concentration ca. $5 \times 10^{19}\,\mathrm{cm}^{-3}$).
The second SOI wafer material (*Si-Mat, Germany*) was used for all nanogap samples fabricated by anisotropically etching in KOH (cf. Section 4.1). As schematically shown in Fig. 3.1(b), it consists of a $d = (3.0 \pm 0.5)$ µm thick Si device layer (100) and a (8.0 ± 0.4) nm thin buried SiO_2 layer. The Si device layer (100) as well as the Si handle wafer were analogously highly p-doped (Boron, $9 \times 10^{18}\,\mathrm{cm}^{-3}$).

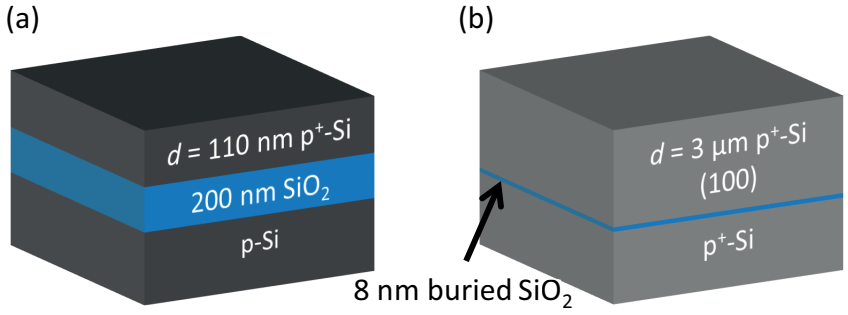

Figure 3.1 Schematic showing the silicon-on-insulator (SOI) wafer material used for the fabrication of Si nanogap samples by (a) RIE and by (b) anisotropically etching in KOH.

3.1.2 Functionalized silicon nanocrystals

All functionalized SiNCs used in this work were provided by Dr. Arzu Angı and Marc Kloberg from the Wacker-Chair of Macromulecular Chemistry (TUM, Prof. Bernhard Rieger) in the framework of the "Alberta/Technical University of Munich International Graduate School for Funcional Hybrid Materials (ATUMS)" collaboration.
The electrical characterization of thin films of SiNCs presented in this work focused mainly on SiNCs whose surfaces are functionalized with hexyl groups (Hex-SiNCs) as schematically depicted in 3.2(a). Additionally, thin films of SiNCs functionalized with phenyl groups (Phen-SiNCs) and phenylacetylene groups (PA-SiNCs) were investigated (Fig. 3.2(b) and (c)). The respective organic groups cover the whole surface of the SiNCs after functionalization and form thus an organic shell (monolayer) around the SiNCs, differently to the simplified sketches of Fig. 3.2. The preparation of SiNCs is based on embedded SiNCs in a SiO_2-like matrix

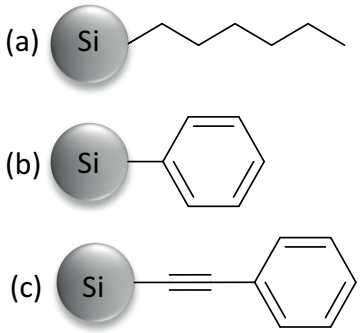

Figure 3.2 SiNCs functionalized with (a) hexyl, (b) phenyl and (c) phenylacetylene groups. Surface functionalization was realized using organolithium reagents. All SiNCs had a diameter of ~ 3 nm.

which is prepared by the synthesis of polymeric hydrogen silsesquioxane (HSQ), based on a literature-known procedure [95]. To obtain free-standing hydride-terminated SiNCs, a synthetic procedure based on the thermolysis of HSQ was applied which was first shown by Veinot et al. [96] and recently reviewed in detail [28]. The surface functionalization of the obtained hydride-terminated SiNCs with hexyl, phenyl or phenylacetylene groups was realized with organolithium reagents as described in [77]. A more detailed description of the synthesis and functionalization of the SiNCs as well as their characterization can be found in the Appendix A.1.

3.1.3 Organophosphonate molecules

All SAMs considered in this work are based on organophosphonate molecules because of their ability to covalently bond to metal oxides and SiO_2 due to their phosphonic acid group [97, 98]. Three different organophosphonate molecules were used in this work as schematically shown in Fig. 3.3: two aromatic organophosphonates, namely (a) 2-phosphono-9,10-diphenyl-anthracene (PAphenyl) and (b) 2,6-diphosphono-9,10-dianthracene anthracene (PAanthrac), and one aliphatic organophosphonate, (c) 1-hexadecanephosphonic acid (PAC16) which was

used as reference molecule in the electrical measurements. PAC16 was purchased from *Strem Chemistry*. All aromatic organophosphonates were synthesized by Dr. Kung-Ching Liao at Prof. Jeffrey Schwartz's lab (Princeton university). PAphenyl is a mono-organophosphonate molecule which contains only one phosphonic acid group, whereas PAanthrac is a bis-organophosphonate molecule which contains two phosphonic acid groups, one on each side of the anthracene backbone.

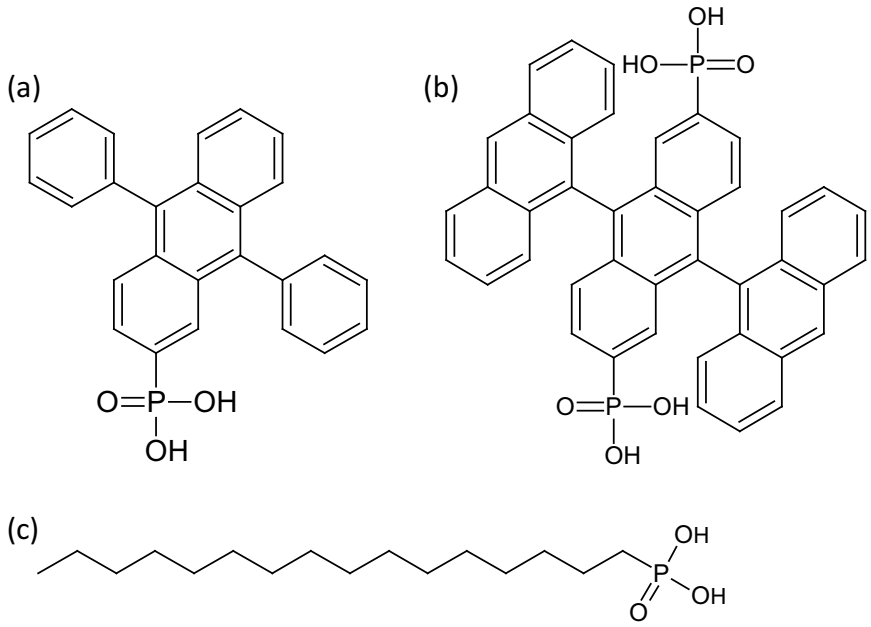

Figure 3.3 Lewis structures of organophosphonate molecules used for SAMs. (a) 2-phosphono-9,10-diphenyl-anthracene (PAphenyl), (b) 2,6-diphosphono-9,10-dianthracene anthracene (PAanthrac) and (c) 1-hexadecanephosphonic acid (PAC16).

3.2 Fabrication methods

Several fabrication methods have been applied for the fabrication of the Si nanogap electrode samples. The most important ones are briefly explained in the following.

3.2.1 Photolithography

Photolithography is a well known standard process both in lab scale as well as in industry to generate mask patterns on samples for either (metal) deposition or etch purposes. Throughout this work, sample patterning by photolithography was used for both purposes. In general, a flat surface of a sample is first coated by a photosensitive polymer thin film (photoresist) via e.g. spin coating and exposed to UV light through a patterned mask with a specific exposure dose. The UV light changes the photosensitive polymer layer chemically at those areas that are not covered by the mask. The locally changed chemical properties of the photoresist are utilized in

a subsequent developing step when the exposed sample is immersed in a developer bath. The developer dissolves then locally the photoresist and transfers as a result the mask pattern in the photoresist layer. Depending on the typ of photoresist, either the exposed or masked parts of the photoresist layer are dissolved: in case of a positive tone photoresist, only the exposed areas of the photoresist are developed. All other parts withstand the developing bath and vice versa in case of a negative tone photoresist.
Most of the photolithography tasks in this work were done with the image reversal resist *AZ5214E (MicroChemicals)* as positive tone resist. Typical film thickness after spin coating was $\sim 1.6\,\mu m$. We used the developer *AZ351B* (*MicroChemicals*, 1 : 4 diluted with DI H_2O).
In some cases the adhesion of the photoresist layer to the sample surface was insufficient which resulted in areas of misplaced photoresist patterns on the sample surface after developing, probably because of the high aspect ratios of some mask features. If thorough surface cleaning with organic solvents and oxygen plasma right before resist coating could not improve the adhesion, the adhesion promoter hexamethyldisilazane (*HMDS, Aldrich Chemistry*) was spin coated right before the photoresist coating.
After the subsequent processing step such as metal deposition or etching, we immersed the samples consecutively in the organic solvents acetone and isopropanol to remove the photoresist layer of the sample (lift-off step in case of metal deposition).

3.2.2 Electron-beam lithography

Electron-beam lithography (EBL) is in principal similar to photolithography. A suitable polymer thin film is coated as an electron beam (ebeam) resist layer on the sample surface which is then exposed and subsequently developed similiar to photolithography. However, there are two major differences: First, the exposure is not realized by UV light through a mask but directly by a focused ebeam. The ebeam is typically produced by an ebeam gun via field electron emission at high electric fields, typically at acceleration voltages in the order of 10 kV to 100 kV under ultra high vacuum conditions. The ebeam is focused via magnetic lenses on the sample surface. Since the wavelength of electrons is much smaller compared to that of UV light, the resolution limit is much smaller than in optical photolithography. As a result, very small pattern features in the order of 10 nm or below [99] can be in principal resolved via EBL. Secondly, no mask is required for exposure since in EBL the ebeam is sequentially moved over the sample surface line by line to expose the areas of interest. The required energy dose to fully expose the resist layer determines the dwell time of the ebeam at each exposure pixel. The pattern is designed with the help of standard CAD software. An introduction to EBL can be found e.g. in [100]
One drawback of EBL is the comparably slow overall exposure time per sample due to the sequential nature of the exposure which limits the throughput of samples and the associated high costs per sample. That is why EBL is rather suitable for lab scale developing purposes than for large scale chip production.
In this work, a positive-tone EBL resist (*AR-P* 6200*, Allresist*) was used with a thickness of

$\sim$ 80 nm after spin coating. The samples were exposed in an EBL system (30 kV acceleration voltage, *e_LINE, Raith*) with an aperture of 10 µm and a typical ebeam dose in the range of 80 µC/cm^2 to 100 µC/cm^2. Development time was 60 s (developer: *AR* 600-546*, Allresist*).

3.2.3 Reactive ion etching

One method to transfer the lithographically defined nanogap pattern after developing into the top Si device layer is reactive ion etching (RIE). RIE is a dry chemical etch process. We used the inductively coupled plasma reactive ion etcher (ICP-RIE) *Plasma Lab* 80 *Plus* from *OXFORD Instruments*. A good overview about RIE and especially ICP-RIE can be found in [101].
The sample is placed in an evacuated chamber on a temperature controlled stage. Typical chamber pressures are below $\sim 1 \times 10^{-5}$ mbar. The chamber is then filled with the process gases. For Si etch purposes, a combination of SF_6 and C_4F_8 gases was used. To ionize the gas mixture and hence create a plasma, energy needs to be provided. This excitation of the plasma in an ICP-RIE is realized via a time-varying radio frequency (RF) source which is inductively coupled to the plasma via a coil wrapped around the plasma chamber. Since electrons move faster than the heavy ions in the plasma, they cause further ionization through collisions with the slow moving ions. For the same reason, more electrons will be lost to the grounded side walls of the chamber, leaving slightly more ions than electrons in the plasma. As a result, the ICP coupling controls to some extent the ion density in the plasma. The positive ions react both, chemically and physically with the sample surface. Chemically, because they initiate a chemical etch process with the atoms of the sample surface and physically, since they knock-off (sputter) atoms from the sample surface. Depending on the plasma conditions also the reverse process, deposition of material is possible. Careful adjustment of the plasma parameters is therefore necessary. Additionally to the ICP mechanism, the RIE is equipped with a capacitive coupled plasma (CCP) power source which is in principal a capacitor realized by the stage as one capacitor plate and the chamber itself as the counter plate. The CCP power source is often referred to as the "forward power" since it mainly controls the physical sputter component of the RIE process. On the other hand, since the ICP power source controls among others the ion density one can think of the ICP source controlling mainly the chemical part of the RIE. One big advantage of the ICP-RIE is therefore the almost independent control of ion density and bias voltage which can result in very anisotropcal etch profiles.

3.2.4 Anisotropically etching in potassium hydroxide

Si can be chemically and anisotropically wet-etched in potassium hydroxide (KOH) due to the different etch rates of the Si crystal planes in KOH. The {111} planes are etched more slowly than the {100} planes. This results in etching features which comprise the characteristic angle of 54.7° between (100) and (111) planes as schematically shown in Fig. 3.4(a). Etch rates and selectivity to e.g. SiO_2 depend strongly on the concentration of KOH and

the temperature. As mask material, typically SiO_2, nitride layers or metal masks such as gold are used [102, Ch. 20]. An introduction to anisotropically etching in KOH can be found in [103].

In this work, a simple KOH etch setup was used as depicted in Fig. 3.4(b). 80 ml KOH solution was filled in a 100 ml beaker and continually stirred by a magnetic stir bar to minimize local OH^- concentration gradients. The beaker was placed on top of a hotplate to maintain a constant etch temperature. Up to 4 samples were etched simultaneously in one KOH etch run by carefully clamping them with tweezers and immersing them in the KOH solution. We used typically a KOH concentration of 9 % (in DI H_2O) and a nominal temperature of the hotplate of 45 °C which resulted in a stable temperature of the KOH solution of $T = 32\,°C$.

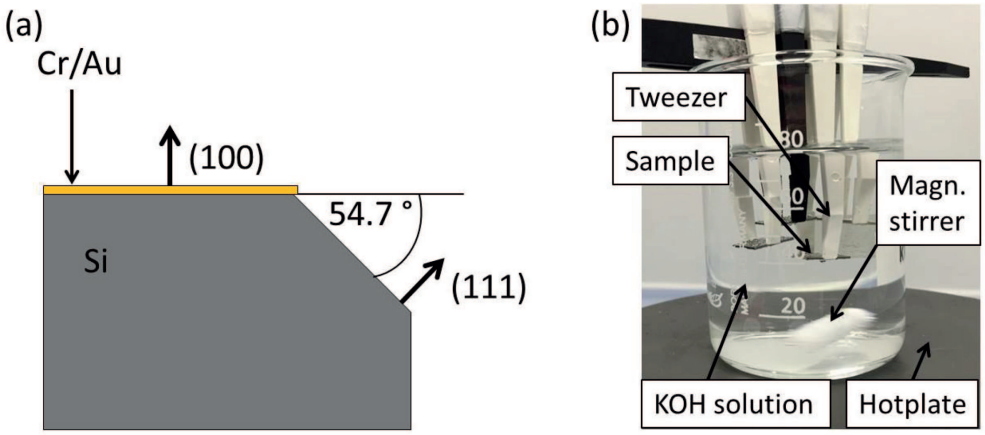

Figure 3.4 (a) Schematic showing the anisotropical, crystal direction dependent etching behaviour of silicon in KOH solutions. Due to different etch rates in ⟨111⟩ and ⟨100⟩ directions, a characteristic angle of 54.7° between the (100) and (111) planes can be observed. (b) Image of KOH etch setup. Image adapted from [104].

3.2.5 Metal deposition

Metal layer deposition was done via physical vapor deposition (PVD). The metal, placed in a crucible, is heated in a vacuum chamber (typical pressure values are $< 1 \times 10^{-6}$ mbar) in one of two ways: Either thermally by resistive heating by driving high currents through the crucible or directly via local heating by an ebeam. In both cases, metal atoms are released once the vapor pressure of the metal is reached. The sample is mounted in the vacuum chamber above the crucible with its surface facing towards the metal source. The metal atoms impinge on the sample surface and are eventually adsorbed once the shutter is opened which initially prevents the sample surface from uncontrolled metal deposition. Because of the high vacuum in the chamber, collisions of the metal atoms with residual gas atoms are negligible. It is possible to monitor the deposition rate of the metal atoms on the sample surface via the frequency change of an oscillating quartz crystal, placed in vicinity of the sample so that it is exposed to the same amount of the released metal atoms as the target sample. The metal evaporation rate can then

be adjusted by controlling the heating of the metal source.
For most of the samples in this work, metal deposition was done by ebeam PVD (*Leybold L560*). Typical evaporation rates were max. 2 Å/s for gold, and max. 1 Å/s for titanium and chromium.

3.2.6 Functionalization with self-assembled monolayers

We functionalized our samples with SAMs of organophosphonate molecules. The functionalization process depend strongly on the substrate material. In our case SiO_2 is used. For organophosphonate SAM growth on SiO_2, there is a well established deposition protocol developed by Hanson et al. called "Tethering By Aggregation and Growth" (T-BAG) [98] as schematically depicted in Fig.3.5. A sample placed on a teflon holder is vertically immersed in a solution of dissolved organophosphonate molecules far below their critical micelle concentration. While the solvent slowly evaporates, molecules aggregate to some extent at the solvent/air interface and are transferred to the sample surface in an almost inverse way to the Langmuir-Blodgett method. In a last step, the molecule coated samples need to be annealed to covalently bond the organophosphonate molecules to the SiO_2 surface. Several washing steps with organic solvents remove finally any additional deposited molecules which are not bonded to the sample surface, resulting ideally in a monolayer of organophosphonate molecules on the SiO_2 substrate. A detailed description of the experimental parameters used for the functionalization

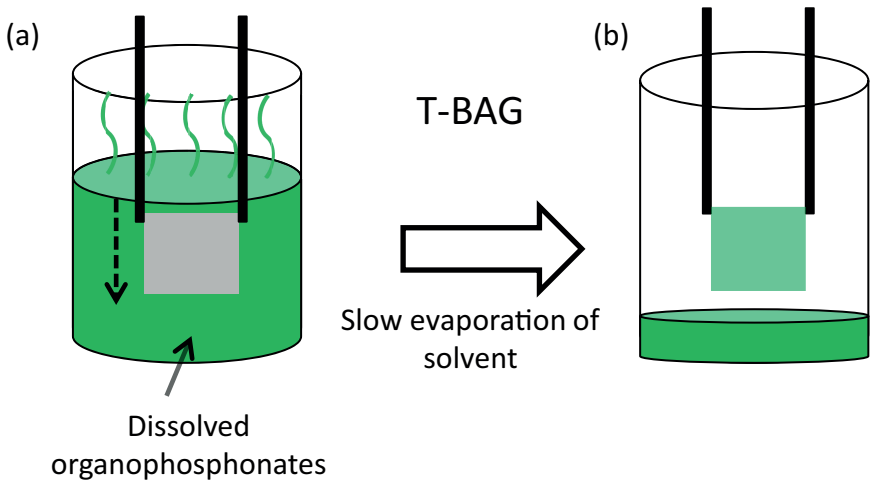

Figure 3.5 Schematic showing the first step of the tethering by aggregation and growth (T-BAG) process. (a) The sample is immersed vertically in a solution of dissolved organophosphonate molecules. While the solvent slowly evaporates, the organophosphonate molecules are adsorbed on the sample surface (b). At last, samples are heated to covalently bond a monolayer of the adsorbed molecules to the surface (not shown).

of SiO_2 samples with organophosphonate SAMs can be found in the Appendix D.1.

3.3 Characterization techniques

In the following, the most important characterization methods which were used during the course of this work are briefly described.

3.3.1 Scanning electron microscopy

Scanning electron microscopy (SEM) uses a focused ebeam similar as described for EBL (cf. Section 3.2.2) to scan a sample surface sequentially line by line to image the topography of a sample surface due to the interaction of the electrons of the ebeam with the sample atoms. Images generated by a SEM have a large depth of field which makes them useful to inspect the surface characteristic of a sample over a large magnification range. The whole system is placed in a vacuum chamber to minimize scatter events of the electrons with atmospheric gas atoms. A introduction to SEM can be found in [105].
A high voltage electron source generates the electrons typically by field emission at voltages in the range of 1 kV to 30 kV. The resulting ebeam is shaped and focused in the adjacent beam column which consist of various electron lenses and coils to condense and deflect the ebeam. The electrons of the ebeam are scattered to some extend inelastically at the sample atoms eventually generating secondary electrons. A detector generates then an image of the sample topography based on the intensity of these secondary electrons. There a various types of detectors used in SEM. A common one is the in-lense detector which is located directly in the ebeam column and detects low energy back scattered secondary electrons. These secondary electrons originate from an interaction volume close to the sample surface which give rise to a high resolution image of the sample surface topography in the order of a few nm. Other detector types detect secondary electrons at a specific angle to the ebeam column or detect elastically back scattered primary electrons.
During the course of this work two different SEMs were used. A *NVision 40 Dual Beam* and a *SEM Evo* both from *Zeiss*. Typical used acceleration voltages were in the range of 3 kV to 5 kV and mainly the in-lense detector was used.

3.3.2 X-ray photoelectron spectroscopy

X-ray photoelectron spectroscopy (XPS) is a surface sensitive spectroscopy technique which reveals information about the binding energies of electrons. It utilizes the photoelectric effect. In brief, a sample is placed in an ultra high vacuum chamber ($\sim 1 \times 10^{-9}$ mbar) and illuminated with monochromatic X-rays (energy of X-ray photons > 1 keV). The X-rays are used to excite electrons of the sample atoms from their atomic core orbitals above the vacuum level. The kinetic energy of the released electrons are then spectroscopically analyzed in an electron detector. Excited electrons from atoms deep below the sample surface are mainly scattered inelastically and lose therefore kinetic energy. Contributions from those electrons are measured as background signal. Only the excited electrons from atoms in a volume in close vicinity of the

surface lead to sharp peaks in the energy spectrum. As a result, XPS is very surface sensitive. Since the binding energies of the electrons are dependent on the element type and the atomic charge distribution of the surface atoms, it is possible to extract information about the elemental composition and the chemical state of the surface atoms from the energy spectrum.
A more detailed introduction to XPS can be found in [106] and [107].

The XPS measurements were carried out in a home-built setup (parts from SPECS Surface Nano Analysis) under ultra-high vacuum ($\sim 6 \times 10^{-9}$ mbar). The setup is equipped with an XR 50 X-ray source and a Phoibos 100 hemispherical electron analyzer. An aluminum anode was utilized, generating X-ray photons of the energy of the Al K_α edge ($E = 1486.6$ eV). The X-ray source was operated at a voltage of 12.50 kV and an emission current of 20 mA. Photoelectron spectra were acquired at an energy resolution of 0.1 eV and a dwell time of 1 s and averaged over two to four scan repetitions. A pass energy of 30 eV was used universally. XPS data were analyzed with *CasaXPS* software (*Casa Software Ltd*, charge referencing, background subtraction and elemental analysis) and *Origin* (*OriginLab*, intensity normalization and plotting).
The XPS spectra were charge-referenced with respect to the C 1s hydrocarbon peak at 284.8 eV and corrected for analyzer transmission and photoelectron escape depth. For quantitative analysis and normalization, relative sensitivity factors (Scofield cross-sections [108]) for each peak were retrieved from the *CasaXPS* library, accounting for the effective photoionization cross-section of the associated electronic transition.

3.3.3 Atomic force microscopy

Atomic force microscopy (AFM) is a powerful tool to image accurately the topography of sample surfaces. While the lateral resolution is in the order of a couple of 10 nm, the resolution in height can be in the range of 1 nm. An introduction to AFM can be found in [109]

AFM utilizes the interaction of a sharp tip with the atoms of a sample surface. These interactions can be attractive or repulsive depending on the distance of the tip to the sample surface. A general AFM setup consists of a tip attached to a cantilever that oscillates close to its eigenfrequency driven by piezoelectric crystals. With the help of a laser beam which is reflected at the backside of the cantilever, a four quadrant photo detector can detect small changes in the amplitude. A electronic feedback loop adjusts the driving voltage of the piezoelectric crystals to maintain a constant oscillating amplitude of the cantilever. The information gained from the feedback loop is then typically processed to a height image of the sample topography. By moving the tip over the sample surface line by line, it is possible to generate a height image of the sample topography.
Beside this non-contact operation mode, there is also the possibility to operate the AFM in contact mode. For this purpose, the tip is brought in contact with the sample surface via a controlled bending of the cantilever through the piezoelectric crystals. Changes in the sample

topography lead then to force changes of the tip to the sample surface which are detected via the feedback loop by adjusting the bending of cantilever to maintain a constant tip-sample force.
AFM images were taken with a *Dimension V* from *Bruker/Veeco*. The AFM was mostly operated in tapping mode equipped with a silicon tip which was coated with a diamond-like-carbon-coating (*TAP*190*DLC, BudgetSensors*). Scan rate was typically 1 Hz. Images were analyzed using the *NanoScope Analysis* 1.5 software from *Bruker*.

AFM nanolithography scratching

For SAM functionalized samples, AFM nanolithography scratching [110] was used to determine the thickness of the SAM. First, a $5 \times 5\,\mu m^2$ area of the reference sample functionalized with the SAM was scanned in tapping mode. Afterwards, a $1 \times 1\,\mu m^2$ area was scanned in contact mode without moving the sample. We adjusted the deflection set point of the cantilever to keep the applied force of the tip to the sample surface constant. The force value was chosen that the tip removed the SAM from the surface but did not scratch into the SiO_2 substrate. The scan size was increased again to an area of $5 \times 5\,\mu m^2$ and the sample was subsequently scanned in tapping mode revealing the topography of the scratched area.

3.3.4 Current voltage spectroscopy with probe station

The nanogap samples were electrically characterized using a vacuum probe station (*TTPX*, *Lakeshore*) as shown in Fig. 3.6(a). The probe station is equipped with 4 probe arms which comprise micro manipulators for precise movement of the attached probe tips in x, y and z-direction. We used typically beryllium-copper or tungsten probe tips. The samples are placed in a vacuum chamber and a turbo pumping system is used to achieve pressures down to $\sim 5 \times 10^{-6}$ mbar in the vacuum chamber. This allowed stable measurement conditions, especially for oxygen-sensitive samples. During chamber opening for sample exchange, the chamber is continuously flushed with dry N_2 gas to maintain good vacuum conditions in the chamber. A camera system on top of the viewing window of the vacuum chamber allowed the exact monitoring of the probe tip landing on the sample surface. Fig. 3.6(b) shows an otical image from that camera system showing two probe tips landed on Au pads of a device under test (DUT).
External measurement equipment such as source measure units (SMU) are connected to the probe arms via low noise triax connectors and cables. Triax cables comprise an additional conductor (in total: 3 conductors) between the signal conductor and the outer ground layer compared to BNC cables. This additional middle conductor guards the signal conductor by applying the same potential to the guard conductor as to the signal conductor. As a result, there is no voltage difference between the inner two conductors and hence no leakage current which reduces the electrical noise and makes triax cables and connectors suitable for low current measurements.

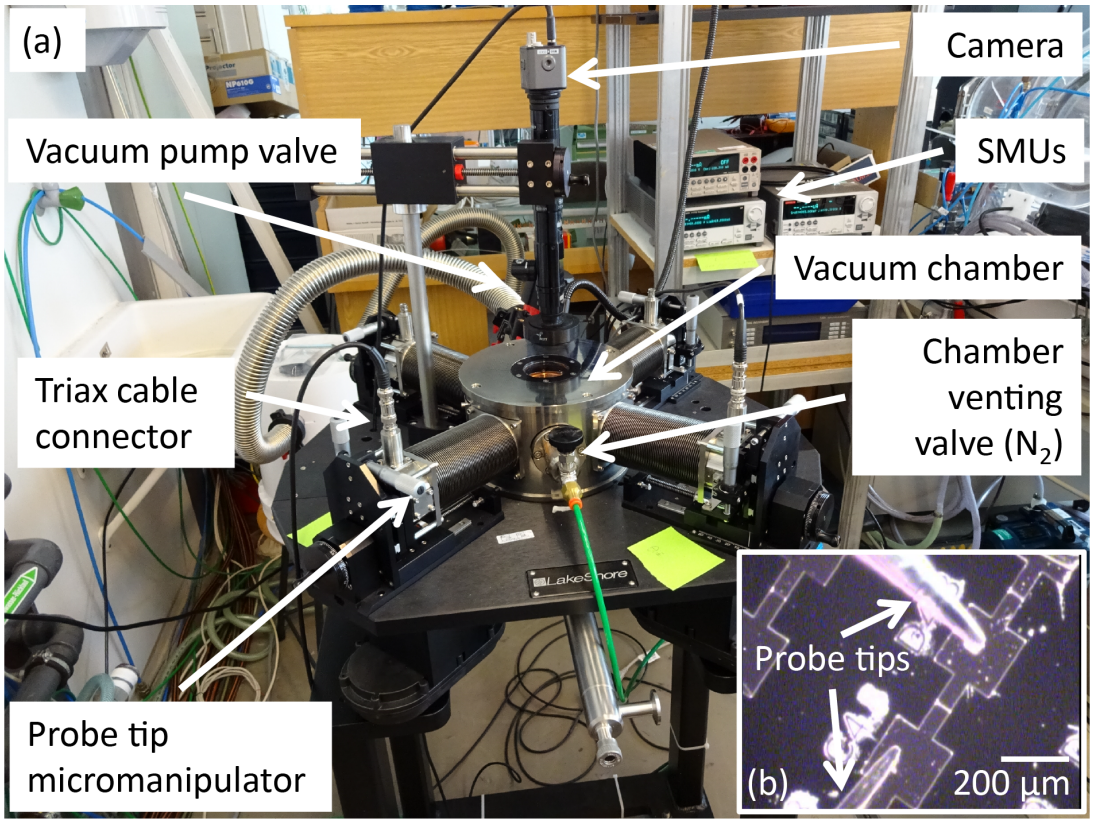

Figure 3.6 (a) Image of the vacuum probe station setup equipped with 4 probe arms. A camera system on top of the viewing window of the vacuum chamber allows the exact monitoring of the probe tip landing on the sample surface. External measurement equipment such as source measure units are connected to the probe arms via low noise triax connectors and cables. A turbo pumping system allowed pressures down to $\sim 5 \times 10^{-6}$ mbar in the vacuum chamber. (b) Optical image (top-view) taken via the camera system, showing two probe tips which are positioned on the Au contact pads of the device under investigation inside the vacuum chamber of the probe station.

The vacuum chamber encloses a second chamber which is used as radiation shield to minimize electrical noise as schematically depicted in Fig. 3.7. Two-terminal *I-V* measurements are typically realized by landing the probe tips to the top contacts of the sample and connecting the external measurement circuitry via the triax connectors of the probe arms. We used source measure units (SMU) manufactured by *Keithley* (*Keithley* 2635*B*) which allowed the simultaneous application of a voltage while measuring the current signal. For three-terminal measurements, a second SMU is connected additionally to the triax sample stage. This way, a global gate potential is applied to the back side of the sample with respect to the source top contact (signal ground).

If not stated otherwise, all measurements were conducted at room temperature and in darkness by covering the viewing window of the vacuum chamber during measurements. DC *I-V* curves were typically measured at a scan rate of about 150 mV/s by controlling all SMUs by a PC (Matlab software) via GPIB.

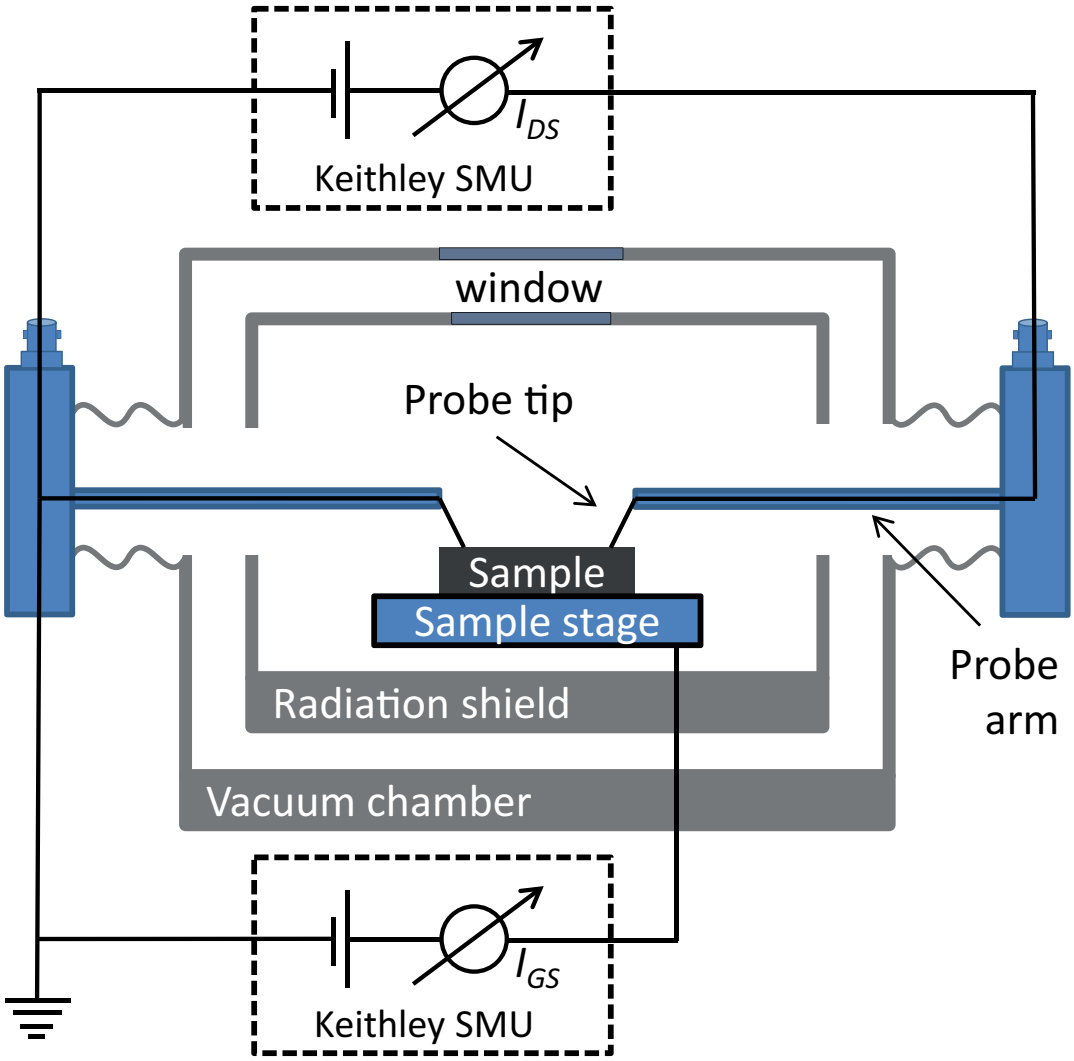

Figure 3.7 Schematic cross-section of the probe station and typical used electrical circuitry. The sample is placed on a triax stage which serves as global back contact. Probe tips contact the device under test on the sample surface and are electrically connected via the probe arms and the triax connectors with the external measurement circuitry. The sample is enclosed in two chambers which are both electrically grounded (not shown). The inner one acts as additional radiation shield to minimize electrical noise. The outer one is used as vacuum chamber. Electrical connections are typically made via triax cables and *Keithley* 2635*B* SMUs were used for two and three terminal *I-V* measurements. All measurements were controlled via a Matlab program on a PC.

3.3.5 Current voltage spectroscopy with hanging mercury droplet electrode

Planar, unstructured samples were characterized electrically with a hanging mercury droplet electrode setup. Hg is a liquid metal at room temperature. Due to the high surface tension of Hg, it is possible to apply a very gentle and soft top contact with a Hg droplet on top of fragile sample surfaces and measure e.g. the *I-V* characterization vertically through the sample. Fig. 3.8 depicts the general setup of the hanging Hg droplet electrode. A hanging droplet of

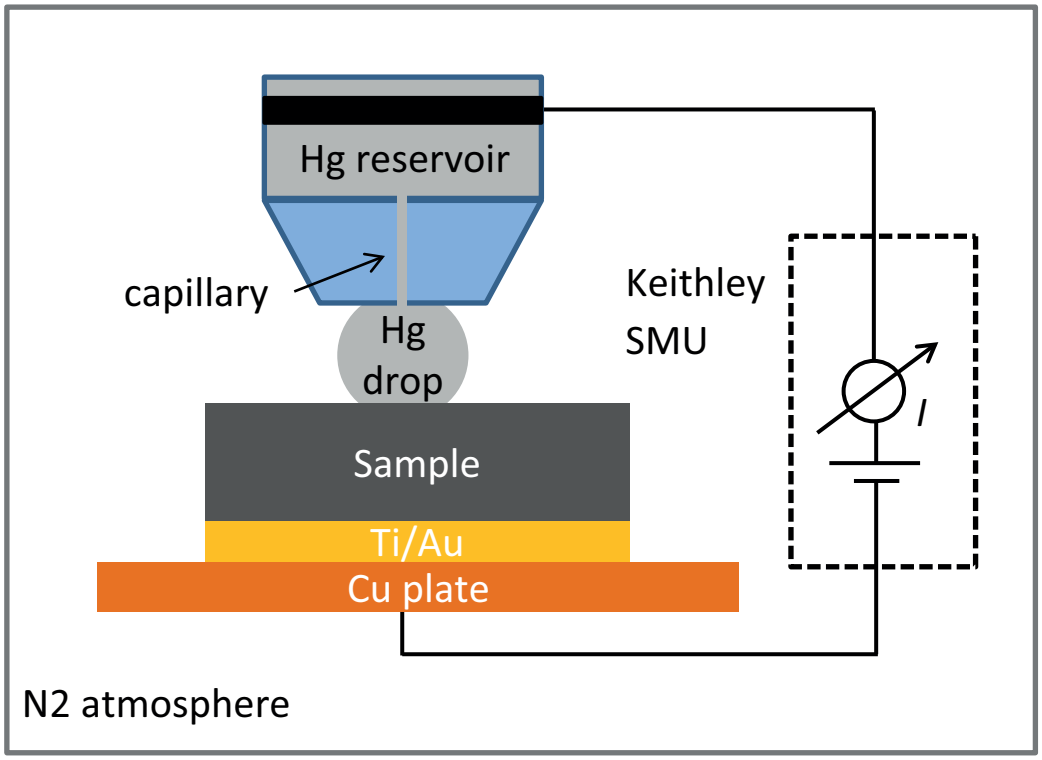

Figure 3.8 Schematic of hanging mercury droplet electrode setup. A hanging droplet of mercury with defined volume is formed at the lower end of a capillary which is connected at the upper part to a mercury reservoir. The sample is placed on a copper stage below the hanging Hg droplet and slowly driven upwards until the Hg droplet wets the sample surface. Electrical connections for vertical measurements through the sample are made via the sample copper stage and from the other side via a metallic ring contact around the Hg reservoir. Typically a *Keithley* 2635 SMU was used for DC *I-V* measurements. The whole setup is operated in a N_2 filled glovebox to achieve stable Hg contacts on the sample surface.

Hg with defined volume is formed at the lower end of a capillary which is connected at the upper part to a mercury reservoir. The droplet stays hanging at the capillary end due to the high surface tension of Hg. The sample is placed on a copper stage which can be moved in x,y and z-direction by micro-manipulators. The sample backside is typically coated with a metal layer, e.g. Ti/Au and glued with silver paint to an additional copper plate to ensure a good electric contact to the copper stage. The sample surface and the hanging Hg droplet can be monitored by a camera system which is placed perpendicular to the capillary end in front of the stage. The stage is moved slowly upwards until the Hg droplet gets into contact with the sample

surface as shown in Fig. 3.9. Electrical connections are made at the backside of the sample via the copper stage and by a metallic ringlike contact around the Hg reservoir which is connected via the Hg column in the capillary and the Hg droplet to the sample surface. The vertical DC *I-V* characteristic of the sample is measured with a *Keithley* 2635 SMU controlled via a PC (Matlab program). The whole setup is operated in a glovebox filled with N_2 to avoid moisture contamination on the sample surface and to keep the oxygen level low in order to achieve stable electrical contacts of the Hg droplet with the sample surface. Mostly samples with non-metallic

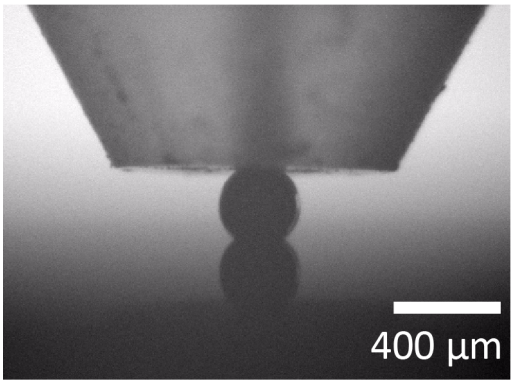

Figure 3.9 Optical image (side view) showing a Hg droplet at the end of the capillary in contact with a SiO_2 surface. The image was taken with the camera system which is used to monitor the sample approaching the hanging Hg droplet.

surfaces can be used with the hanging Hg droplet since most metals form an amalgam with Hg which destroys the Hg droplet and can contaminate the Hg capillary and the sample itself.
We used a controlled growth mercury electrode (CGME) manufactured by *Bioanalytical Systems, USA* which comprises the Hg reservoir, the capillary and an electronically controlled Hg dispenser in a customized glovebox from *PlasLabs, USA* equipped with a load lock. A home made control system comprising a standard lab pump and a feedback pressure sensor circuitry keep a constant and slight N_2 overpressure in the glovebox.

3.3.6 Impedance spectroscopy

Impedance spectroscopy is an AC technique which measures the complex impedance Z represented by its magnitude $|Z|$ and the corresponding phase angle Θ between an applied sinusodial voltage and the measured current response over a broad frequency range.

$$Z = |Z|e^{j\Theta} \tag{3.1}$$

The measured current response is typically presented in Bode plots which show the frequency dependence of Z and Θ. The power of impedance spectroscopy is that the frequency-dependent measurement signals can be fitted according to suitable equivalent circuit models. If the fit is carefully adjusted to the measurement data, information of single components of the sample

can be extracted even for complex multi layer systems.
During the course of this work impedance spectroscopy was done with the help of an ivium compactstat (*Ivium Technologies*) in a two terminal configuration. The hanging Hg droplet setup was used to contact planar samples electrically (cf. Section 3.3.5). No DC bias was used and typical AC voltages were in the range of 100 mV to 150 mV with frequencies in the range of 1 Hz to 1×10^6 Hz. Equivalent circuit fitting was done with the ivium software.

4 Silicon nanogap electrode fabrication, characterization and nanogap filling

4.1 Nanogap fabrication by anisotropically etching in potassium hydroxide

This Section is partly based on the published conference proceeding: A nanogap electrode platform for organic monolayer-film devices [70] (Simon Pfaehler et al., 2016 IEEE 16th International Conference on Nanotechnology (IEEE-NANO) (Sendai, Japan). IEEE, 2016, 842–844, DOI: 10.1109/NANO.2016.7751507.)[1]

4.1.1 Device design and sample layout

We used an evaporated metal pattern as etching mask for the nanogap electrodes. The device design utilizes the anisotropical etching behaviour of silicon in KOH regarding its crystal planes as described in chapter 3.2.4. The {111} planes are etched far slower than the {100} planes which results eventually in inverted triangular shaped trenches [111]. This anisotropy results in Si gaps at the bottom of the converging {111} planes once the tip of the inverted triangle reached the buried SiO_2 layer since the SiO_2 acts as an effective etch stop. The resulting Si gaps are smaller than those of the metal mask. Fig. 4.1 shows schematically the design concept with all relevant geometrical parameters: w is the width of the gap, d is the thickness of the Si device layer, L is the distance between two metal pads and l is the resulting nanogap length at the bottom of the gap. Beside the etch time, l depends on L and d and can be geometrically calculated by

$$l = L - \frac{2d}{\tan(54.74°)} \tag{4.1}$$

with $\alpha = 54.74°$ as the characteristic angle between the silicon {111} and {100} planes.

[1] Reprinted (adapted) with permission from [70]. Copyright (2016) IEEE. Most of the experimental work on the fabrication of anisotropically etched silicon nanogaps in KOH presented in this Section was obtained in close collaboration with Kevin Keim as part of his master's thesis [104].

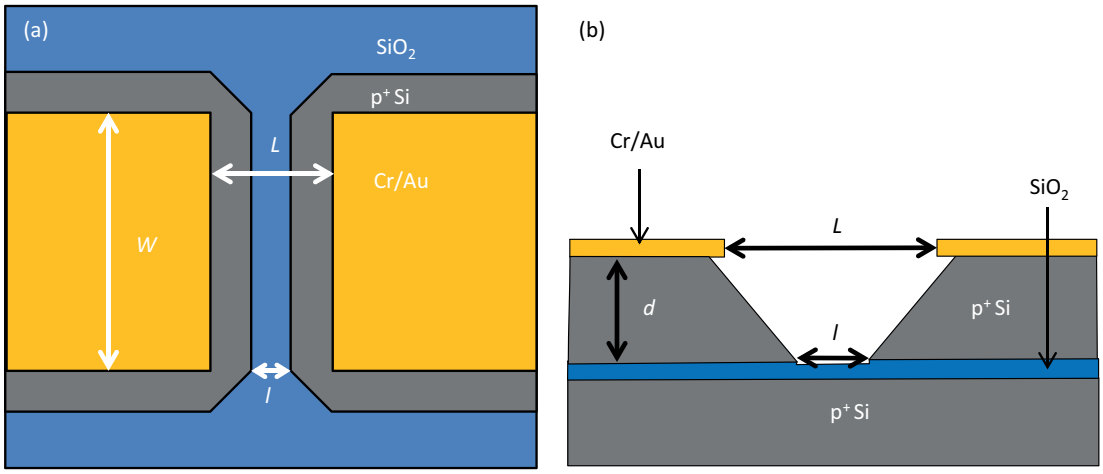

Figure 4.1 Schematic showing the nanogap dimensions after KOH etching. (a) top view and (b) side view.

4.1.2 Nanogap fabrication

We used SOI wafer pieces consisting of a $(3.0 \pm 0.5)\,\mu m$ thick, highly p-doped Si device layer (Boron, $9 \times 10^{18}\,cm^{-3}$, (100)), separated from the handle wafer (analogously doped) by an $(8.0 \pm 0.4)\,nm$ thick buried silicon dioxide layer (cf. Fig. 4.2).

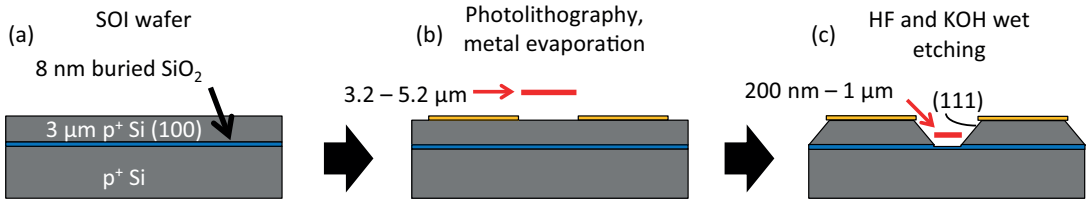

Figure 4.2 Schematic showing the fabrication process of the nanogap electrodes. A patterned metal film is evaporated on top of an SOI substrate with a 3 µm thick p^+ Si (100) device layer; it serves as the etching mask as well as the electrical contact pads. The typical spacing between two metal pads was in the range 3 µm to 5 µm. Subsequent anisotropic etching in KOH solution resulted in characteristic, triangular shaped nanogap structures. Reprinted (adapted) with permission from [70]. Copyright (2016) IEEE.

An evaporated metal thin film of Cr/Au (10/100 nm) was patterned by standard photolithography methods and was used as the etching mask as well as a contact pad for eventual electrical measurements. After mask preparation, all samples were dipped in aqueous hydrofluoric acid (HF, 5%) to remove the native silicon oxide layer, and were subsequently etched in aqueous potassium hydroxide (KOH, 9%, 32 °C) for 210 min. Special attention was paid to the alignment of the lithographically defined pattern along one of the [110] crystallographic directions to optimize anisotropic etching. In this way, the micrometer-spaced gaps of the metal mask were translated to the oxide interface: Our etch mask pattern comprises electrode metal pairs with spacing $L = 3.2\,\mu m$ to $5.2\,\mu m$ which resulted in gap electrode distances on the order of $l = 200\,nm$ - $1\,\mu m$. Fig. 4.3(a) shows an optical microscope image of a part of a sample chip

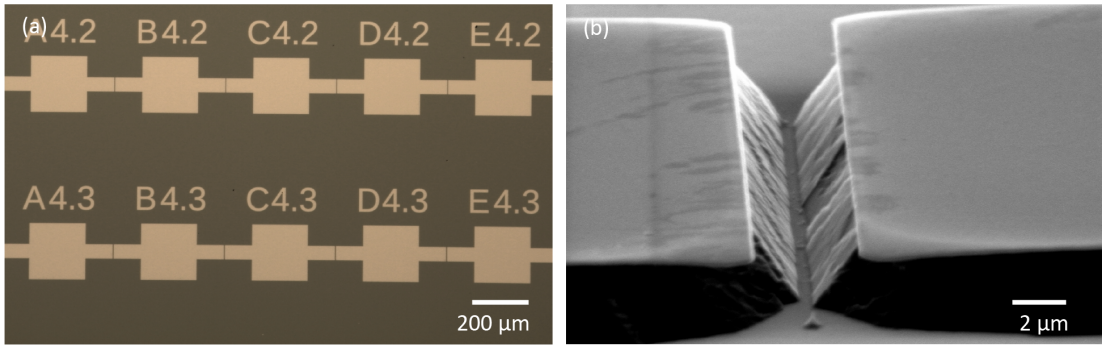

Figure 4.3 (a) Optical microscope image of a part of a sample chip with several gaps arranged in line, pairwise sharing electrical contacts before KOH etching. Gap width is $w = 50\,\mu m$ and gap length is $L = 4.2\,\mu m$ (top row) and $L = 4.3\,\mu m$ (bottom row). (b) SEM image taken at a viewing angle of 80°, showing a silicon nanogap after etching in KOH for 210 min.

after metal PVD and lift-off but before KOH etching. The gaps are arranged in lines sharing pairwise electrical contacts. The top row comprises gaps with $L = 4.2$ µm and the bottom row with $L = 4.3$ µm. One chip comprises 150 electrode pairs. Fig. 4.3(b) shows a SEM image taken at a viewing angle of 80° of a finished nanogap after etching in KOH for 210 min. The trapezoidal structure of the nanogap crossection is clearly visible. The metal pads on top of the Si device layer are slightly under-etched since the etching rate of the {111} plane is small but not negligible. At the edges of the nanogap, etching of the {110} planes is possible and visible in the SEM image which leads to a tapered shape at the nanogap edges. We fabricated therefore only nanogaps with $w > 20$ µm which is far broader than the observed etching of the {110} planes at the nanogap edges.

In order to achieve the best possible control of the etch process for our samples and etch

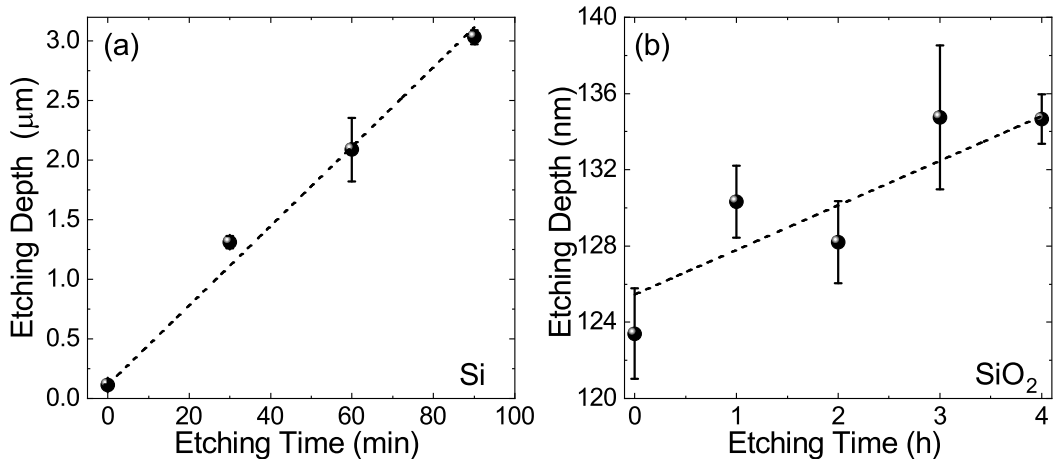

Figure 4.4 KOH etch depth versus etching time of (a) Si and (b) SiO_2 for 9 % KOH at 32 °C. The dashed lines are linear fits to the data. The error bars represent the standard deviation of 5 measurements.

setup, we determined the etch rates in KOH for $Si_{\langle 100 \rangle}$ and SiO_2. Samples with a simple Cr/Au pattern were used and the top of the Cr/Au layer served as height reference for etch depth measurements, carried out with a profilometer. All samples were etched in aqueous potassium hydroxide (KOH, 9%, 32 °C). All Si samples were dipped in aqueous hydrofluoric acid (HF, 5%) right before the KOH etching to remove the native silicon oxide layer. To investigate the etch rate of SiO_2, Si/ SiO_2 samples with a 100 nm thick thermal SiO_2 layer were used. Since the etch rate is much smaller for SiO_2, the etch depth was measured with an AFM for the SiO_2 samples. The measured etch depth with respect to the etch time is depicted in Fig. 4.4 (Si: (a) and SiO_2: (b)). The dashed lines are linear fits to the data. The etch rates r are determined from the slope of the fits. For Si, an etch rate of $r_{Si} = (33.3 \pm 1.7)$ nm/min is determined which is about half of the literature value of $r_{Si,lit} = 53.8$ nm/min for 10 % KOH at 30 °C [112]. One possible reason is the high doping concentration of the Si device layer which decreases the etch rate [112]. For SiO_2, an etch rate of $r_{SiO_2} = (2.3 \pm 0.6)$ nm/h was determined which is roughly a factor of 2 greater than the literature value of $r_{SiO_2,lit} = 1.2$ nm/h for 10 % KOH at

30 °C [112], possibly due to our slightly higher etch temperature. The resulting etch selectivity of $r_{\mathrm{Si}_{\langle 100\rangle}}$ to $r_{\mathrm{SiO_2}}$ is

$$\frac{r_{\mathrm{Si}_{\langle 100\rangle}}}{r_{\mathrm{SiO_2}}} = 860 \pm 220$$

which is smaller than the literature value of 2634 [112] mainly because of the smaller measured etch rate of Si as already discussed. As a result, the 8 nm thick buried SiO_2 layer of the SOI wafer should withstand the KOH etch for ca. 3.5 h based on the experimentally determined etch rate selectivity.

The 3 µm thick Si device layer of the SOI wafer should be completely etched down to the buried

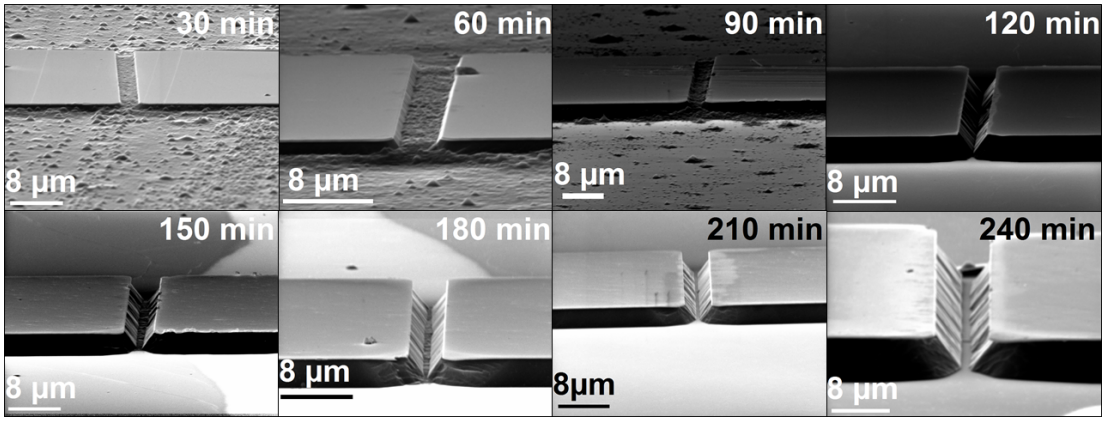

Figure 4.5 SEM images at a viewing angle of 80°, showing the silicon nanogap etch evolution in KOH in [100] direction with time from 30 min (top left) to 240 min (lower right).

SiO_2 in ≈ 90 min according to the experimentally determined etch rate of Si (c.f. Fig. 4.4(a)). However, this is true for planar samples without any geometrical constraints. If the inclining Si {111} planes of the gap patterned samples meet before the buried SiO_2 layer is reached and while the gap is opening at the SiO_2 interface, etching occurs mainly in ⟨111⟩ direction which is much slower. Small variations in L of the metal pad spacing lead therefore to variations in the observed etching times in case of the nanogap etching process. Nanogap samples etched for t =30 min to 240 min in 9 % KOH at 32 °C were therefore investigated by SEM to estimate the best etch time to achieve narrow but open nanogaps. Fig. 4.5 shows the SEM images taken at a viewing angle of 80° for the nanogap etch series. For $t < 120$ min, small residuals next to the gap area are present which might be small residual Si pyramids with {111} planes [113]. At $t > 120$ min all Si residuals outside the gap area are etched away, revealing the smooth surface of the SiO_2 layer (rms roughness: 0.163 nm, measured by AFM) while the gap is not yet completely etched down to the SiO_2 layer. The best result was obtained for an etch time of $t = 210$ min which produced a narrow but open gap without residuals. Etch times longer than $t = 210$ min lead to an increase in gap length l.

The {111} planes forming the sidewalls of the gaps exhibit a certain roughness, visible as alternating pattern of darker and lighter areas in Fig.4.3(b) and Fig. 4.5 which results in a

certain edge roughness along the gap at the bottom. The exact origin of this edge roughness is not fully clear. In the literature, it is reported that the KOH etch process can be locally masked by the formation of H_2 gas bubbles which originate from the etch process itself and hence results in an increased roughness [114]. Another possible reason could be the slight misalignment of the surface orientation which also leads generally to an increased roughness as described in [115].

4.2 Nanogap fabrication by e-beam lithography and reactive ion etching

We used a second approach for the fabrication of Si nanogaps beside the concept of anisotropically etching in KOH. The main difference is the use of ebeam lithography to define the etch pattern and transferring it via RIE into the Si device layer instead of chemical wet etching in KOH.

4.2.1 Nanogap fabrication

The following Section is based on the published article: Space charge-limited current transport in thin films of alkyl-functionalized silicon nanocrystals [116] (Simon Pfaehler et al., Nanotechnology, 30(39) (2019), 395201, DOI: 10.1088/1361-6528/ab2c28)[2].

The process of Si nanogap device fabrication is outlined in Fig. 4.6. Silicon electrodes were fabricated from SOI wafers (Soitec, France), composed of a $d = (110 \pm 7.5)$ nm thin silicon device layer (100) separated by a (200 ± 5) nm buried silicon dioxide (SiO_2) layer from the silicon handle wafer (100). The top silicon layer was heavily p-doped by ion implantation (p^+, Boron, doping concentration ca. $5 \times 10^{19}\,cm^{-3}$) (a). The SOI wafers were diced in $8 \times 8\,mm^2$ sample chips. For the fabrication of an array of electrode pairs (cf. Fig 4.7(a)), the SOI sample chips were first cleaned by sonicating them in acetone (VLSI Selectipur, BASF), subsequent sonicating them in isopropanol (VLSI Selectipur, BASF) and blowing them dry under a stream of N_2, followed by an additional cleaning step in oxygen plasma (18 s, 400 W, 50 Pa). We used conventional photo-lithography to pattern the etching mask for the mesa-structure of the electrodes array: At first, an adhesion promoter hexamethyldisilazane (HMDS, Aldrich Chemistry) and a positive-tone photo resist (AZ5214E, MicroChemicals) were deposited by spin-coating (film thickness: 1.6 µm). Following resist development (AZ351B, 1 : 4 diluted with DI H_2O, MicroChemicals) and an additional oxygen plasma treatment to remove adhesion promoter and resist residues (18 s, 400 W, 50 Pa), the mesa-structure was etched in the top silicon device layer down to the buried oxide by RIE (SF_6/ C_4F_8 plasma, OXFORD Instruments, Plasma

[2]Reprinted (adapted) from [116]. Copyright (2019) IOP Publishing Ltd, Creative Commons BY 3.0 license (http://creativecommons.org/licenses/by/3.0)

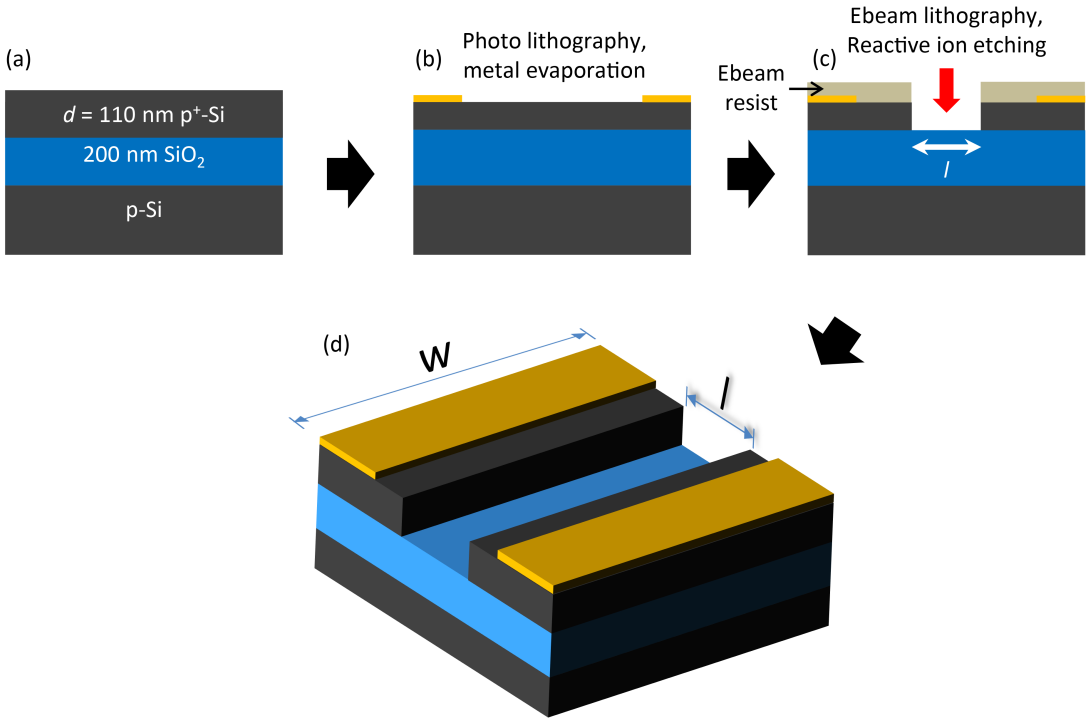

Figure 4.6 Schematic showing the fabrication process of the silicon nanogap electrodes based on a SOI wafer (a). (b) Metal contact pads (yellow) are fabricated using photo lithography, metal evaporation and lift-off. The metal pads are located far away from the gap (µm distance, sketch not to scale). (c) The nanogap separating the Si electrodes is fabricated using EBL (positive tone resist) and RIE. (d) Finished nanogap electrode device, l denotes the nanogap length and w the nanogap electrode width. Reprinted (adapted) with permission from [117]. Copyright (2019) IEEE.

Lab 80 Plus). In that way, we produced an electrically conductive lead structure comprising an array of ten top silicon layer bars of widths w ranging from 5 µm to 200 µm, which are electrically separated from each other and act as the basis for the later fabricated electrode arrays. After the RIE step, the remaining resist was removed in a subsequent ultrasonic bath of acetone, followed by rinsing in isopropanol and dry-blowing with N_2. To provide ohmic contact to the highly doped Si lead structures we fabricated a row of Ti/Au metallic contact pads on top of the Si layer (Fig. 4.6 (b)). These pads of area $200 \times 200\,\mu m^2$ were prepared by a combination of photo-lithography (positive photo resist AZ5214E, MicroChemicals), a short dip in diluted HF (5%, 30 s) to remove the native oxide, and subsequent PVD of 10/100 nm Ti/Au (Leybold L560, max 0.2 nm/s), followed by lift-off in an acetone bath, rinsing in isopropanol and dry-blowing with N_2. EBL was used to prepare the etching mask for gap fabrication. After cleaning the samples by sonication in acetone (10 min), followed by sonicating them in isopropanol and dry-blowing with N_2, and an additional cleaning step in oxygen plasma (60 s, 400 W, 50 Pa) the sample chips were coated with positive-tone EBL resist (90 nm, AR-P 6200, Allresist) and exposed in an EBL system (30 kV acceleration voltage, e_LINE, Raith). After developing (60 s, AR 600-546, Allresist) the samples were baked on a hotplate at 130 °C for 60 s to improve the

etching stability of the EBL resist. The resulting resist gap pattern was transferred into the top Si layer by RIE as previously described, eventually resulting in gaps in the silicon mesa (cf. Fig. 4.6(c) and 4.7(a), one between each pair of metal pads). The remaining e-beam resist was removed by subsequent sonication in acetone and isopropanol plus the additional application of an oxygen plasma (5 min, 400 W). The resulting nanogap electrode device with nanogap channel length l and electrode width w is shown in Fig. 4.6(d). In this way, each top silicon layer bar of the mesa was split in ten electrode pairs resulting in an array of 100 electrode pairs in total, on each sample. Fig. 4.7(a) shows an optical microscope imgage (top-view) of a part of such a nanogap electrode array sample chip. The nanogap is clearly visible as a dark line in-between contact areas in the inset magnification. Fig. 4.7(b) shows a SEM image (top-view) of a part of a $l \approx 40$ nm long single nanogap with sharp and clearly defined edges.

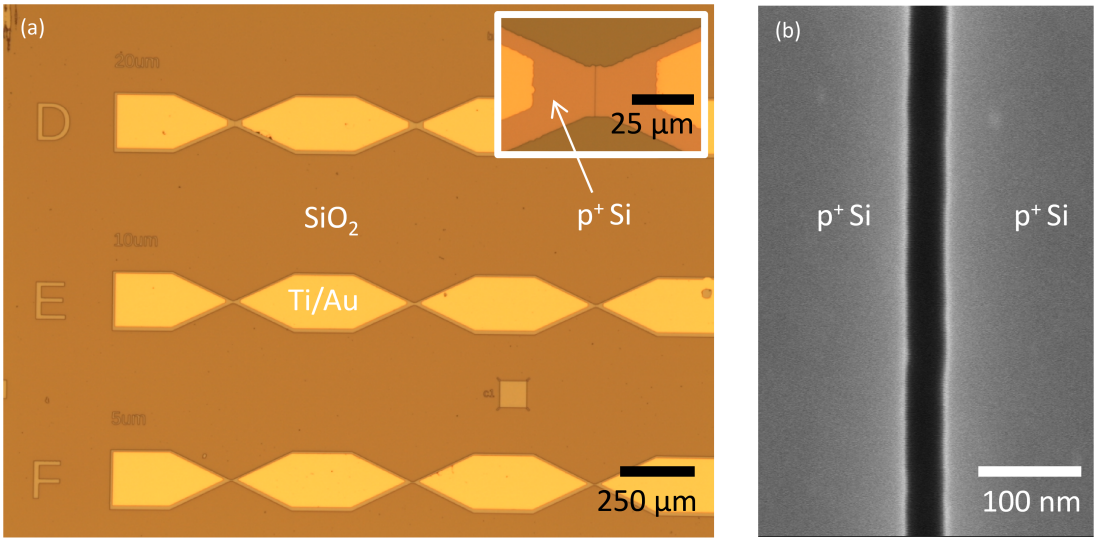

Figure 4.7 (a) Optical microscope image of a part of a sample chip with several gaps arranged in line, pairwise sharing electrical contacts. Gap widths vary from 20 µm to 5 µm in the image (top to bottom row). Magnification: The gap can be recognized as a dark line in-between contact areas. (b) SEM image (top-view) of part of a single nanogap with $l \approx 40$ nm after RIE etching.

4.2.2 Optimization of nanogap etch depth and channel length

This Section is based on the published conference proceeding: Silicon Nanogap Electrode Engineering for Organic Monolayer Field Effect Transistors [117] (Simon Pfaehler et al., 2019 IEEE 19th International Conference on Nanotechnology (IEEE-NANO) (Macao, China). IEEE, 2019, 521–525, DOI: 10.1109/NANO46743.2019.8993870.)[3]

We studied the RIE depth of the Si nanogap electrodes by controlling the etching time t while keeping all other parameters constant. Having precise control over the etch depth is a key factor

[3]Reprinted (adapted) with permission from [117]. Copyright (2019) IEEE.

for the successful fabrication of the nanogap devices besides e.g. the geometry of the etch profile. On the one hand, Si must be completely etched away in the gap area to completely separate the electrodes. On the other hand, the buried SiO_2 should be etched as little as possible to align the bottom of the nanogap with the lower edge of the Si device layer. This way, an optimal charge injection from the Si electrodes into the later filled-in materials under investigation in the nanogap may be expected (particularly in case of SAMs). The etch rate of the EBL resist limits the applicable maximum etch time. We measured the etch depth on reference samples which are fabricated as described above but using a pattern of big squares ($90 \times 90\,\mu m^2$) and additional wide trenches (w: mm scale) with same channel lengths l as the nanogap electrode devices. Fig. 4.8 summarizes the etch depth for $t = 10\,s - 40\,s$ in Si (black)

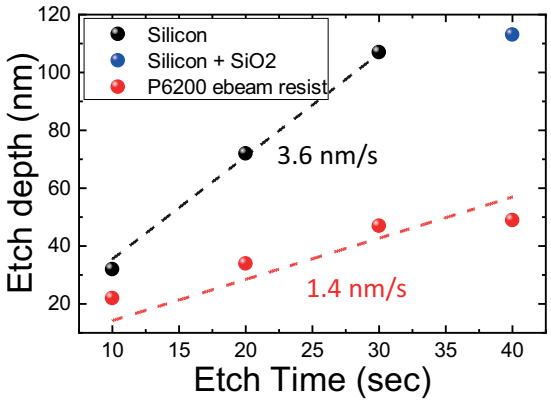

Figure 4.8 Etch series of the Si top layer and of the EBL resist layer using a SF_6/C_4F_8 based RIE plasma, with measured etch rates. Reprinted (adapted) with permission from [117]. Copyright (2019) IEEE.

and in the EBL resist (red), measured with a profilometer. There is only little increase in the etch depth for t longer than $\sim 35\,s$, because most of the Si is already etched and the buried oxide is etched much slower due to the different etch rates. This is also visible in the SEM images in Fig. 4.9: at $t = 30\,s$ (b) almost all Si is etched but at $t = 40\,s$ (c) only very little of the buried SiO_2 is etched. On the other hand, etch times in the range of $t = 20\,s$ (a) are cleary too short to etch the nanogap down to the buried SiO_2 layer. The dashed lines in Fig. 4.8 are linear fits to the data. From the slopes, measured etch rates are for Si $r_{Si} = 3.6\,nm/s$ and for the EBL resist $r_{P6200} = 1.4\,nm/s$, respectively, resulting in an etch selectivity of

$$\frac{r_{Si}}{r_{P6200}} \approx 2.6$$

Hence, the $\sim 90\,nm$ thick resist used is sufficient to withstand etching up to $\sim 60\,s$.
Another relevant fabrication parameter besides the etch depth is the nanogap length which defines directly the channel length l of the Si nanogap electrode device. We adjusted l by carefully controlling the EBL parameters. Fig. 4.10 shows the cross-sectional SEM images of

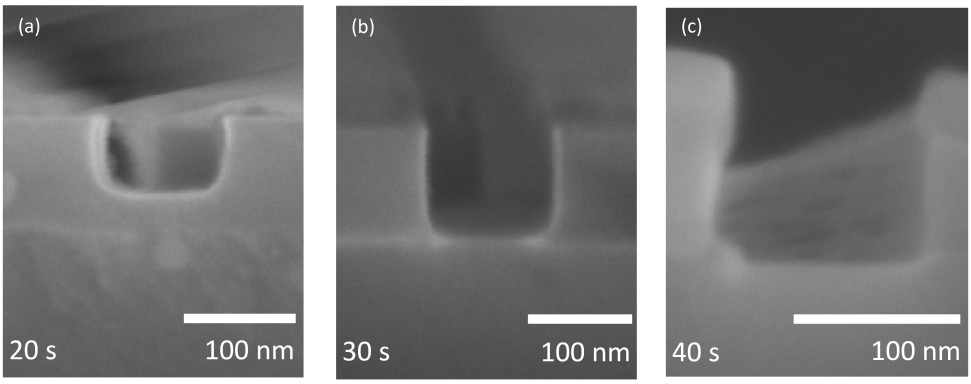

Figure 4.9 SEM cross section images of $l = 100\,\text{nm}$ long nanogaps which are etched for 20 s, 30 s and 40 s ((a), (b) and (c)), respectively, into the Si top layer. Reprinted (adapted) with permission from [117]. Copyright (2019) IEEE.

nanogap reference samples, fabricated as described above with wide trenches but same l as the nanogap electrode devices. While in Fig. 4.10 (a) and (b) the EBL resist layer was already removed after etching, it is still present in (c) and (d) as indicated on top of the Si device layer. As visible in Fig. 4.10, our RIE process generally resulted in a vey good anisotropic etch profile. Fig 4.10 (a)–(c) show nanogaps with $l = 200\,\text{nm}$, 100 nm and 60 nm which were exposed using

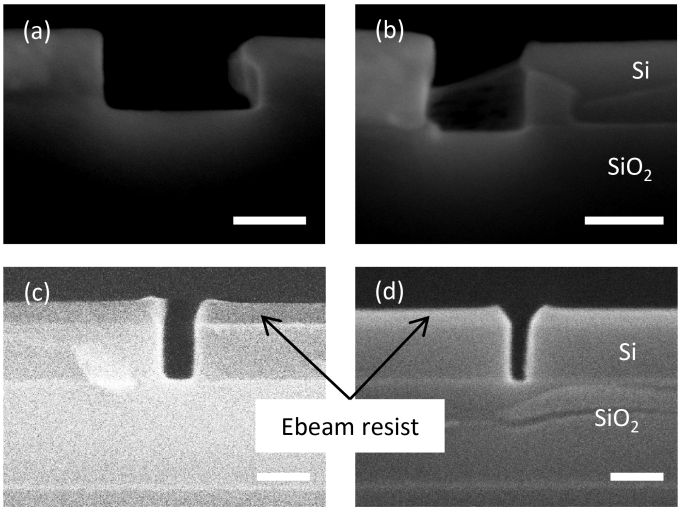

Figure 4.10 SEM cross section images of Si nanogap electrodes with different channel length l fabricated by ebeam lithography and reactive ion etching. (a) $l = 200\,\text{nm}$, (b) $l = 100\,\text{nm}$, (c) $l = 60\,\text{nm}$, (d) $l = 30\,\text{nm}$. All scale bars are 100 nm. Reprinted (adapted) with permission from [117]. Copyright (2019) IEEE.

an EBL exposure dose of $200\,\mu\text{C/cm}^2$ ((a), (b)) and $110\,\mu\text{C/cm}^2$ (c) respectively and a RIE time of $t = 40\,\text{s}$. We used an EBL write field size of $200 \times 200\ \mu\text{m}^2$ and the area exposure mode of the EBL system that uses multiple parallel lines of e-beam exposure to achieve the lithography pattern. In this way we were able to successfully fabricate nanogaps with $l \geq 60\,\text{nm}$. However, nanogaps with $l < 60\,\text{nm}$ could be only achieved using the single pixel line (SPL) mode of

the EBL system which in contrast to the area mode exposes only a single line pixel per pixel. The nanogap length is therefore not controlled by the number of exposure lines and hence the geometry of the area pattern but directly by the exposure dose of a single pixel. We achieved nanogaps as small as $l = 30\,\mathrm{nm}$ using the SPL mode and an ebeam exposure dose of $400\,\mathrm{pC/cm}$ as shown in Fig. 4.10 (d). In this case we used a RIE time of $t = 45\,\mathrm{s}$, since we observed slightly slower etching rates of Si for these small nanogaps, presumably because of less efficient transport of etched material due to the increased aspect ratio d/l.

4.3 Filling the nanogap electrodes with silicon nanocrystals

We devoted much effort to the controlled and reproducible filling of the nanogap with SiNCs. Few procedures have been reported in the literature, demonstrating the filling of (metallic) nanoscale trenches by different approaches [67, 118]. We tried several alternative methods, such as spin coating, drop casting or solvent evaporation to fill the nanogaps. However, none of these techniques led to satisfying filling with a homogeneous thin film of SiNCs. By far, the best results were obtained by mechanically pressing the SiNCs from solution into the gap, employing a pressure-transducing PDMS membrane. This novel approach, particularly developed for this purpose, turned out to enable the formation of homogeneous SiNCs thin films with precise control of thickness.

4.3.1 Nanogap filling by spincoating

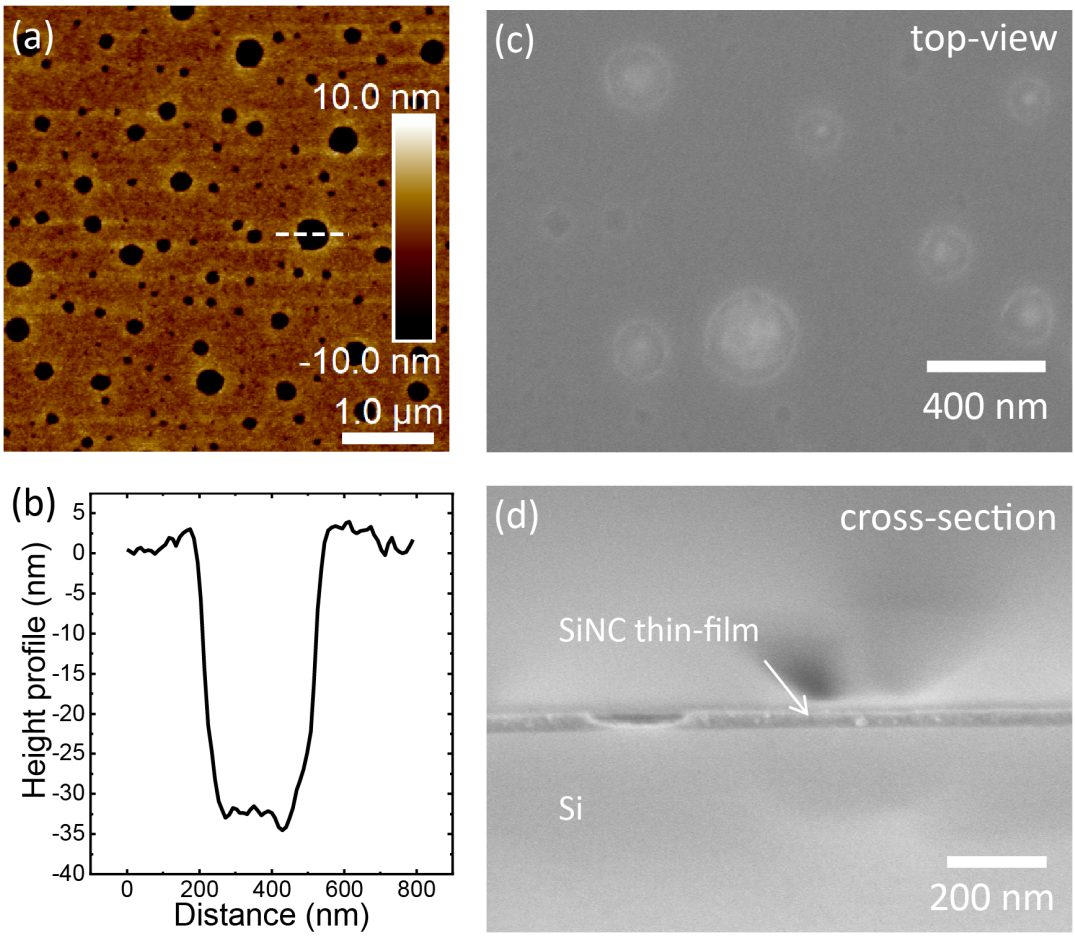

Figure 4.11 (a) AFM image of a SiNC thin film on top of a Si substrate, spin coated from toluene solution. (b) Corresponding height profile along the path indicated as white dashed line in (a). (c)SEM top-view image of the same sample as in (a) and corresponding cross sectional SEM image of the SiNC thin film (d).

Spin coating is one of the well known standard methods to fabricate uniform thin films on planar substrates, e.g., for photo resist layers in lithography processes. Thin films of NCs were also fabricated successfully by spin coating [119–121]. We tried therefore to fabricate homogeneous thin films of SiNCs by spin coating to fill the nanogaps reliably. Fig. 4.11(a) shows an AFM image of such a SiNC thin film spin coated from a $c = 5\,\mathrm{mg/ml}$ SiNC solution (toluene) at 600 rpm for $t = 90\,\mathrm{s}$. No homogeneous thin film is observed because of several circular holes in the film with diameters ranging from a couple of 10 nm up to several 100 nm, as it is also visible in the corresponding SEM top-view image in Fig. 4.11(b). The depth of these holes is comparable to the thin film thickness as it can be seen in the AFM height profile Fig. 4.11(c) for a line scan along the indicated white dashed line in (a) and also in the cross-sectional SEM image in Fig. 4.11(d). We tried several different spin coating speeds in the range of 350 rpm to 2500 rpm without achieving a homogeneous and continuous thin film, which is not beneficial to fill all gaps of our nanogap electrode array which are distributed over the whole sample surface.

4.3.2 Nanogap filling by drop casting

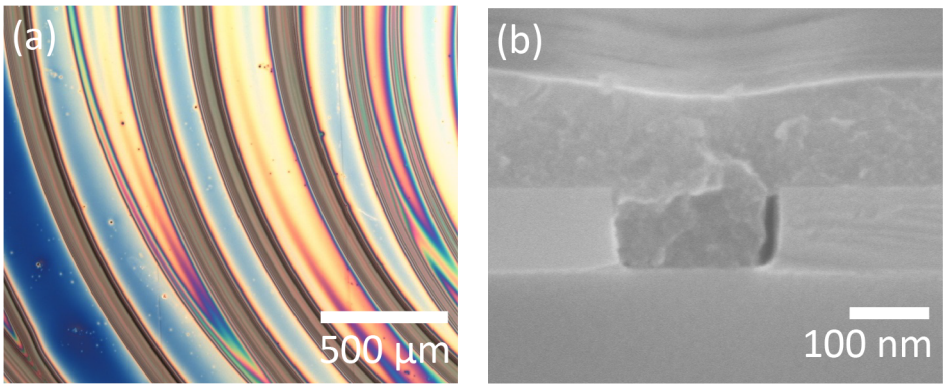

Figure 4.12 (a) Optical microscope image of a drop casted SiNC thin film on top of a SOI sample. (b) Cross-sectional SEM image of a 200 nm long nanogap filled with SiNCs via drop casting.

Another approach to fill the nanogaps with thin films of SiNCs is to simply drop cast the SiNC solution on the sample surface, using a pipette and let the solvent evaporate. As it can be seen in the optical microscope image in Fig. 4.12(a) the drop casted thin film exhibits rather a hilly, ring like surface morphology than a homogeneous and flat surface. These ring structure of the droplet originated most likely from the coffee ring effect [122]. While the solvent of the SiNC solution droplet evaporates, the dissolved SiNCs are transported to the perimeter of the droplet. As a result, the ring like structure is formed on the sample surface. More importantly, the drop casted thin film is not homogeneously filling the nanogaps as visible in the cross-sectional SEM image in Fig. 4.12(b). At the right sidewall, there is a void between the film and the Si wall which impairs reliable charge carrier injection from the Si electrode into the SiNC thin film. Similar observations have been made for dip-coated thin films where the samples were dipped

perpendicular for a couple of seconds in the SiNC solution and subsequently taken out of the solution.

4.3.3 Nanogap filling by vertical evaporation

Since dip-coated films produced very thin films (in the order of 10 nm or less), we tried the reverse process: keeping the perpendicular sample at a fixed height position in the SiNC solution and waiting until the solvent was evaporated as schematically shown in Fig. 4.13(a). The solvent evaporation needed typically ≈ 24 h until the solvent level was below the sample. The complete coating process was done in a glovebox to prevent the SiNCs from oxidation. The finished SiNC thin film surface showed a repeating thickness variation pattern, visible as alternating stripes in the optical microscope image of Fig. 4.13(b). Most likely these thickness pattern originates from mechanical vibrations, introduced by the glovebox pump which regulates the pressure of the inert atmosphere in the glovebox in regular time intervals. A control sample coated by vertical evaporation outside the glovebox in a fume hood did not show the stripe like thickness pattern on the surface. The vertical evaporation method produced thick SiNC films of the order of 1 µm as shown in the cross-sectional SEM image of a filled nanogap (l = 200 nm) in Fig. 4.13(c) with visible cracks in the film. Furthermore, in the nanogap itself, there are voids in the vicinity of the Si sidewalls, similar to the drop casting coating method as described in Section 4.3.2.

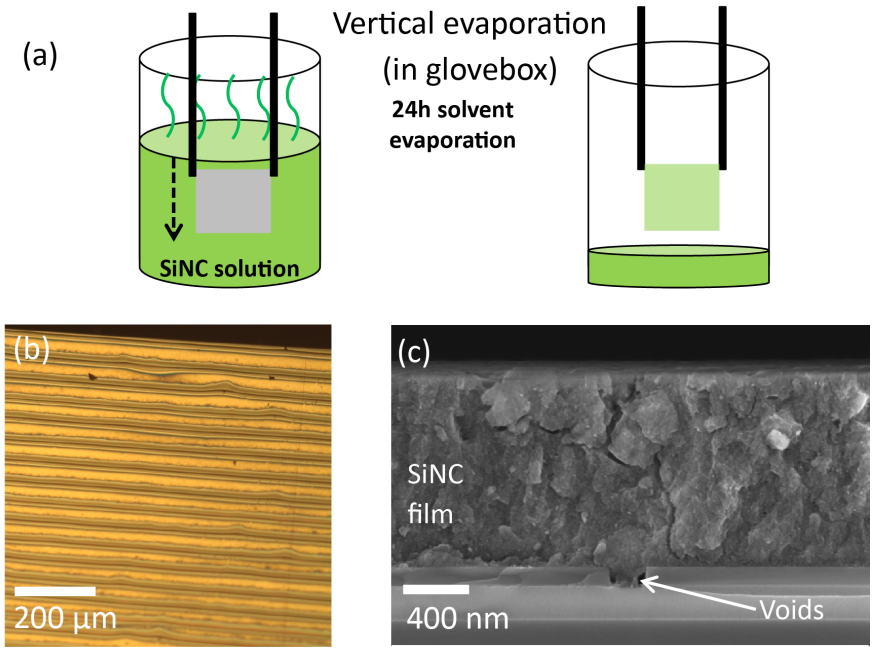

Figure 4.13 (a) Schematic of the coating process by vertical evaporation: The sample is vertically placed in the SiNC solution and coated while the solvent slowly evaporates. (b) Optical microscope image of sample surface after coating by vertical evaporation. (c) Cross-sectional SEM image of a nanogap sample coated with a film of SiNC by vertical evaporation.

4.3.4 Nanogap filling via a pressure-transducing PDMS membrane

The following Section is based on the published article: Space charge-limited current transport in thin films of alkyl-functionalized silicon nanocrystals [116] (Simon Pfaehler et al., Nanotechnology, 30(39) (2019), 395201, DOI: 10.1088/1361-6528/ab2c28)[4].

By far the best coating results were obtained by mechanically pressing the SiNCs from solution into the gap, employing a pressure-transducing PDMS membrane. This filling process of the active gap region between the contacts with a thin film of SiNCs is outlined in Fig. 4.14 in the case of Hex-SiNCs. This novel approach, particularly developed for this purpose, turned out to enable the formation of homogeneous Hex-SiNCs thin films with precise control of thickness, without any voids or cracks in-between the Si electrodes.

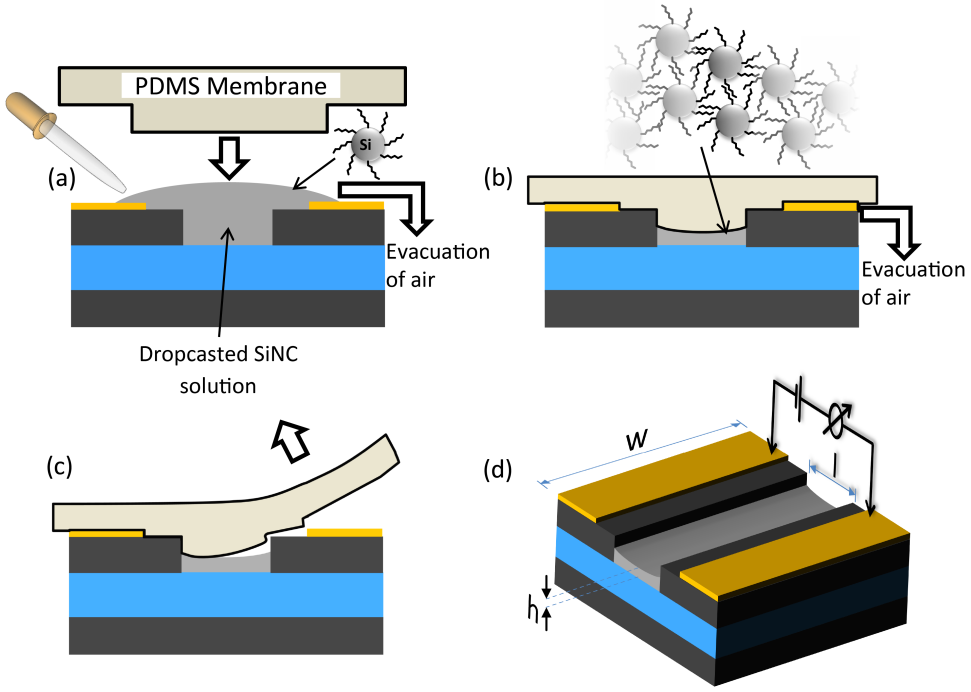

Figure 4.14 Schematic representation of nanogap filling with Hex-SiNCs. (a)-(c) Filling the gap between electrodes with a thin film of Hex-SiNCs by mechanically pressing the Hex-SiNCs from solution via a pressure-transducing PDMS membrane. (d) Final device structure for electrical characterization. Dimensions of the film are indicated as w (width), l (length) and h (height). Reprinted (adapted) from [116]. Copyright (2019) IOP Publishing Ltd, CC BY 3.0 license.

To achieve this, the samples were first cleaned by sonication in acetone (10 min, VLSI Selectipur, BASF), subsequent sonication in isopropanol (VLSI Selectipur, BASF) and dry-blowing with N_2, followed by a short dip in diluted HF (2%, 30 s) to remove the native oxide from the silicon electrodes' surface, right before the coating with Hex-SiNCs solution. Next, about 70 µl Hex-SiNCs solution was immediately drop-casted onto the sample covering the complete surface

[4]Reprinted (adapted) from [116]. Copyright (2019) IOP Publishing Ltd, Creative Commons BY 3.0 license (http://creativecommons.org/licenses/by/3.0)

(Fig. 4.14(a)). We used a custom-made device originally designed for nano-imprint lithography to mechanically press the Hex-SiNC solution via a pressure-transducing PDMS membrane into the gaps (Fig. 4.14(b)). The membrane was fabricated by mixing base and curing agent (Sylgard 184 silicon elastomer kit, Dow Corning) in a weight ratio of 5 : 1, evacuating the mixture in a desiccator to remove air bubbles and curing it for 48 hours at room temperature. In order to mechanically press the Hex-SiNC solution into the gaps, the volume between the PDMS membrane and the wetted sample surface was evacuated by a standard membrane vacuum pump, such that the PDMS membrane got into close contact with the sample surface. Thus, the solvent of the drop-casted Hex-SiNC solution on the sample was removed mainly by pumping but also to a little amount by being soaked by the PDMS membrane while mechanically pressing the Hex-SiNCs as a thin film into the gap separating the electrodes. No remaining solvent could be observed after 4 min of evacuation and having carefully released the PDMS membrane from the sample surface (Fig. 4.14(c)). For every sample we used a newly prepared, fresh piece of the same PDMS membrane. After release, the samples were heated on a hotplate to 100 °C for 60 s to evaporate remaining residues of the solvent. To investigate the quality and filling height of the Hex-SiNC thin film in the gap between electrodes, we used reference samples based on the same SOI material and fabricated a set of six very wide ($w \approx 7$ mm) gaps per reference sample by EBL and RIE using the same fabrication and PDMS membrane coating protocol as for the gap electrodes array samples described before. All reference samples were coated with Hex-SiNCs solutions from the same batch that was used for the coating of the gap electrode samples.

Multilayer approach

In order to gain control over the thin film thickness h, we first tried to repeat the SiNC coating cycle multiple times to increase h. Fig. 4.15 shows SEM cross-section images of nanogap test structures ($l = 100$ nm) filled with multiple layers of Hex-SiNCs from the same solution ($c = 5$ mg/ml) as described before using our PDMS membrane technique. Each layer was pressed into the gap with a fresh piece of the same PDMS membrane.

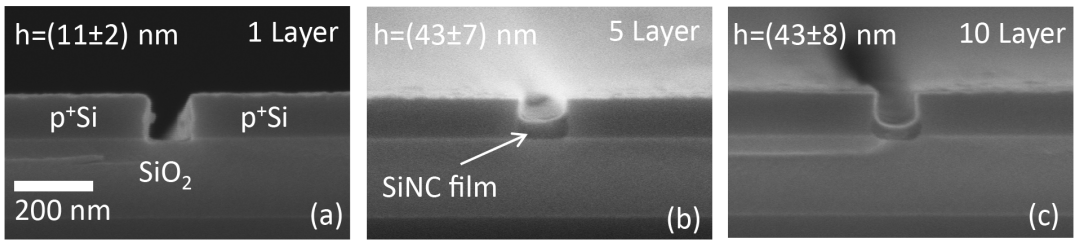

Figure 4.15 SEM cross section images of Si nanogaps ($l = 100$ nm) filled with thin films of Hex-SiNC prepared by multiple successive coating layers from a solution with concentration $c = 5$ mg/ml. Indicated thin film thicknesses are based on at least six measured test structures. (a) 1 layer: $h = (11 \pm 2)$ nm, (b) 5 layers: $h = (43 \pm 7)$ nm and (c) 10 layers: $h = (43 \pm 8)$ nm.

In general, the film shape adopted a concave form inside the gap. Here, we determined the (minimum) film thicknesses h from measuring in the middle of the cross section of the gap, as depicted in Fig. 4.14(d). For the sample with 5 coating layers (Fig. 4.15(b)), a thin film thickness of $h_{5L} = (43 \pm 7)$ nm is measured which is about half the hight of the nanogap. Compared to the case of only one coating layer ($h_{1L} = (11 \pm 2)$ nm, Fig. 4.15(a)), this is a clear increase in h. But as visible in Fig. 4.15(c), about the same thickness of $h_{10L} = (43 \pm 8)$ nm is measured for 10 coating layers. We measured large variations of h for several samples in different coating runs with multiple coating layers without clear trend and without gaining precise control over the thin film thickness. Since the same solvent (toluene) was used for every coating layer, it is likely that the solvent dissolved to some extent SiNCs from the surface of the previously coated layer in the nanogap which circumvents control over the overall thin film thickness.

SiNC solution concentration approach

Instead of using a fixed concentration and repeating the SiNC coating multiple times, the level of gap filling can be efficiently adjusted by the concentration of SiNCs in solution. As shown in the SEM cross-sectional images of Fig. 4.16, the thin film thickness (h) in the gap increases monotonically with the solution concentration of the Hex-SiNCs, which was varied from $c = 5, 10, 15$ to 20 mg/ml (Fig. 4.16(b)–(e), respectively). Fig. 4.16(a) was treated according to the same coating protocol, but with the pure solvent without any Hex-SiNCs. No Hex-SiNC thin film could be observed in this case which shows that the otherwise observed thin films consist of Hex-SiNCs.

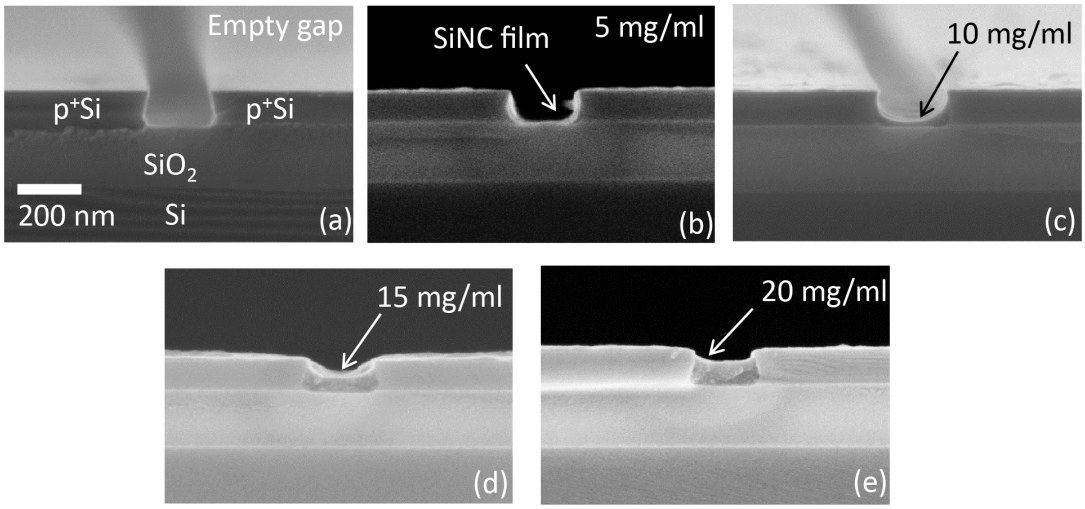

Figure 4.16 (a)–(e) SEM cross section images of Si nanogaps filled with thin films of Hex-SiNC prepared from increasing solution concentrations, resulting in increasing thin film thicknesses. Reprinted (adapted) from [116]. Copyright (2019) IOP Publishing Ltd, CC BY 3.0 license.

Fig. 4.17 summarizes the measured film thickness as function of Hex-SiNC solution concentration, starting from a thin film with $h \approx (15 \pm 3)$ nm up to an almost completely filled gap with $h = (92 \pm 8)$ nm. All resulting Hex-SiNC thin films filled the gap in a homogeneous manner, free from voids or cracks in the film or close to the interface to the electrodes. This is an important requirement for stable and reproducible electrical measurements.

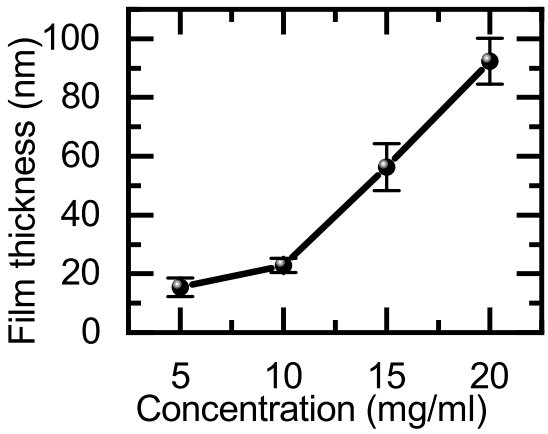

Figure 4.17 Averaged thin film thicknesses as a function of Hex-SiNC concentration, measured in filled 200 nm gaps. All film thicknesses were obtained from averaging the measurement results of at least six test structures comprising wide (mm scale) trenches, for each Hex-SiNC solution concentration. Reprinted (adapted) from [116]. Copyright (2019) IOP Publishing Ltd, CC BY 3.0 license.

The PDMS concentration-dependent coating method produced homogeneous thin films over a large part of the sample surfaces as shown in the optical microscope images of Fig. 4.18. For all concentrations of 5 mg/ml, 10 mg/ml, 15 mg/ml and 20 mg/ml (Fig. 4.18 (a)–(d)), there is a homogeneous part of the Hex-SiNC thin film in the middle of the sample surrounded by a hill like boundary which originates directly from the PDMS coating process: While the pump is evacuating the space above the the sample surface, the PDMS membrane is bended downwards due to the decreased pressure and reaches the sample surface directly in the middle of the surface, rolling subsequently to the sample edges which piles up the SiNCs at the edges. For this reason, only nanogap electrode devices in the middle part of each sample were used electrically to ensure consistent thin film quality and a controlled filling of the nanogap electrode devices as it is demonstrated in the AFM image of Fig. 4.19, showing a nanogap coated with Hex-SiNC from a 20 mg/ml solution.

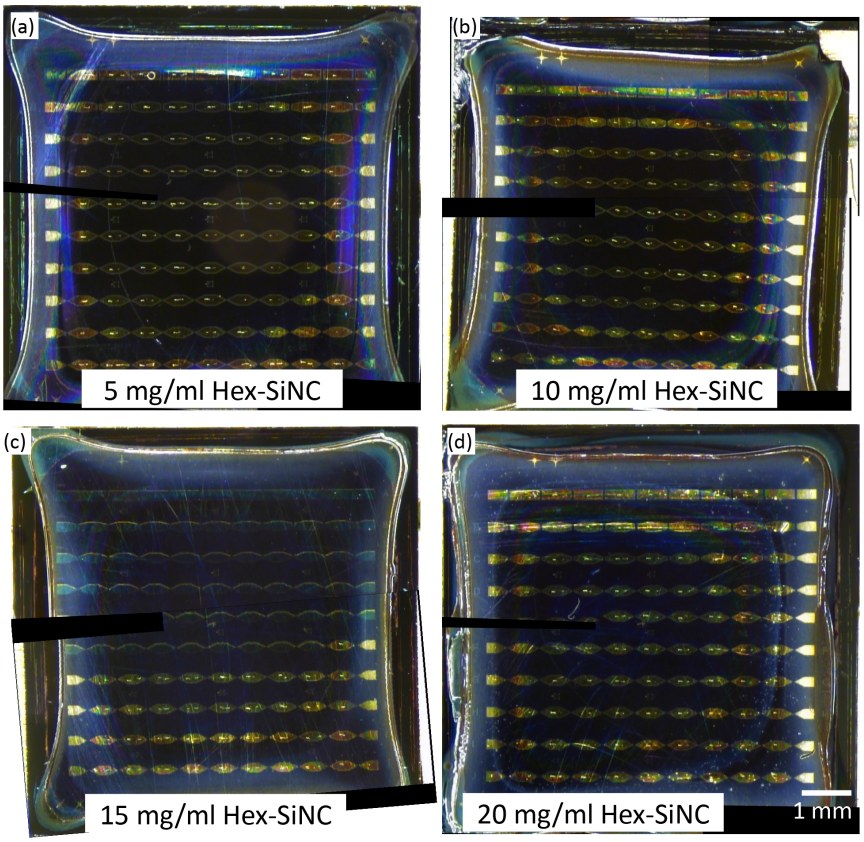

Figure 4.18 Stitched optical microscope images of nanogap sample chips coated with Hex-SiNCs from solution of various concentration via a pressure transducing PDMS membrane. (a) $c = 5\,\mathrm{mg/ml}$, (b) $c = 10\,\mathrm{mg/ml}$, (c) $c = 15\,\mathrm{mg/ml}$ and (d) $c = 20\,\mathrm{mg/ml}$. The black stripes are image errors due to the stitching process and not related to the samples.

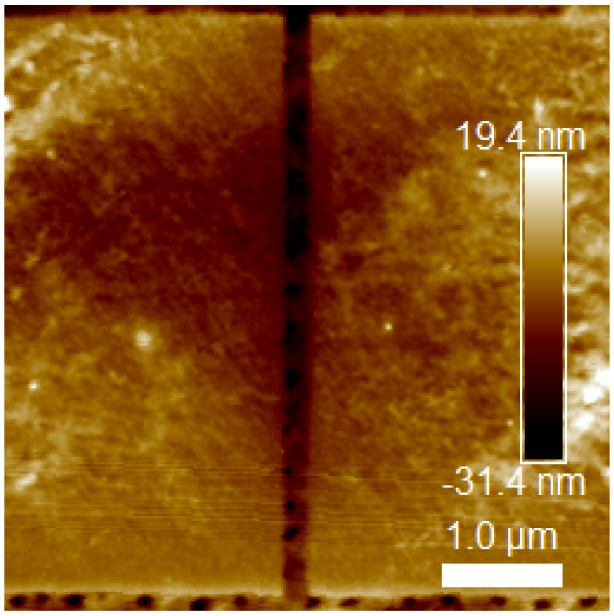

Figure 4.19 AFM image of a nanogap ($w = 5\,\mu\mathrm{m}$, $l = 200\,\mathrm{nm}$), filled with Hex-SiNCs from $20\,\mathrm{mg/ml}$ solution via a pressure transducing PDMS membrane.

5 Current transport in thin films of functionalized silicon nanocrystals

In the following Chapter, current transport through thin films of functionalized SiNCs is studied. In the first two Sections, the obtained current-voltage (I-V) data of the Si nanogaps coated with functionalized SiNCs is presented and discussed. We complement our data with a kinetic Monte Carlo simulation of the obtained charge transport process in the third Section. The Chapter is concluded with the discussion of additional I-V measurements on planar samples coated with SiNCs by using a hanging Hg droplet electrode, as well as impedance measurements and the presentation of the obtained film composition via XPS measurements.

In this Chapter, Sections 5.1, 5.2 and 5.6 are based on the published article: Space charge-limited current transport in thin films of alkyl-functionalized silicon nanocrystals [116] (Simon Pfaehler et al., Nanotechnology, 30(39) (2019), 395201, DOI: 10.1088/1361-6528/ab2c28)[1].

5.1 Current voltage spectroscopy on SiNC thin films filled in Si nanogap electrodes

We characterized the prepared SiNC films of different filling height h electrically, by measuring the DC I-V characteristics across the filled nanogaps. We measured in total 116 nanogap devices on several samples coated via the pressure transducing PDMS membrane technique with thin films of Hex-SiNC, PA-SiNC and Phen-SiNC, prepared form solution concentrations of 5 mg/ml to 20 mg/ml from several SiNC batches. The nanogap channel length l of all measured nanogap devices was in the range of (39 ± 2) nm to (215 ± 7) nm, while their widths w varied from 5 µm to 50 µm. Before measuring the coated samples, all devices were pre-characterized in their as-fabricated state, i.e., without any SiNC film filling. Only those fabricated devices with measured currents less than 1 pA at an applied voltage of 30 V (i.e., with insulating gap) were taken into further consideration for filling with SiNC films (see Fig. 5.1(a), grey curve, for such a reference measurement).

[1] Reprinted (adapted) from [116]. Copyright (2019) IOP Publishing Ltd, Creative Commons BY 3.0 license (http://creativecommons.org/licenses/by/3.0)

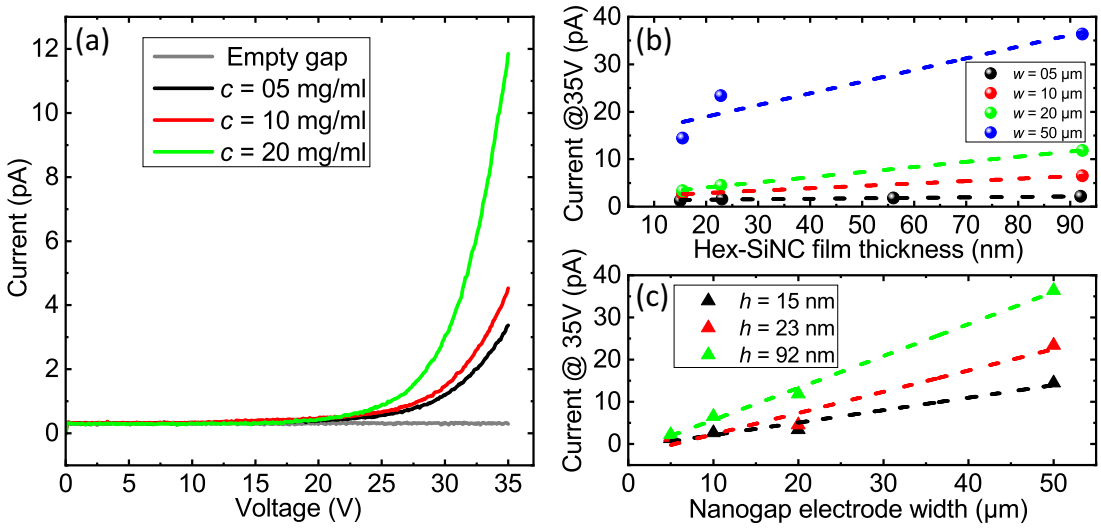

Figure 5.1 (a) *I-V* characteristics for nanogap devices with $w = 20\,\mu m$ and $l = (206 \pm 11)\,nm$, filled with films of Hex-SiNCs that were prepared from different solution concentrations. Data shows the first bias scan from zero to 35 V, averaged over two individual devices. (b) Current at 35 V as function of Hex-SiNC thin film thickness for devices with widths 5 µm, 10 µm, 20 µm and 50 µm. The dashed lines are linear fits to the data points. (c) Current at 35 V as function of gap widths for different Hex-SiNC film thicknesses. The dashed lines are linear fits to the data points. Reprinted (adapted) from [116]. Copyright (2019) IOP Publishing Ltd, CC BY 3.0 license.

Fig. 5.1(a) shows the *I-V* characteristics of $w = 20\,\mu m$ broad nanogap devices with $l = (206 \pm 11)\,nm$ and filled with Hex-SiNC films, prepared from different solution concentrations of 5 mg/ml, 10 mg/ml and 20 mg/ml that resulted in thin film thicknesses of about h =15 nm, 23 nm and 92 nm, respectively. After filling the gaps with these thin films, all devices showed a pronounced non-linear increase in current with increasing voltage, when compared to the empty, insulating device directly after fabrication. With increasing thin film thickness, a larger current was measured over the entire voltage range. By evaluating the first-scan data from 24 gap devices in total, we could determine the dependence of current as function of film thickness and channel width as shown in Figs. 5.1(b) and (c). Measured currents increased monotonically, roughly linearly as a function of film thickness and channel width, suggesting the well-defined, homogeneous filling of the gaps up to their edges.

We note that the displayed curves are all averages from the very first bias scans from zero to 35 V. The reason for this choice of first curves was a pronounced hysteretic *I-V* behavior, which was observed for all investigated samples. By selecting the same (first) traces, all samples with different filling could be compared. The hysteretic behavior led to notable differences for consecutive forward and backward scans, carried out between the minimal (0 V) and maximal applied voltage. Fig. 5.2(a) shows the *I-V* traces of three subsequent scans as an example. As additionally apparent, for subsequent bias scanning cycles the overall reached maximum currents successively decreased, until typically after some twenty cycles the currents had already dropped by $\sim 80\,\%$ (cf., 5.2(b)).

We note that all measured currents correspond to a very low conductance regime, with values

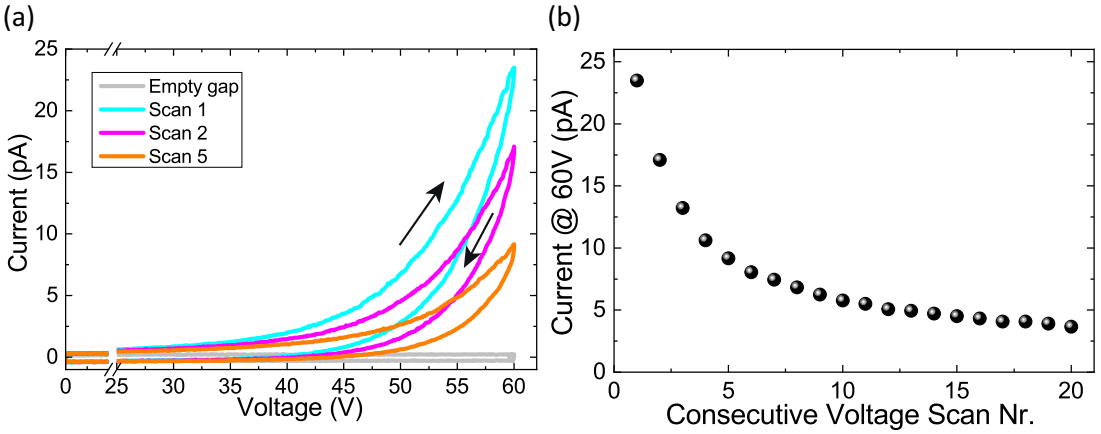

Figure 5.2 (a) Three consecutive *I*-*V* scans measured for a Hex-SiNC coated device with $l = 200$ nm and $w = 20$ µm, prepared with a 5 mg/ml Hex-SiNC solution. The black arrows indicate the scan direction for the example of the first scan. (b) Maximal measured currents at $V = 60$ V of each consecutive voltage scan of the same device as in (a).

in the range of 10 pA or below, at 35 V. Yet, our study revealing the monotonic, approximately linear dependence of current as a function of film thickness and gap width indicates that charge transport presumably takes place homogeneously through the Hex-SiNC layer.
Generally, we observed the decreasing current phenomenon for all measured samples and SiNC types. A 100 nm long and 5 µm broad nanogap device which was filled with Hex-SiNCs from a 20 mg/ml solution was used to measure directly the time-dependent decreasing current exemplarily. The voltage was first increased from 0 V to 25 V and subsequently kept constant at 25 V while at the same time, the time-dependent current signal was measured for ~ 1 h, represented by the black curve in Fig. 5.3. Afterwards, the voltage was further increased to 30 V (red curve) and 35 V (green curve) while measuring the time dependence of the current for ~ 1 h respectively. In all cases, the current decreased rather exponentially without pronounced saturation during the measured time interval.

Beside thin films of Hex-SiNCs, we measured additionally PA-SiNC and Phen-SiNC coated nanogap devices of different gap length. Fig. 5.4 gives an overview about the obtained *I*-*V* curves and the dependence of *I* on the channel length for all SiNC types. Here, all *I*-*V* data correspond to nanogap devices with $w = 5$ µm and SiNC coatings from 20 mg/ml solution concentration. Fig. 5.4(a) depicts the *I*-*V* curves for Hex-SiNC filled nanogap devices with nominal channel lengths of 40 nm, 100 nm and 200 nm. The presented *I*-*V* curves are averaged curves from the first voltage scans for at least 3 devices respectively. As clearly visible from the plot, with decreasing channel length, a larger current was measured over the entire voltage range. The same trend was observed in case of the PA-SiNC and Phen-SiNC coated nanogap devices as depicted in Fig. 5.4(b). The longer the channel, the lower the observed current.

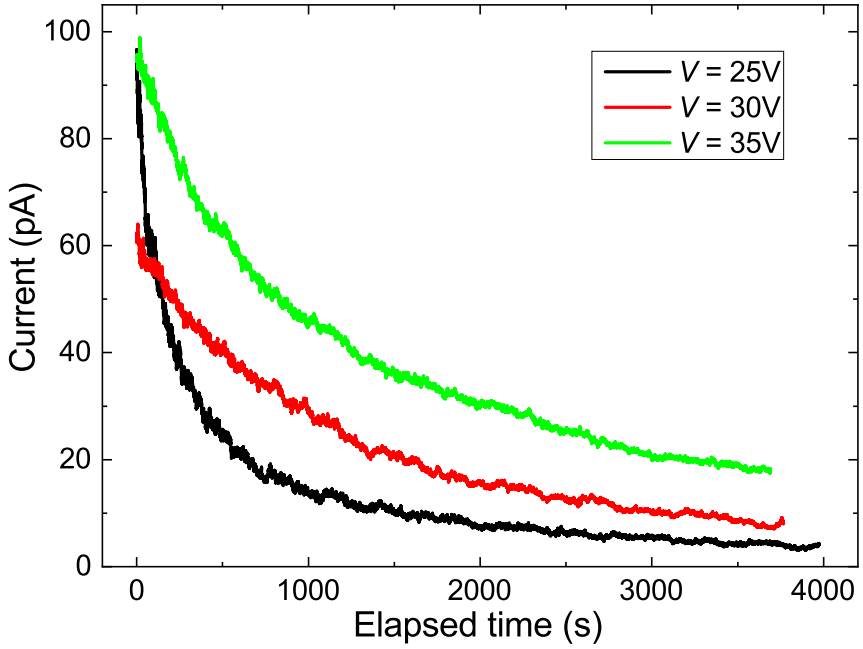

Figure 5.3 Time-dependent current signals after increasing the bias voltage to a fixed value of 25 V, 30 V and 35 V for a Hex-SiNC (c = 20 mg/ml) coated nanogap device with l = 100 nm and w = 5 µm.

We see no considerable difference in the I-V curves of same l when comparing PA-SiNC and Phen-SiNC. However, there is a significant difference of about one order of magnitude of these curves compared to the corresponding Hex-SiNC measurements. This is clearly visible in Fig. 5.4(c) and (d) which show the same data as (a) and (b) but depict the current density j instead if I. The low currents in case of PA-SiNC and Phen-SiNC are somehow surprising, since their aromatic moieties are not expected to limit charge transport but rather supporting it in comparison to the alkyl chains of Hex-SiNC. On the other hand there are multiple reasons which can limit the current transport in these films. Besides the film thickness and the spatial arrangement of the SiNCs in the thin film also their coupling to the electrodes as well as the overall film homogeneity are important factors, among others. In fact, we observed generally a poor film quality for PA-SiNC and Phen-SiNC compared to the Hex-SiNC films during SEM inspection: The nanogaps are less filled and the films showed generally more inhomogeneities (cf. Appendix A.2), possibly due to a poorer SiNC solution quality beause of a poorer solubility of PA-SiNC and Phen-SiNC in toluene.

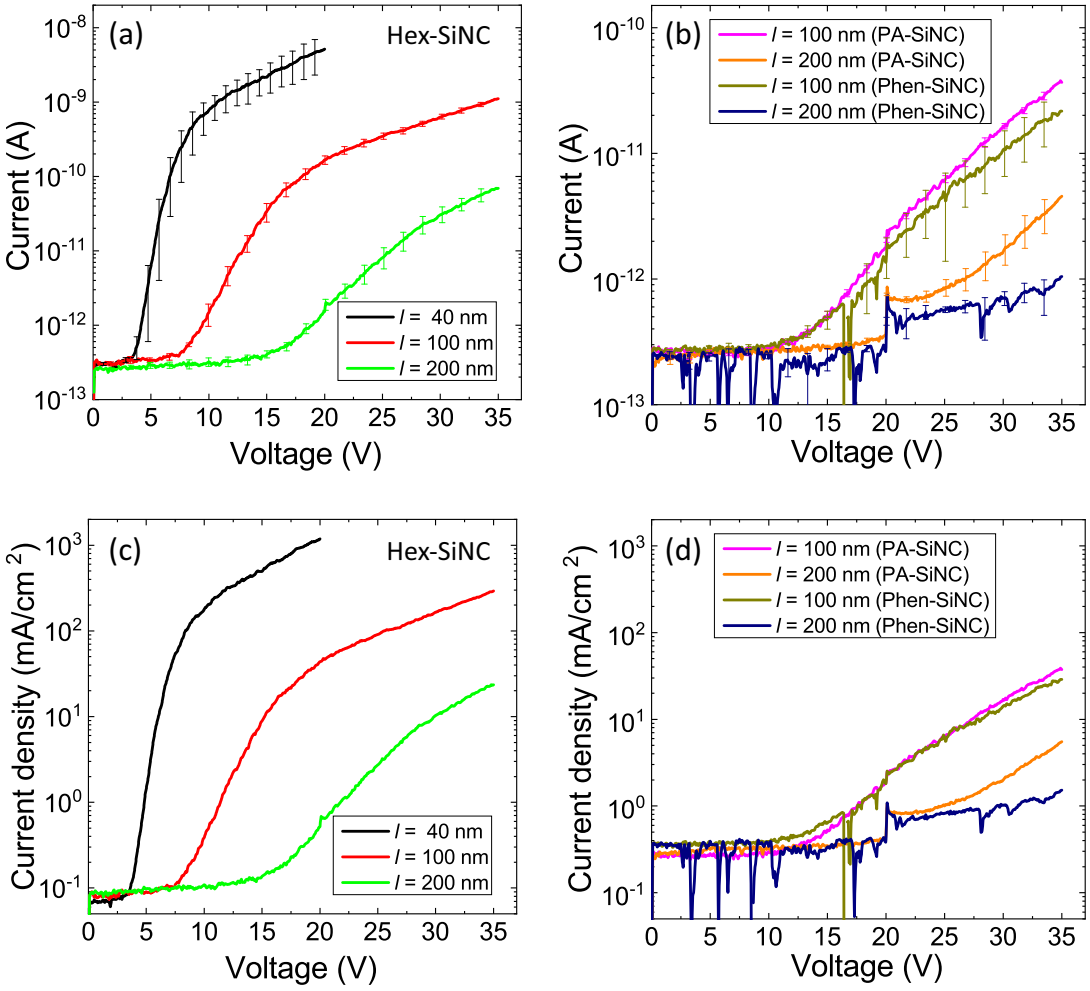

Figure 5.4 Averaged *I-V* curves from the first voltage scans of at least 3 devices respectively as function of nominal channel length and SiNC type with $w = 5\,\mu m$ and $c = 20\,mg/ml$. Error bars correspond to the standard error. (a) Hex-SiNC coated nanogap devices (l =40 nm, 100 nm and 200 nm). (b) *I-V* data of PA-SiNC and Phen-SiNC coated nanogap devices (l =100 nm and 200 nm). (c) same data as in (a) represented with corresponding current density. (d) same data as in (b) represented with corresponding current density.

The obtained channel length dependent *I-V* data of Hex-SiNC in Fig. 5.4(a) can be used to roughly estimate the specific conductivity in our Hex-SiNC thin films by using a simplified transmission line model (TLM) [123]. Fig. 5.5 depicts the resistance values, calculated for fixed voltages of 15 V, 17.5 V and 20 V versus l/A with the effective electrode area A which is calculated as $A = h \cdot w$ (with h obtained from cross-sectional SEM measurements). The inverse slope of the linear fits to the data (dashed lines) gives an estimation of the specific conductivity and is calculated in the range of $1 \times 10^{-9}\,\Omega^{-1}\,\mathrm{cm}^{-1}$ to $1 \times 10^{-8}\,\Omega^{-1}\,\mathrm{cm}^{-1}$, hence can be roughly compared with conductivities of materials such as intrinsic wide-band-gap semiconductors or insulators.

However, it needs to be noted that the measured *I-V* curves are highly non-linear which limits the correct application of the TLM. Hence, the extracted values can be only taken with care and can only serve as a rough approximation.

The intercept of the linear fit with the y-axis can be used as a rough estimation of the contact resistance of the nanogap device according to the TLM. As evident in Fig. 5.5, the resulting intercept values are negative which is due to the discussed limitations of applying the TLM model to our data. Nevertheless, the absence of a significant positive intercept value in our evaluation suggests, that our nanogap devices are not affected by substantial contact resistance effects.

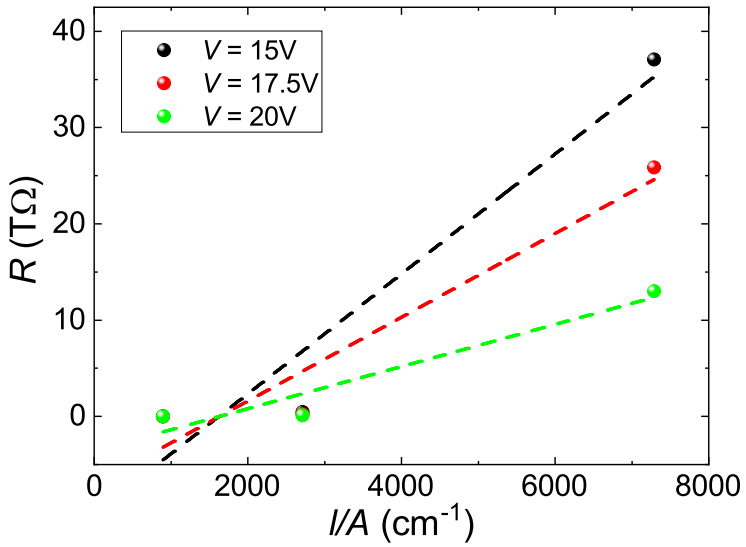

Figure 5.5 Resistance as function of effective electrode area A devided by l for constant voltages, respectively. The dashed lines are linear fits to the data.

5.2 Space charge limited current in thin films of hexyl functionalized SiNCs

Our charge transport medium consists of a randomly ordered network of (undoped) SiNCs which are separated in the case of Hex-SiNCs by surface bound hexyl molecules. The hexyl molecule thickness sets the SiNC-to-SiNC distance to a minimum of roughly 1.6 nm, assuming dense packing. This organic, insulating spacer represents a barrier for charge carriers to be transferred from SiNC to SiNC. For the traveling of charges over the total distance of the channel length, percolation paths across the randomly connected network of SiNCs are likely [36, 40, 120, 124]. The transport along these paths may involve a hopping-type of charge transport [125], Fowler-Nordheim tunneling [42], Pool-Frenkel conduction [43] or space-charge-limited-current (SCLC) transport [40]. If localized charges trapped within the semiconductor SiNCs may build up gradually with time under applied bias and continuous injection from the source, the overall resulting space-charge layer in the SiNC material will increasingly block subsequent charge injection. As a consequence, the resulting current at a fixed bias decreases with time. In fact, such a behavior has been observed for networks of oxidized or hydrogen-terminated SiNCs and explained within this framework [126]. The observed hysteretic behavior and particularly the successive degradation of current upon cyclic voltage ramping qualitatively agree with such SCLC mechanism, and first quantitative parameters may be extracted from the data. Fig. 5.6 displays the *I*-*V* traces of Fig. 5.1(a) in a double-log plot. In this representation, two voltage ranges can be identified with disparate slopes, corresponding to a current-voltage dependence of the form

$$I = aV + bV^m \tag{5.1}$$

with a, b, m being fitting parameters adjusted to the experimental data. In the SCLC theory, the first (linear) term refers to the low-bias regime where mostly quasi-free charge carriers would contribute. In this regime, the parameter a corresponds to the Ohmic conductance whereas for higher voltages the second term with the power law coefficient m dominates [127, 128]. In fact, from fitting our data to a general $I \sim V^n$ dependence at medium bias, we obtain exponents in the range $n = 0.8 - 1.6$, which is in reasonable agreement with dominating Ohmic conductance. At low bias (below 5 V) no current could be resolved above our experimental resolution limit. At higher bias, our measured currents follow a distinct super-linear increase with voltage. According to previous reports, $m = 2$ would correspond to the absence of traps (Mott-Gurney law [129]), while $m > 2$ would indicate the presence of traps. Exponents of $m = 2 - 3$ have been reported for hydrogen-terminated SiNCs [36], while values of up to $m \sim 5$ were observed for oxidized SiNCs [126] and amorphous silicon [130]. The analysis of our data in the high-bias regime yields high values of $n = 5.9 - 8.6$. We assign this finding to a potentially high density of trap centers [127].

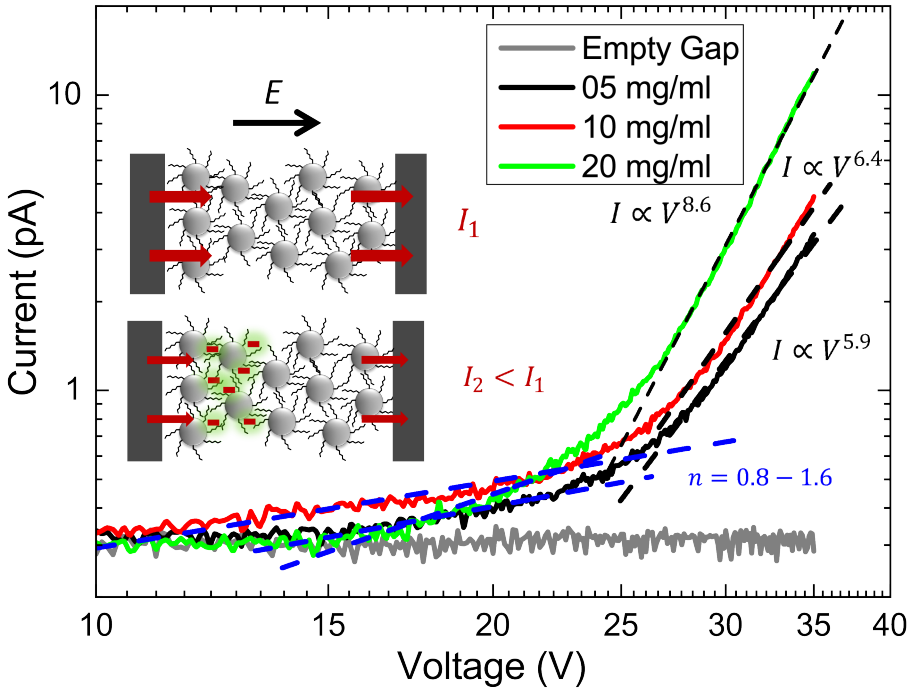

Figure 5.6 *I-V* characteristics of Fig. 5.1(a) in a log-log plot. Dashed lines are linear fits to the curves, with extracted exponents n listed next to the data. Blue and black color refers to the medium and high-bias regime, respectively. Inset: Schematic of trapped charges, limiting transport in a network of Hex-SiNCs: charge carriers are initially injected in the SiNC network which leads to the current I_1 (upper panel). Some of these carriers are trapped and build up a space charge layer(lower panel) which reduces the external electric field. This eventually leads to a lower current I_2. Reprinted (adapted) from [116]. Copyright (2019) IOP Publishing Ltd, CC BY 3.0 license.

Ginger *et al.* observed a similar decreasing behavior of the current (cf. Fig. 5.2 and Fig. 5.3) at a fixed bias voltage in disordered films of tri-n-octylphosphine oxide (TOPO) cadmium-selenide (CdSe) nanocrystals which they explained by SCLC in the presence of deep trap states [131]. They used a stretched exponential fit to their data according to:

$$I(t) = I_0 \exp\left(-\left(\frac{t}{\tau}\right)^{\beta}\right) \tag{5.2}$$

together with a numerical model based on the semiconductor drift-diffusion equations with an additional extension which accounts for energetically deep laying trap states. This way, they could fit their data with Eq. 5.2 and relate the fitting parameters I_0, τ and β to the electronic properties of their CdSe thin films. According to the authors, I_0 is related to the mobility of the charge carriers in the film, τ is a characteristic time scale of the system and the stretching exponent β is related to the trap density.

We used Eq. 5.2 to fit our data in an analog way. The resulting fit matches our data well as it is depicted in Fig. 5.7 exemplary for the decreasing current at $V = 25\,\mathrm{V}$ in Fig. 5.3. From the fit, we extracted $I_0 = 1.22 \times 10^{-10}\,\mathrm{A}$, $\tau = 169.28\,\mathrm{sec}$ and $\beta = 0.41$. In [131], the authors

determined similar values for β in the range of 0.2 to 0.5 which they relate to a corresponding trap density of $n_t \approx 2 \times 10^{16}\,\mathrm{cm}^{-3}$ from comparison with the best solution of their numerical model to the data. Since our obtained β value is in the same range, this trap density can be considered as a first estimation of the trap density in our SiNC film as well.

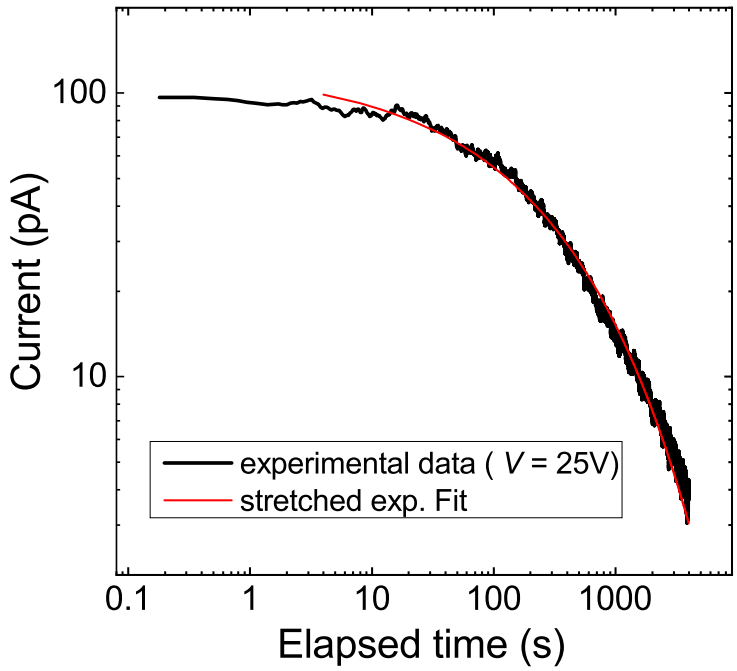

Figure 5.7 Time-dependent current for a fixed voltage of $V = 25\,\mathrm{V}$ for the Hex-SiNC nanogap device with $l = 100\,\mathrm{nm}$, $w = 5\,\mu\mathrm{m}$ and $c = 20\,\mathrm{mg/ml}$ (cf. Fig 5.3).

5.3 Kinetic Monte-Carlo simulation

We conducted numerical simulations to study the charge transport in more detail within the Si nanogap electrode devices which were filled with thin films of Hex-SiNCs. We implemented a kinetic Monte Carlo (kMC) model as it has been done e.g. for SiNCs embedded in a SiO_2 matrix by Lepage *et al.* [132] to study the charge transport within the nanogaps.
The kMC simulations during the course of this work were conducted by Waldemar Kaiser from the Professorship of Simulation of Nanosystems for Energy Conversion at TUM (Prof. Alessio Gagliardi).

Simulation model

A schematic of the simulation box is presented in Fig. 5.8. The simulation box - representing the nanogap - consists of SiNCs separated by a distance of 1.6 nm, which is twice the length of the organic hexyl chains. The highly doped Si electrodes are used as boundary conditions of the nanogap. Periodic boundary conditions are placed along the nanogap, while open boundaries

are used perpendicular to the substrate. Charge carriers can be injected from both electrodes into the SiNCs. The charges move then through the SiNC network by a hopping mechanism and can be collected from both electrodes .

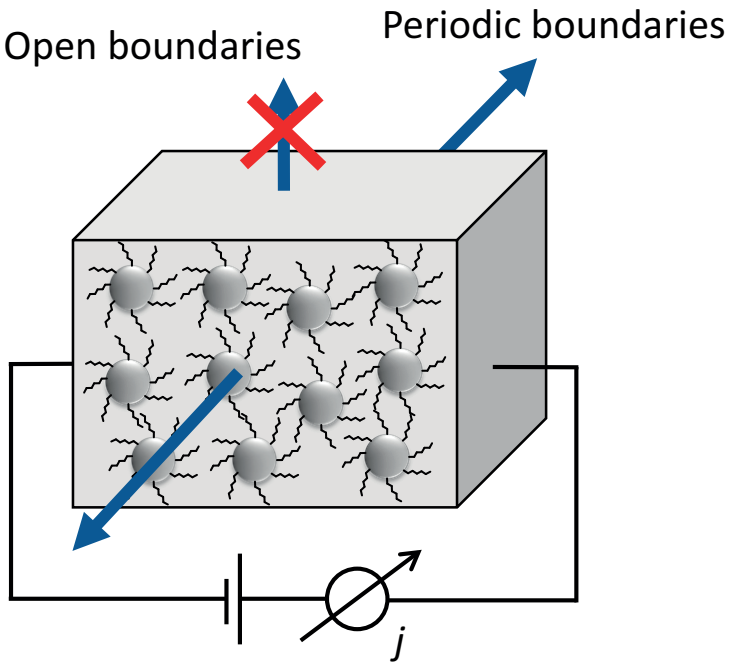

Figure 5.8 Schematic of the simulation box used for the kMC model of Hex-SiNCs filled in the nanogap with boundary conditions. The arrows symbolize the boundary conditions of the simulation box.

Charge transport is described by the Miller-Abrahams (MA) hopping rate which is a valid description of the current as the SiNCs are weakly coupled due to the separation by the hexyl chains. The current density j is then determined by counting charge extraction events at the electrodes for an averaged time period during the kMC simulation. The MA-rate a_{ij}^{hop} describes a thermally activated incoherent transport (cf., eg. 2.7). The energy difference ΔE_{ij} experienced by the charge carriers moving between nanocrystals i and j is given by

$$\Delta E_{ij} = \Delta E_{ij}^{0} + \Delta E_{ij}^{\mathrm{C}} + \Delta E_{ij}^{\mathrm{F}} \,. \tag{5.3}$$

The first term accounts for the difference in the HOMO energies including the quantum confinement

$$\Delta E_{ij}^{0} = E_j - E_i \,. \tag{5.4}$$

The molecular energies depend on the SiNC-radius R, which determines the change in bandgap by [133]

$$\Delta E_g = \frac{3.74}{(2R/\mathrm{nm})^{1.39}}\,\mathrm{eV} \tag{5.5}$$

which splits between a shift in valence and conduction band by $\Delta\mathrm{VB}/\Delta\mathrm{CB} = 2/1$ [134].The second term $\Delta E_{ij}^{\mathrm{C}}$ gives the electrostatic energy difference arising from the self-charging energies of the nanocrystals, polarization effects, and the Coulomb interactions with the other charge carriers in the system:

$$\Delta E_{ij}^{\mathrm{C}} = \Sigma_j - \Sigma_i + q\Delta V_{ij} \,. \tag{5.6}$$

The self-energies are computed using [135]

$$\Sigma(R) = \frac{q^2}{8\pi\epsilon_0 R}\left(\frac{1}{\epsilon_{\mathrm{out}}} - \frac{1}{\epsilon_{\mathrm{in}}}\right) + 0.47\frac{q^2}{4\pi\epsilon_0\epsilon_{\mathrm{in}}R}\left(\frac{\epsilon_{\mathrm{in}} - \epsilon_{\mathrm{out}}}{\epsilon_{\mathrm{in}} + \epsilon_{\mathrm{out}}}\right) . \tag{5.7}$$

In SiNCs (radius R in nm), the static permittivity ϵ_{in} differs strongly from the bulk value of silicon [136]

$$\epsilon_{\mathrm{in}}(R) = 1 + \frac{\epsilon_{\mathrm{Si}} - 1}{1 + \left(\frac{1.38}{2R}\right)^{1.37}} \tag{5.8}$$

where $\epsilon_{\mathrm{Si}} = 11.7$. The difference due to the electrostatic interaction is $\Delta V_{ij} = V_j - V_i$, where V_i is the potential created at the NC i by the charges outside of the NC, the charges in the periodic replicas of the simulation box, and the image charges induced by the contacts. We compute V_i using the Ewald summation [137]. The final term $\Delta E_{ij}^{\mathrm{F}}$ is related to the applied bias voltage V_{bias}

$$\Delta E_{ij}^{\mathrm{F}} = qV_{\mathrm{bias}}\frac{z_j - z_i}{z_{\mathrm{size}}} , \tag{5.9}$$

where z_{size} gives the distance between the electrodes.

The injection of charge carriers is modeled using the thermionic injection model as described by Wolff *et al.* [138]. For each site of both electrodes, we compute the injection rate into the adjacent nanocrystals using the Miller-Abrahams rate (cf. Eq. 2.7 in Section 2.2.3). For each electrode, the injection rates of all contact sites to their respective neighbor nanocrystals is summed up to a common injection rate a_{inj}. Charge collection is treated as the inverse process of injection.

One main property of interest is the impact of the trap density n_t on the current density j. Traps are included on random locations in the simulation box. We assume deep mid-gap traps with an energy of $E_{\mathrm{trap}} = (E_{\mathrm{HOMO}} + E_{\mathrm{LUMO}})/2$. In addition, we add higher quantized states as available states where the charge carriers can hop on. The energy levels of the quantized states are computed using a quantum mechanical spherical potential well.

Simulation results

The diameter of the Hex-SiNCs is determined from TEM inspections as (3.1 ± 0.2) nm (cf. Appendix A.1). A permittivity of $\epsilon_{\mathrm{out}} = 3.79$ is obtained by the Maxwell-Garnett effective medium approximation [139] with the assumption of a closed packing of nanocrystals. The

inverse localization length is chosen as $\gamma = (1.5\,\text{nm})^{-1}$ which means a full delocalization across the SiNC. Simulations are performed using $a_0 = 1 \times 10^9\,\text{s}^{-1}$ and $T = 298\,\text{K}$.

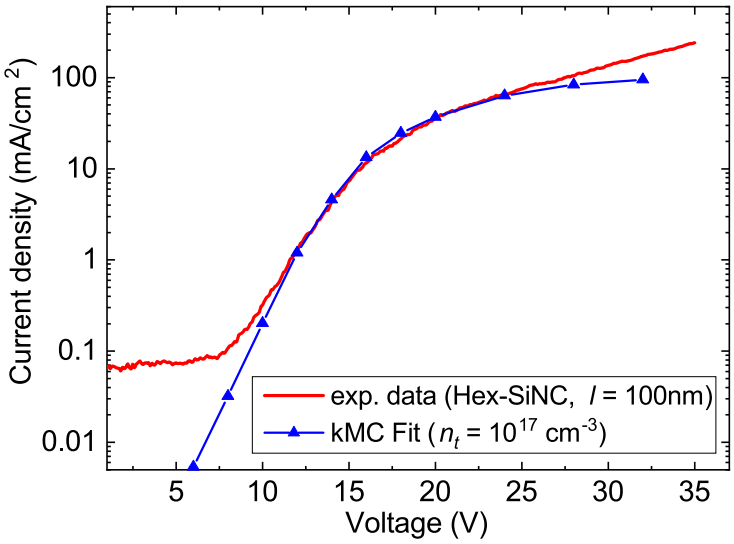

Figure 5.9 Simulated j-V curve (blue) and measurement data (red) of the Si nanogaps filled with Hex-SiNCs and using a trap density of $n_t = 10^{17}\,\text{cm}^{-3}$. The measurement data is taken from the averaged first voltage scans of nanogap devices with $l = 100\,\text{nm}$ and $w = 5\,\mu\text{m}$. Hex-SiNC solution concentration was $c = 20\,\text{mg/ml}$.

The comparison between resulting current density obtained by the kMC simulation and the experimental data as a function of the applied bias voltage is shown in Fig. 5.9. The current signal $\lesssim 5\,\text{V}$ was below the experimental resolution limit. At higher voltages, the simulated curve fits the measurement data well for an implemented trap density of $n_t = 10^{17}\,\text{cm}^{-3}$. The exponential increase of j in the region up to 20 V is controlled by the interplay of the injection of charge carriers and is trap-limited. For higher voltages, we observe indeed a SCLC as discussed in Section 5.2. Regions of high densities of space charges are formed which limits the further increase in current density. Remarkably, the simulated curve deviates from the measurement data for voltages above $\sim 25\,\text{V}$. The simulated j increases less than the measured current density. One possible reason is that only a single occupation of the SiNCs by the charge carriers was permitted in our kMC model. Thus, the extension of our kMC model with an implementation of multiple charge carrier occupations per SiNC while considering the resulting Coulomb repulsion of multiple charges on a single SiNC could potentially lead to a stronger increase of j for high voltages and hence fit the measured data even better in the high voltage regime.

The fitting of our I-V data according to 5.1 indicated SCLC as the dominating charge transport mechanism (cf. Fig. 5.6). The kMC simulation as well as the comparison to the model of Ginger *et al.* suggests also that SCLC is the dominating charge transport mechanism in our SiNC network. Additionally, the trap density $n_t = 10^{17}\,\text{cm}^{-3}$ obtained by the kMC simulations is close to the estimated value of the trap density by comparison to the model of Ginger *et al.*

($2 \times 10^{16}\,\mathrm{cm}^{-3}$). While this can not be considered as complete confirmation of SCLC as the dominating charge transport process, we think that the above discussed arguments are a strong indication that SCLC plays a major role in our SiNCs networks.

5.4 Current voltage spectroscopy on planar SiNC thin films

In comparison to the conducted *I-V* measurements of the functionalized SiNC films filled in the Si nanogap electrodes, we measured planar Si samples (*ABC GmbH*, resistivity: $0.005\,\Omega\,\mathrm{cm}$, doped with Boron), coated with the same SiNCs with a hanging Hg droplet electrode. The samples were coated via the PDMS membrane technique with thin films of Hex-SiNCs, Phen-SiNCs and PA-SiNCs from a solution concentration of $c = 20\,\mathrm{mg/ml}$. This resulted in film thicknesses of $\sim (18 \pm 3)\,\mathrm{nm}$ (Hex-SiNC), $\sim (27 \pm 2)\,\mathrm{nm}$ (PA-SiNC) and $\sim (30 \pm 4)\,\mathrm{nm}$ (Phen-SiNC) determined via cross-sectional SEM inspections. Additionally, two reference samples were measured: one bare Si sample (Ref-NoHF) which was not treated with HF and one Si sample which was treated with HF (Ref-HF) in the same way as the SiNC samples right before the coating process. All samples were measured right after fabrication without delay.

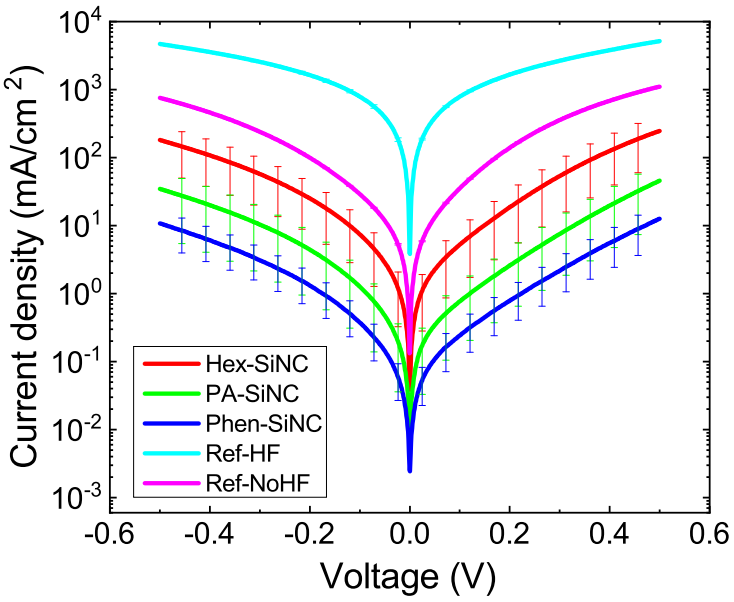

Figure 5.10 Averaged *I-V* curves of planar Si samples, coated with thin films of functionalized SiNCs and measured with a hanging Hg droplet electrode. Error bars are the corresponding standard errors.

We measured for each SiNC type in total 6 spots on 2 samples with at least 3 full voltage cycles on each spot from $-0.5\,\mathrm{V}$ to $0.5\,\mathrm{V}$. The resulting averaged *I-V* curves are depicted in Fig. 5.10. The reference sample which was treated with HF before measurement showed a higher current than the reference sample which was not treated with HF. This is reasonable since a native oxide layer with a thickness of $\sim 2\,\mathrm{nm}$ is expected on the Ref-NoHF sample and a short oxygen plasma was applied additionally before measurement. On the contrary, the HF treatment should remove

the native oxide layer from the Ref-NoHF sample and therefore higher currents can be expected due to the missing insulating barrier on top of the sample. There might be a very thin residual oxide layer present even for the Ref-HF sample, since all samples need to be transported to the measurement glovebox and were thus shortly exposed to air. Additionally, a small residual amount of oxygen is also present in the glovebox.
Due to the different voltage regimes, a quantitative comparison to the data of the nanogap samples is not possible but we observed qualitatively the same trend for the SiNC samples as for the nanogap samples: Hex-SiNC showed the highest currents, but less then the reference samples and PA-SiNC and Phen-SiNC are at the lower range of the measured current regime. As already discussed, we expect the poor film quality which was also present for the planar samples in case of PA-SiNC and Phen-SiNC to be the major reason for the lower observed currents.

5.5 Impedance measurements on planar SiNC thin films

We used the hanging Hg drop electrode and the same planar Si samples coated with thin films of functionalized SiNCs as in Section 5.4 to conduct additionally impedance measurements. We measured samples coated with thin films of Hex-SiNCs, Phen-SiNCs and PA-SiNCs and additional the two reference samples Ref-NoHF which was not treated with HF and one Si sample which was treated with HF (Ref-HF) in the same way as the SiNC samples right before the coating process. All samples were measured right after fabrication without delay. Fig. 5.11(a) shows the obtained Bode plot for $|Z|$ and

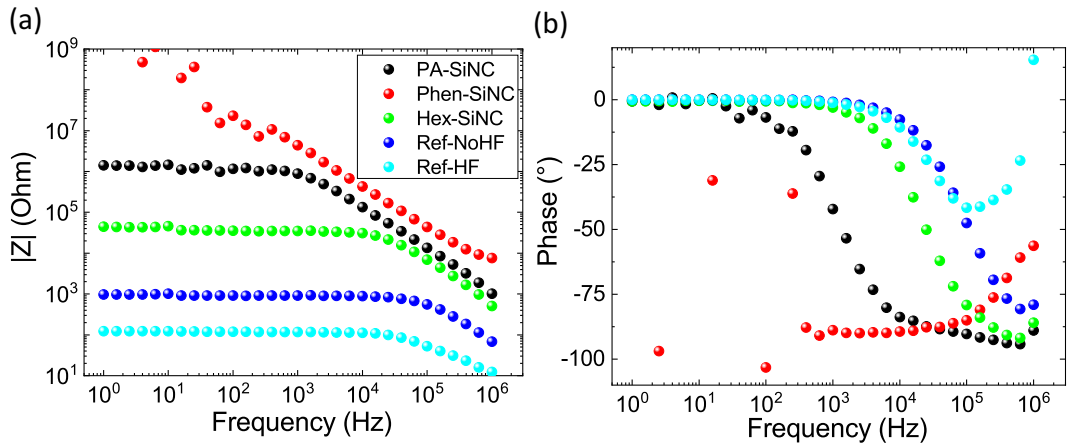

Figure 5.11 Bode representation of the complex impedance showing (a) $|Z|$ and (b) the corresponding phase Θ of the measured planar Si samples coated with thin films of functionalized SiNCs using the hanging Hg drop electrode setup.

Fig. 5.11(b) shows the Bode plot for the corresponding phase Θ for all measured samples. $|Z|$ was lowest for the two reference samples and increased in case of the Hex-SiNC, PA-SiNC and Phen-SiNC samples. Generally, $|Z|$ was constant at frequencies below $\sim$ 1 kHz and decreased

towards higher frequencies. The corresponding phase showed a similar behavior: no phase shift below ~ 1 kHz and a decreasing phase up to ~ −90° for higher frequencies. The PA-SiNC sample deviates from the generally described trend as $|Z|$ is not saturating at low frequencies and the data points of the corresponding phase are distributed over a broad range without clear trend which is attributed to the inhomogeneity in the Phen-SiNC film observed during SEM inspection.

The general observed characteristics in the Bode plots suggests to employ mainly resistors and capacitors in an equivalent circuit model for the modeling of the impedance data.

We used a series resistor together with a parallel RC element as depicted in Fig. 5.12(a) to model both reference samples without SiNC coating. The series resistor R_1 accounts for all setup related resistances as e.g. contact and lead resistances as well as for the resistance of the Si substrate. The RC element (R_{ox} and C_{ox}) represents a "leaky" capacitor which models the response of an oxide layer on top of the Si substrate which allows current transport through the oxide layer. In case of the Ref-NoHF sample, there is certainly a native oxide layer present and also for the Ref-HF sample a thin oxide layer can not be totally excluded, despite all efforts to minimize exposure to air after the HF treatment.

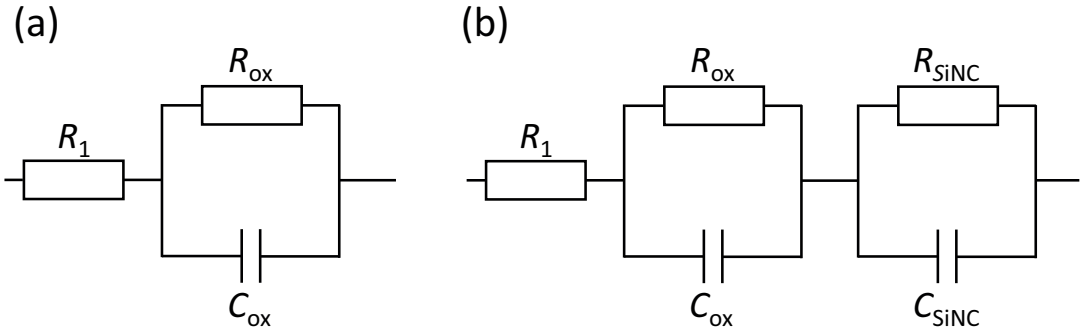

Figure 5.12 Equivalent circuit models employed for the evaluation of the impedance data for: (a) the reference samples without SiNC coating (Si space charge layer is neglected); (b) all SiNC coated samples.

The impedance data of Ref-NoHF is depicted in Fig. 5.13(a) and the impedance data of Ref-HF is shown in Fig. 5.13(b). The straight line represents the obtained fit according to the discussed equivalent circuit model in Fig. 5.12(a). The model matches the impedance data of the reference samples well. The extracted values for R_1, R_{ox} and C_{ox} are given in Tab. 5.1. We can use the obtained (normalized) values for C_{ox} to test the fitting model by calculating the oxide thickness d from the obtained capacitance values via

$$C_{ox} = \varepsilon_0 \varepsilon_{ox} d^{-1} \tag{5.10}$$

with the vacuum permittivity ε_0 and the permittivity of SiO_2 $\varepsilon_{ox} = 3.9$. The resulting thicknesses are $d_{Ref-NoHF} = 2.31$ nm and $d_{Ref-HF} = 0.18$ nm. These values meet the expectation for a Si sample with native oxide layer together with a short oxygen plasma treatment (~ 2 nm) as

well of a HF-treated Si sample which removes the oxide layer. The short exposure to air while transporting the sample to the measurement glovebox after HF treatment accounts for the very thin calculated residual oxide layer.

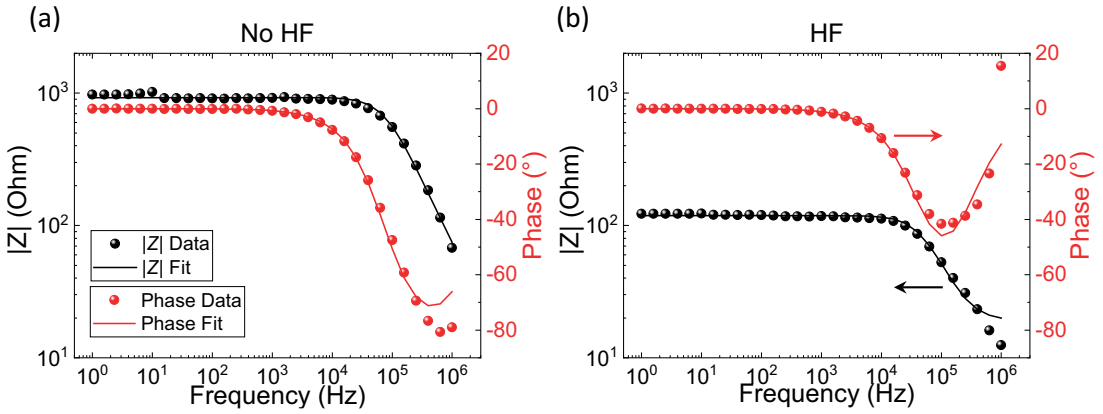

Figure 5.13 Bode plots showing the impedance data of the Si reference samples Ref-NoHF (a) and Ref-HF (b) together with the model fit (straight lines) corresponding to the equivalent circuit model shown in Fig. 5.12(a).

sample	R_1 ($\Omega\,\mathrm{cm}^2$)	R_{ox} ($\Omega\,\mathrm{cm}^2$)	C_{ox} ($\mu\mathrm{F/cm}^2$)	d_{ox} (nm)
Ref-HF	0.04	0.19	18.7	0.18
Ref-NoHF	0.04	1.40	1.50	2.31

Table 5.1 Extracted values from the equivalent circuit fits to the impedance data of the Si reference samples according to Fig. 5.12(a) together with the calculated oxide layer thicknesses d_{ox}.

A similar approach was chosen to fit the impedance data of the SiNC coated samples by an equivalent circuit model. We expanded the applied model for the oxide reference samples with an additional *RC* element as depicted in Fig. 5.12(b). The extracted parameters R_1, R_{ox} and C_{ox} from the model fit of the Ref-HF sample were chosen as fixed input parameters for the model fit of the SiNC coated samples, since we treated all Si samples with HF right before the SiNC coating. Fig. 5.14 shows the impedance data of the SiNC coated samples together with the resulting model fits (straight lines). The obtained fit curves match the impedance data of Hex-SiNC and PA-SiNC well. The Phen-SiNC data was only fitted for frequencies $f \gtrsim 1\,\mathrm{kHz}$ as discussed before. However, the fit matches the phase data of Phen-SiNC poorly for high frequencies. The extracted values R_{SiNC} and C_{SiNC} according to the applied equivalent circuit model are given in Tab. 5.2.

Since the thicknesses of the SiNC thin films were estimated by SEM inspections as $d_{Hex-SiNC} = 17.8\,\mathrm{nm}$, $d_{PA-SiNC} = 26.7\,\mathrm{nm}$ and $d_{Phen-SiNC} = 29.7\,\mathrm{nm}$, it is possible to calculate the relative permittivity ε_r of the SiNC thin films by using the obtained values of C_{SiNC} from the equivalent circuit model and Eq. 5.10. The resulting permittivity values are given in Tab. 5.2. However, it

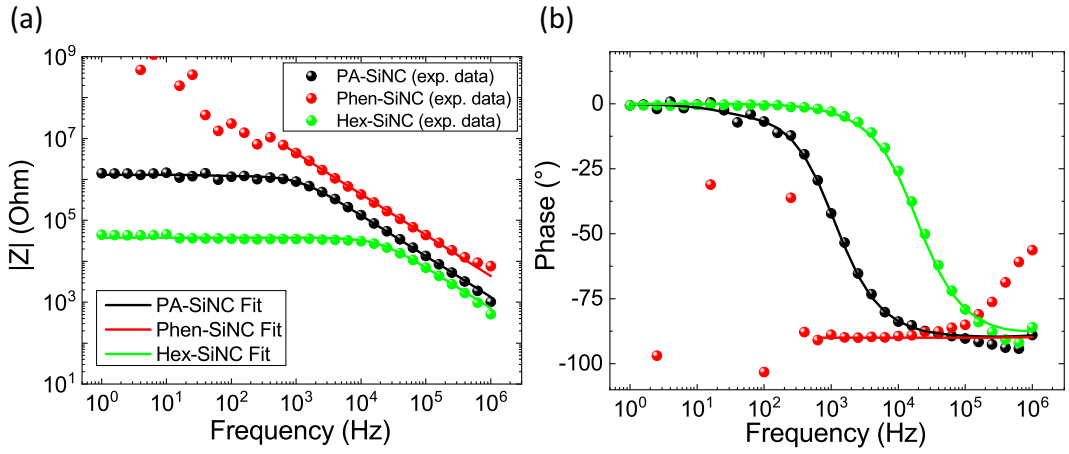

Figure 5.14 Bode plots showing the impedance data of the SiNC coated samples together with the model fit curves (straight lines) corresponding to the equivalent circuit model shown in Fig. 5.12(b).

sample	R_{SiNC} ($\Omega\,\mathrm{cm}^2$)	C_{SiNC} ($\mu\mathrm{F/cm}^2$)	ε_r
Hex-SiNC	37.35	0.22	4.43
PA-SiNC	612.10	0.25	7.41
Phen-SiNC	1.64×10^5	0.08	2.78

Table 5.2 Extracted values from the equivalent circuit fits to the impedance data of the SiNC coated samples according to Fig. 5.12(b).

needs to be noted, that only the Hex-SiNC thin film was truly homogeneous according to SEM characterization. In case of the PA-SiNC and Phen-SiNC thin films, a rough surface and locally varying film thicknesses led only to a rough estimation of the (average) film thicknesses. For the same reason the impedance measurements of these films might be affected because of the worse film quality compared to Hex-SiNC as already discussed in case of Phen-SiNC. Thus, we believe that the obtained relative permittivity values in case of Phen-SiNC and PA-SiNC can be only considered as a rough approximation whereas the calculated permittivity value of Hex-SiNC should be more reliable.

If the calculated $\varepsilon_r = \epsilon_{\mathrm{MG}} = 4.43$ of Hex-SiNC is considered in the context of the Maxwell-Garnett effective medium approximation, the volume fraction ν of the SiNC and hence the thin film density in case of Hex-SiNC can be estimated by [139]:

$$\epsilon_{\mathrm{MG}}(\nu) = \epsilon_{\mathrm{h}} \frac{\epsilon_{\mathrm{i}}(1+2\nu) - \epsilon_{\mathrm{h}}(2\nu-2)}{\epsilon_{\mathrm{h}}(2+\nu) + \epsilon_{\mathrm{i}}(1-\nu)} \tag{5.11}$$

Here, ϵ_{MG} is the relative permittivity of the effective medium, ϵ_{h} the relative permittivity of the host matrix and ϵ_{i} the relative permittivity of the inclusions in the host matrix. If we neglect the influence of the hexyl molecules ($\epsilon_{\mathrm{h}} = 1$) and take the adjusted permittivity for SiNCs with a diameter of 3.1 nm as determined by Eq. 5.8 as $\epsilon_{\mathrm{i}} = 9.05$, we calculate a volume fraction for

the Hex-SiNC thin film of $\nu_{\mathrm{Hex-SiNC}} \approx 0.73$ which is close to a closed packing of the Hex-SiNC ($\nu_{\mathrm{CP}} \approx 0.74$ [140]). The volume fraction should become somewhat smaller if the influence of the hexyl molecules is additional considered, likely down to the range of random closed packing ($\nu_{\mathrm{RCP}} \approx 0.64$ [141]) which would rather match the expectations of our unordered thin film. Nevertheless, since $\nu_{\mathrm{Hex-SiNC}}$ can be considered as an upper estimate of the SiNC volume fraction, the Hex-SiNC thin films can be rather considered as a homogeneous and dense film.

5.6 Thin film composition of SiNC thin films

One important aspect in the electrical analysis of our measured SiNC networks is the composition of the thin films since it directly affects the charge transport properties. We studied the film composition for Hex-SiNC thin films of different thicknesses, using XPS. The XPS measurements during the course of this work were done by Domenikos Chryssikos from the chair of Prof. Stutzmann at WSI, TUM.

In order to obtain insight into the Hex-SiNC film composition, we measured the relative ratios of Si to carbon in the Hex-SiNC thin films on planar surfaces. Planar silicon substrates covered with $\sim$ 100 nm titanium oxide (TiO_x) were used as reference samples for the XPS measurements. They were coated with Hex-SiNC thin films by mechanically pressing via a pressure-transducing PDMS membrane from different solution concentrations, analog to the nanogap separated Si electrode samples (cf. Section 4.3.4).

Fig. 5.15(a)-(d) shows the obtained XPS spectra for C1s, Ti 2p, Si 2p and O 1s, respectively. The black lines correspond to a bare TiO_x substrate which was not in contact with a PDMS membrane, the blue lines to a substrate after applying a PDMS membrane together with pure toluene without Hex-SiNCs, and the red, olive, magenta, and turquoise lines to Hex-SiNC thin films prepared from solutions with a concentration of 5 mg/ml, 10 mg/ml, 15 mg/ml and 20 mg/ml, respectively.

The visible peak doublets in the Ti 2p signal (Fig. 5.15(b)) are assigned to TiO_2 . The peak at lower binding energies in the Si 2p signal (Fig. 5.15(c)) is assigned to elemental Si which originates from the SiNCs since there is no peak visible for the bare TiO_x reference sample. Due to its binding energy of 101.9 eV to 102.5 eV, we associate the second peak at higher binding energies in the Si 2p signal with PDMS (literature value: (102.3 ± 0.5) eV [142]). Similarly, the peak at higher binding energies in the O 1s signal (Fig. 5.15(d)) can be associated with PDMS (literature value: (532.6 ± 0.4) eV), whereas the peak at lower binding energies would belong to TiO_2 (literature value: (530.0 ± 0.2) eV). The C 1s (Fig. 5.15(a)) and Si 2p signals increase with increasing Hex-SiNC solution concentration, while the Ti 2p signal decreases. This confirms qualitatively the increase in Hex-SiNC film thickness with solution concentration. The PDMS peaks in the Si 2p and O 1s signals indicate minor residuals from the membrane-based preparation process. Peak areas do not change with Hex-SiNC solution concentration, suggesting same residual amounts, presumably located at the surface of the

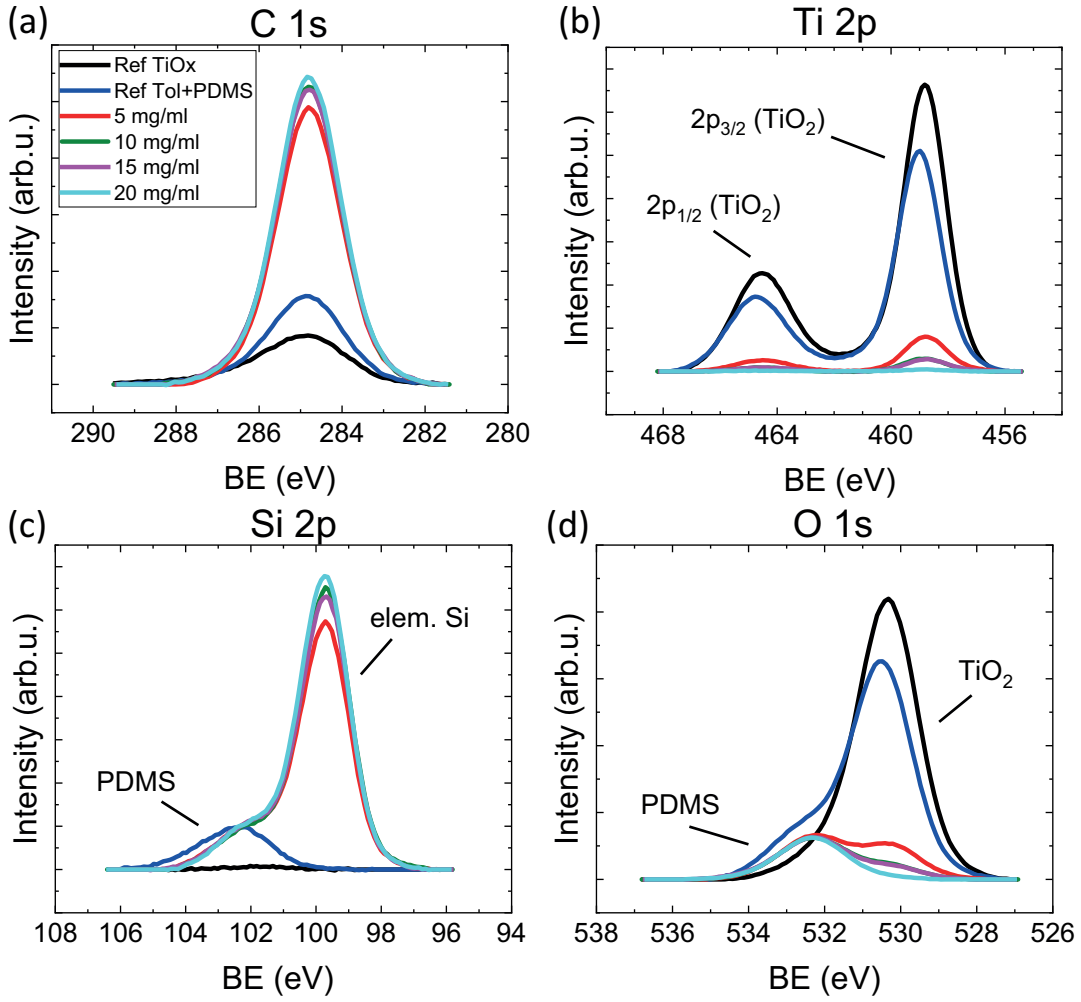

Figure 5.15 XPS spectra for Hex-SiNC reference thin films on TiO_x substrates, fabricated by mechanically pressing via a pressure-transducing PDMS membrane from different solution concentrations analog to the coating of the nanogap separated Si electrode samples. (a) C1s, (b) Ti 2p, (c) Si 2p and (d) O 1s. BE: binding energy.

Hex-SiNC films which would therefore not affect the charge transport properties of the Hex-SiNCs networks. The absence of a pronounced SiO_2 peak in the Si 2p signal at 103.5 eV [142] indicates that the Hex-SiNC are at most very little oxidized, owing to the (protective) surface hexyl functionalization.

For all films prepared from different solution concentrations, the measured Si-to-C ratios were in the range 87 % to 91 % (cf. Tab. 5.3), hence showed very little variation. While a comparison of SiNC density for the different films cannot be derived from these results alone, still the composition of the organically functionalized SiNCs within each film neither did change as function of concentration nor was affected by the filling process, which is essential for comparing films of different thickness in the electrical characterization.

	Ref Tol+PDMS	5 mg/ml	10 mg/ml	15 mg/ml	20 mg/ml
Si/C ratio (±5 %)	0.43 ± 0.02	0.87 ± 0.04	0.90 ± 0.04	0.88 ± 0.04	0.91 ± 0.05

Table 5.3 Relative Si/carbon ratios taken from the normalized XPS peak areas (C 1s, Si 2p, cf. Fig. 5.15(a) and (c)). The ratio is about the same for all investigated Hex-SiNC solution concentrations suggesting that the Hex-SiNC film composition does not change for different film thicknesses.

5.7 Summary

In this chapter, we studied current transport through thin films of functionalized SiNCs. Conductance in the filled Si nanogaps was significantly enhanced compared to untreated devices. The obtained *I-V* characteristics showed the anticipated scaling with channel width, ranging from 5 µm to 50 µm, and with film thickness, ranging from 15 nm to 92 nm in case of the Hex-SiNCs. A strongly hysteretic *I-V* dependence together with a successive decrease of current with time or with the number of *I-V* cycles can be assigned to SCLC-transport, with the functionalized SiNCs providing efficient charge trap centers. Estimated conductivity values for Hex-SiNC thin films are in the range of $1 \times 10^{-9}\,\Omega^{-1}\,\mathrm{cm}^{-1}$ to $1 \times 10^{-8}\,\Omega^{-1}\,\mathrm{cm}^{-1}$. An implemented kinetic Monte Carlo model suggests, that a Miller-Abrahams hopping process of charge carriers between adjacent SiNCs model our *I-V* data well and lead indeed to a SCLC as experimentally observed. Calculated trap densities are accordingly in the range of $n_t = 1 \times 10^{17}\,\mathrm{cm}^{-3}$. An effective medium approximation of the relative permittivity value of $\varepsilon_{Hex-SiNC} = 4.43$ of the Hex-SiNC layer was determined by impedance measurements on planar SiNC coated samples as well as a rather dense packing density of the SiNC thin films. XPS indicated a constant film composition in the case of changed SiNC solution concentrations as well as only minor PDMS residuals present originating from the membrane preparation process, likely at the surface of the coated SiNC films.

6 Electrical characterization of organophosphonate monolayer nanogap devices

6.1 Organophosphonate functionalized nanogaps prepared by anisotropic KOH etching

This Section is partly based on the published conference proceeding: A nanogap electrode platform for organic monolayer-film devices [70] (Simon Pfaehler et al., 2016 IEEE 16th International Conference on Nanotechnology (IEEE-NANO) (Sendai, Japan). IEEE, 2016, 842–844, DOI: 10.1109/NANO.2016.7751507.)[1]

We used the KOH-etched Si gap devices as a test system to study the electrical properties of organophosphonate based SAMs. SAMs of two different organophophonate based molecules were chosen: PAanthrac and PAC16. Generally, there is the expectation that PAanthrac has a higher electrical conductance due to the aromatic constituents in the anthracene backbone and side groups compared to PAC16 that comprise only an alkyl chain and no aromatic groups. SAMs of PAC16 are therefore used as reference system in the electrical characterization of the functionalized Si gap devices.
In the first section, the results of the investigations on the SAM quality by means of water contact angle, ellipsometry and AFM measurements on planar reference samples are presented. Before the electrical characterization of the SAM-functionalized gap electrodes is presented, the structure and properties of the PAanthrac molecule is briefly discussed based on density functional theory simulations of the molecule.

6.1.1 Monolayer characterization

Nanogap samples prepared by KOH etching as well as planar Si samples were functionalized with SAMs of PAC16 and PAanthrac using the T-BAG process described in Section 3.2.6. Since the SAMs grown in the Si gaps were hardly accessible with the common characterization

[1] Reprinted (adapted) with permission from [70]. Copyright (2016) IEEE. Results of the present Section on the characterization of functionalized anisotropically etched silicon nanogaps in KOH were obtained in close collaboration with Kevin Keim as part of his master's thesis [104].

techniques, the planar Si samples acted as reference samples to investigate the quality of the SAMs, e.g., if a smooth and dense monolayer is achieved by the functionalization process without the formation of multilayers. The detailed parameters of the functionalization process can be found in the Appendix D.1.

Figure 6.1 Optical images of water contact angle (θ) measurements of 3 differently surface treated samples. (a) The sample has a SiO_2 surface and was not immersed in THF, hence represents a cleaned and pre-treated reference sample without applying the T-BAG process; (b) Second reference sample which was treated with the complete T-BAG process but without dissolved molecules and (c) PAanthrac functionalized sample via T-BAG. The contact angles were measured at 5 locations per sample respectively and averaged. The given error is the corresponding standard deviation.

We first characterized the SAMs by water contact angle (CA) measurements. A small droplet of DI H_2O is gently placed on top of the SAM surface and the resulting contact angle of the water droplet to the SAM surface is measured. CA measurements were done with a *Contact Angle System OCA* 15+ from *Dataphysics*.

Fig. 6.1 shows the optical images of a water droplet placed on 3 different samples: the sample in (a) has a SiO_2 surface and was not immersed in tetrahydrofuran (THF), hence represents a cleaned and pre-treated reference sample without applying the T-BAG process; the second reference sample in (b) was treated with the complete T-BAG process but without dissolved molecules and the sample in (c) was functionalized with PAanthrac. There was no difference in the contact angle ($(34 \pm 5)°$) between the two reference samples which can be seen as a first indication that there were no THF residuals present on the surface after the T-BAG process. On the other hand, there is a significant difference in the contact angle compared to the PAanthrac functionalized sample ($(76 \pm 3)°$) as evident from Fig. 6.1(c).

Since the droplet consists of water, the contact angle is a measure of how hydrophobic/hydrophilic the sample surfaces are. The reference samples are expected to be mainly terminated by polar OH groups due to the application of oxygen plasma and piranha treatment. Thus, small water contact angles should be measured as it is the case for the reference samples in Fig. 6.1(a)-(b). However even smaller contact angles somewhat $\lesssim 10°$ are expected for an ideally OH-terminated SiO_2 surface. We attribute the slightly higher contact angles of the SiO_2 reference samples to additionally adsorbed molecules from the laboratory environment which possibly contaminated the sample surface in the time between sample preparation and contact angle measurements. From the larger contact angle of $(76 \pm 3)°$ in case of the PAanthrac functionalized sample, we conclude that the PAanthrac SAM surface is more hydrophobic than

the not functionalized reference samples. PAanthrac contains a phosphorus group at the top of the anthracene backbone which is less polar than the OH groups of the SiO_2/Si reference samples which results in the observed increased contact angle. Additionally, the molecules in SAMs are known to self-assemble in a certain tilt angle which increases the probability that parts of the backbone with its carbon/hydrogen regions are exposed to the water droplet [143]. These rather non-polar moieties can additionally contribute to the overall more hydrophobic behaviour of the PAanthrac SAM.

Ellipsometry measurements were used to determine the thickness of the PAanthrac SAM. The measurements were conducted with a *ELX-02C* ellipsometer from *DRE-Dr.Riss Ellipsometerbau GmbH* equipped with a He-Ne laser with 632.8 nm wavelength. The modeling of the ellipsometry data was done with the corresponding software. First, the thickness of the SiO_2 layer was determined with the help of the reference sample immersed in THF. We used the reactive indices and extinction coefficients given in Tab. 6.1 to model the sample based on the obtained ellipsometry data. The reference sample was modeled as a layer stack of Air/ SiO_2/Si while Si was assumed to be opaque. We obtained a SiO_2 thickness of (1.39 ± 0.07) nm based on at least 5 measurements at different spots on the sample. This thickness seems to be reasonable for a native oxide combined with a short oxygen plasma treatment.

The modeled thickness of SiO_2 was then used to model the thickness of the PAanthrac SAM. Thus, in case of the PAanthrac sample we used a layer stack of Air/SAM/ SiO_2/Si to determine the SAM thickness of $h_{ellips} = (1.27 \pm 0.10)$ nm.

material	n	k
SiO_2	1.54	0
PAanthrac SAM [62]	1.50	0

Table 6.1 Refractive indices and extinction coefficients used to model the SAM/ SiO_2 layer during ellipsometry measurements.

We characterized the SAM of PAanthrac additionally by AFM. Fig. 6.2(b)-(d) show tapping mode AFM images of a PAanthrac SAM at different steps during the functionalization process. Fig.6.2(a) shows a tapping mode image of the Si/ SiO_2 reference sample immersed in THF. Besides distinct small particles, visible as white spots with a height > 5 nm which we identified as unintentional contamination particles of the sample surface after sample preparation, possibly originating from the lab environment, there is a relatively smooth surface. The root mean square (RMS) roughness is determined as 0.38 nm based on a 1×1 μm^2 scan area without contamination particles.

Fig. 6.2(b) shows an AFM image of a PAanthrac functionalized sample right after the third T-BAG process but before the last cleaning step. As apparent from the image, there are new larger features visible with lateral dimensions of ~ 500 nm. Height profile scans (not shown) revealed a thickness of 1 nm to 2 nm. Due to the thickness it is likely that these features are additional

layers on top of the SAM. This is supported by Fig. 6.2(c) which shows the same sample after the last multilayer removal step (sonication in ethanol). As it can be seen, the features which are attributed to multilayers are almost completely vanished. The RMS roughness of the three times PAanthrac functionalized sample is determined as 0.31 nm based on a $1 \times 1\,\mu m^2$ scan area. The relatively comparable roughness values of the reference sample and the PAanthrac functionalized samples indicate the formation of a uniform and dense SAM.
Fig. 6.2(d) shows the same PAanthrac functionalized sample after AFM scratching of a $1 \times 1\,\mu m^2$ area to determine the thickness of the SAM. The averaged step height is determined over

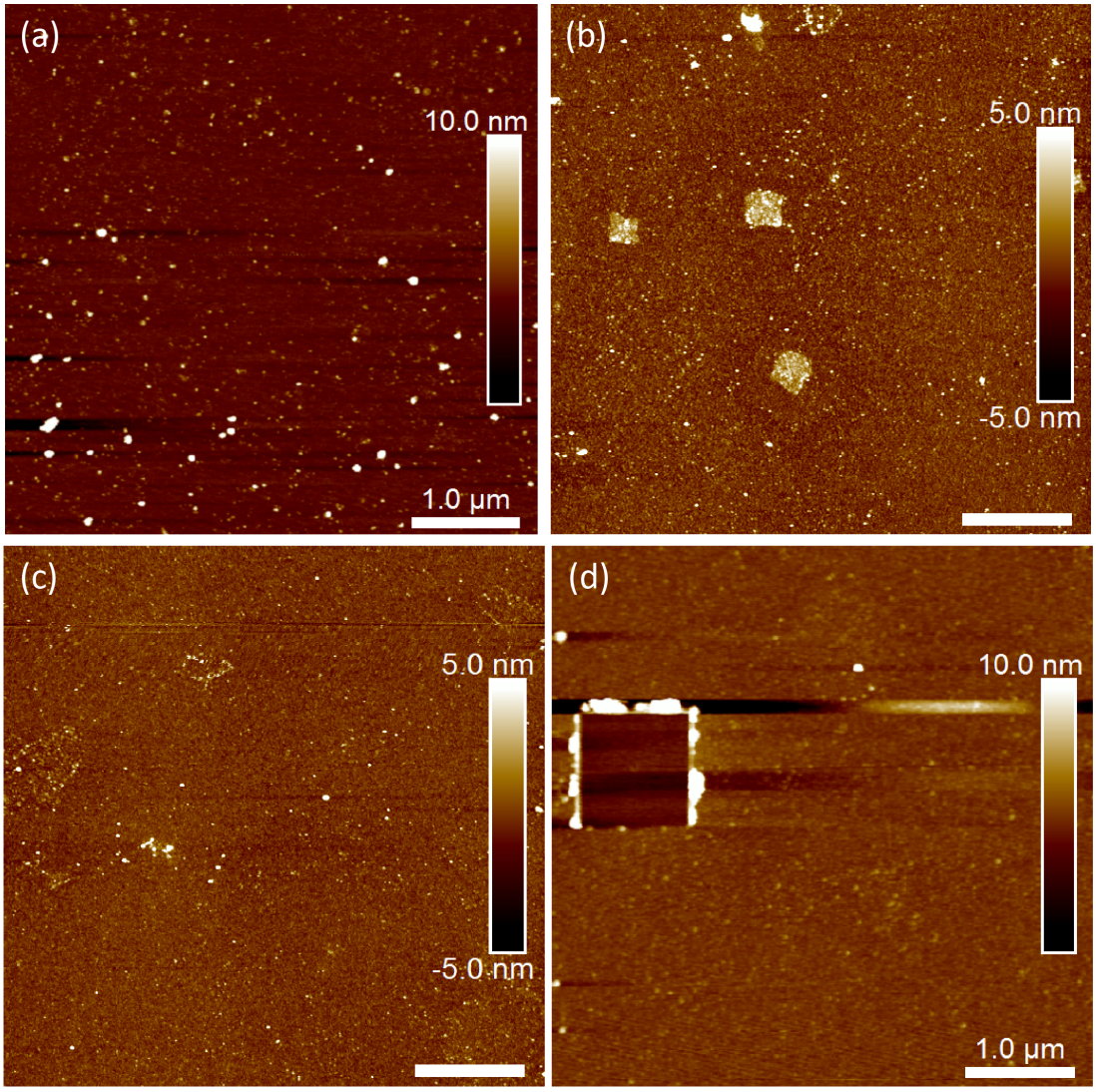

Figure 6.2 AFM images of PAanthrac SAM functionalized samples. (a) Reference sample immersed in THF without PAanthrac molecules. (b) PAanthrac SAM functionalized sample after third T-BAG process. (c) Same sample as in (b) after additional ethanol/sonication cleaning step. (d) PAanthrac SAM functionalized sample after AFM scratching of a $1 \times 1\,\mu m^2$ area. All scale bars a 1 µm.

a sketched area as indicated in Fig. 6.3(a) and the corresponding averaged height profile is depicted in Fig. 6.3(b). From the height profile, a PAanthrac SAM thickness of

$$h_{AFM} = (1.12 \pm 0.22)\,\text{nm}$$

is determined which, is in agreement with the SAM thickness obtained from ellipsometry measurements and slightly below the calculated theoretical length of the PAanthrac molecule (cf. Section 6.1.2), as expected.
Since the ellipsometry model relies on the refractive index of the SAM which was only estimated and not known exactly to determine the PAanthrac SAM thickness, we consider the thickness of the PAanthrac SAM obtained by AFM nanolithography scratching to be more reliable.

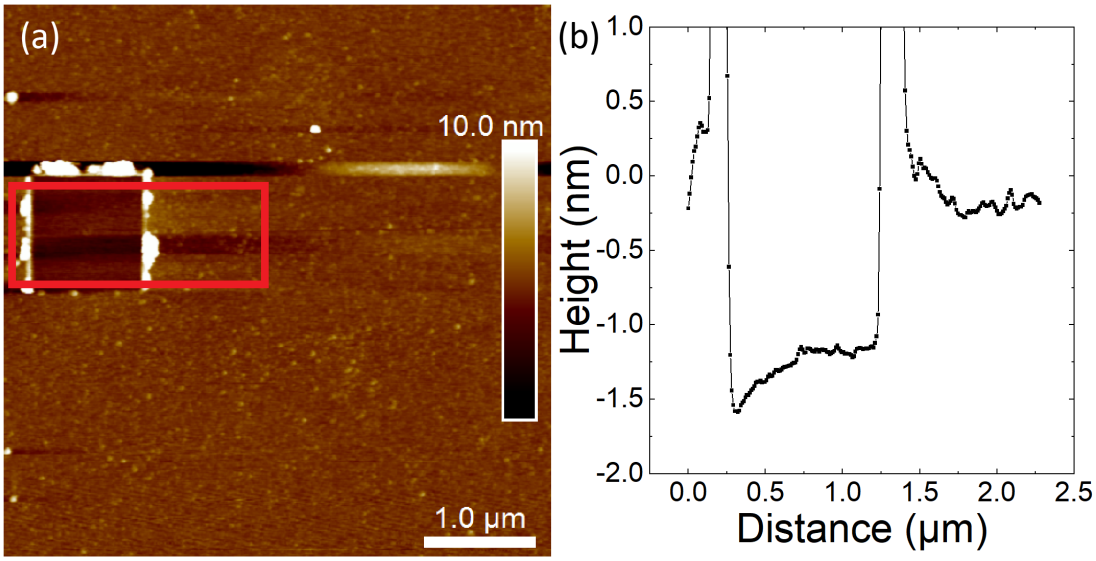

Figure 6.3 (a) Same AFM image as in Fig. 6.2(d) with indicated area for SAM thickness determination. (b) Averaged height profile of area indicated in (a).

6.1.2 Density functional theory simulation

To study the structural and electrical properties of the PAanthrac molecule more in detail, ab-initio quantum calculations were conducted based on density functional theory (DFT). We used the software *Gaussian 09* (*Gaussian Inc.*). The exchange energy functional was described by the Kohn-Sham orbitals and the exchange correlation functional B3LYP and the Gaussian basis set $6-311++g(d)$ were used [144–146]. The scope of the calculations was to optimize the geometry of an isolated PAanthrac molecule in gas phase. The simulation was conducted with the support of Dr. Achyut Bora from the professorship of molecular electronics at TUM. The basic principle of the ab-initio quantum calculations is to minimize the total energy of the PAanthrac molecule by iteratively changing the relative positions of the molecules' atomic nuclei and electron densities. The resulting simulated molecular structure of PAanthrac is depicted

in Fig. 6.4. Carbon atoms are represented in grey, hydrogen atoms in white, phosphorus atoms in orange and oxygen atoms in red. The anthracene backbone is terminated by the two phosphonate groups, one at the top and one at the bottom of the molecule as already expected from the Lewis structure of the molecule. Interestingly, the two anthracene side groups are parallel aligned in the same plane which is tilted by 90° to the anthracene backbone. The length of the molecule, considered as the distance between the most distant atomic nuclei of the top and bottom phosphonate group respectively, is determined as $l_{DFT} = 1.29\,\text{nm}$.

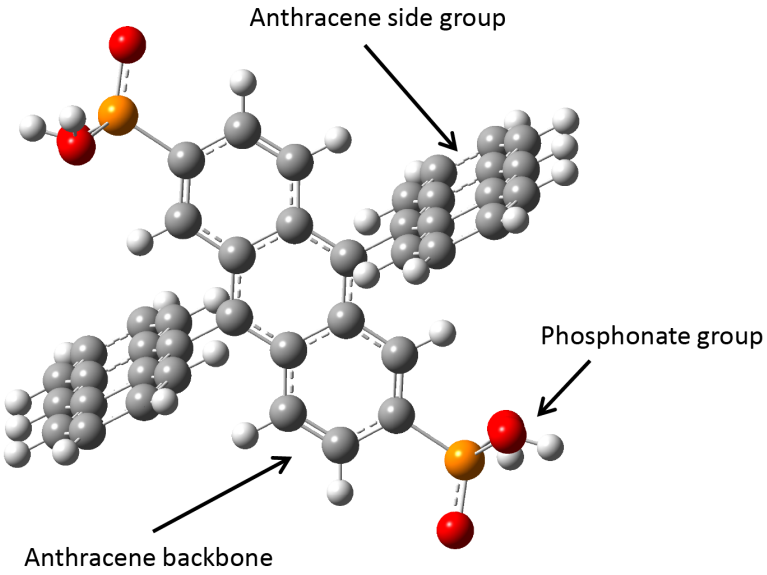

Figure 6.4 Molecular structure of PAanthrac in gas phase calculated by ab-initio quantum calculations based on DFT (*Gaussian* 09 software). Carbon atoms are represented in grey, hydrogen atoms in white, phosphor atoms in orange and oxygen atoms in red. PAanthrac consists of an anthracene backbone terminated by phosphonate groups on each side and two anthracene side groups.

With the length of the PAanthrac molecule determined by ab-initio calculations it is possible to estimate the tilting angle α with respect to the surface normal of the molecules in a SAM by taking the SAM thickness $h_{AFM} = (1.12 \pm 0.22)\,\text{nm}$ into account which was determined by AFM scratching (cf. Section 6.1.1):

$$\alpha = \arccos\left(\frac{h_{AFM}}{l_{DFT}}\right) \approx 29° \tag{6.1}$$

In this context, it is necessary to point out that the simulation of the molecular structure was conducted for an isolated PAanthrac molecule in the gas phase. The length of a surface bond PAanthrac molecule as part of a SAM might therefore be slightly different, but we consider our obtained results as a good starting point and as a first approximation of the molecule length. To our knowledge there are no reports about the tilting angle of molecules in SAMs of PAanthrac. Cattani-Scholz et al. measured the monolayers of similar organophosphonate molecules and found greater tilting angles of about 45° for a 2, 6-diphosphono-anthracene molecule without any

sidegroups [62]. The existence of the anthracene sidegroups in PAanthrac could possibly explain the smaller calculated tilting angle. Due to the sidegroups, PAanthrac requires laterally more space which prevents the PAanthrac molecules from stronger tilting during SAM formation.

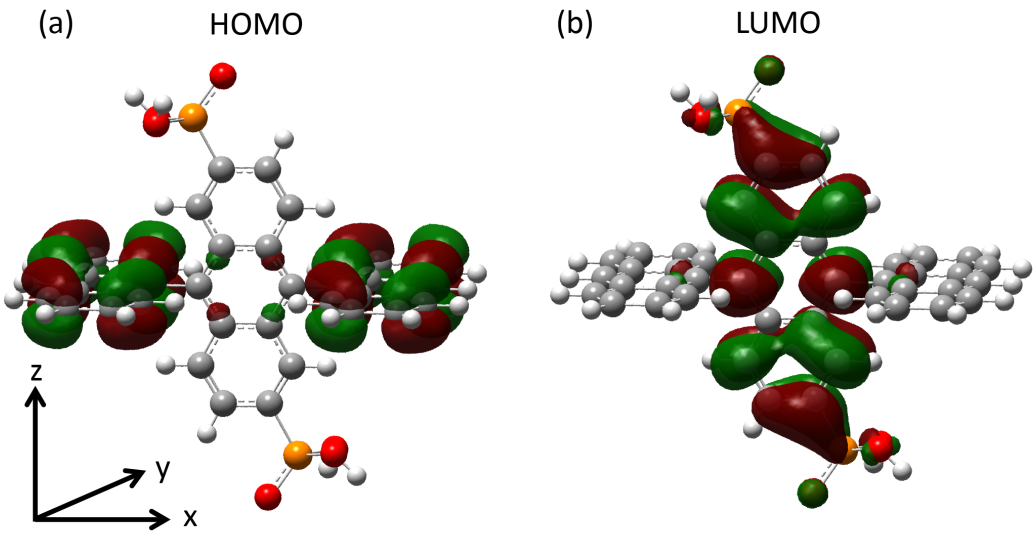

Figure 6.5 Spatial distribution of molecular orbital isosurfaces of (a) highest occupied molecular orbital (HOMO), and (b) lowest unoccupied molecular orbital (LUMO) of PAanthrac, calculated by ab-initio quantum calculations (*Gaussian 09* software). Red represents a positive and green a negative corresponding wave function sign.

Besides the structural conformation of PAanthrac, the simulation provides additional information about the distribution and energies of the molecular orbitals. Fig. 6.5(a) shows the spatial distribution of isosurfaces of the highest occupied molecular orbital (HOMO), and Fig. 6.5(b) of the lowest unoccupied molecular orbital (LUMO) of PAanthrac. In this figure, red represent areas with a positive and green areas with a negative corresponding wave function sign. The HOMO is mainly located along the anthracene side groups and it extends only to a small amount to the middle part of the anthracene backbone. At the phosphonate groups and outer ends of the anthracene backbone, no HOMO is visible. On the contrary, the LUMO extends mainly to the anthracene backbone and there is almost no LUMO distribution at the anthracene side groups as visible in Fig. 6.5(b).

The spatial distribution of the HOMO and LUMO can lead to first assumptions about the charge transport behavior on the molecular scale. The concentration of the HOMO to the tilted anthracene side groups might point to efficient lateral charge transport through a SAM of PAanthrac molecules if π-stacking of the anthracene side groups is considered. However, such overlapping $\pi - \pi$ orbitals would lead to a splitting of the HOMO and LUMO levels and hence change the calculated energy levels [90, 91].

The energy levels of the HOMO and LUMO are obtained from the ab-initio calculations. They are determined as:

$$E_{HOMO} = -5.70\,\text{eV}$$
$$E_{LUMO} = -2.65\,\text{eV}$$

with respect to the vacuum level. The corresponding HOMO-LUMO energy gap is then calculated as $E_{HOMO-LUMO} = 3.05\,\text{eV}$.

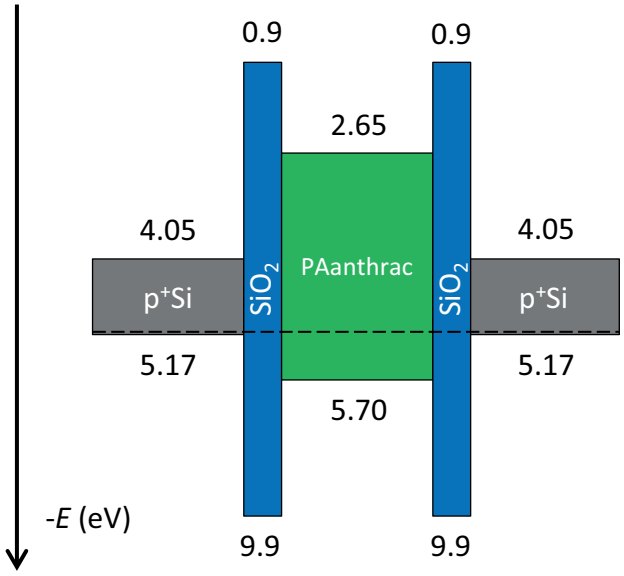

Figure 6.6 Proposed energy diagram of a functionalized nanogap electrode device with PAanthrac in equilibrium without applied voltage and with respect to the vacuum level. Energy values for Si and SiO_2 are taken from [147], HOMO/LUMO energy values are taken from the ab-initio quantum calculations of PAanthrac. Charging, interface states and band bending in Si is neglected.

We used the obtained energy levels E_{HOMO} and E_{LUMO} of the PAanthrac molecule to consider the general energy level alignment of a functionalized nanogap device. Fig. 6.6 shows the proposed energy diagram for a Si nanogap device functionalized with a SAM of PAanthrac with respect to the vacuum level. Si has an electron affinity of $\chi_{Si} = 4.05\,\text{eV}$ and a band gap of $E_{gap,Si} = 1.12\,\text{eV}$ which determines the conduction band edge E_C and the valence band edge E_V energies [147]. Due to the oxygen plasma and Piranha treatment there is a thin SiO_2 layer (1.39 nm) on top of both Si electrodes as measured by ellipsometry (cf. Section 6.1.1). The electron affinity of SiO_2 is $\chi_{SiO_2} = 0.9\,\text{eV}$ and its band gap is $E_{gap,SiO_2} = 9\,\text{eV}$ [147]. The Fermi energy E_F of degenerately p-doped semiconductors can be estimated by [147]

$$E_V - E_F \approx kT\left[\ln\left(\frac{p}{N_V}\right) + 2^{-3/2}\frac{p}{N_V}\right] = -24.8\,\text{meV} \tag{6.2}$$

Here, k is the Boltzmann constant and T is the temperature (room temperature). $N_V = 2.65 \times 10^{19}\,\mathrm{cm}^{-3}$ is the effective density of states in Si and $p = 9 \times 10^{18}\,\mathrm{cm}^{-3}$ is the doping density of the Si top layer.
The Fermi energy level is right above E_V of Si and lies in the HOMO-LUMO gap of PAanthrac. Due to the large band gap of SiO_2, charge carriers need to overcome a high energy barrier if injected from the Si electrodes into the molecules of the SAM. It is rather likely that charge carriers tunnel through the SiO_2 barrier due to the very small thickness of the SiO_2 layer. The energy barrier offset between the HOMO level and E_F is $\phi_{HOMO} \approx 0.57\,\mathrm{eV}$ and between E_F and the LUMO level $\phi_{LUMO} \approx 2.48\,\mathrm{eV}$. It is therefore rather likely that charge transport is mainly conducted via the HOMO level driven by holes. However, it needs to be noted that the HOMO/LUMO levels are based on a simulation of the isolated PAanthrac molecule in gas phase. The energy levels change for molecules in a SAM due to splitting and broadening effects of the HOMO/LUMO levels [90, 92]. Additionally the influence of the coupling of the molecules to the Si/ SiO_2 electrodes is neglected as well as possible interface states at the Si/ SiO_2-molecule interface, but we consider the given energy diagram as a good first approximation of the energy levels in our nanogap devices.

6.1.3 Current-voltage characterization of functionalized nanogaps

We characterized the Si nanogap electrode devices functionalized with organophosphosphonate SAMs electrically by measuring their *I-V* characteristics in a 2-terminal configuration by contacting the metal pads of a single Si nanogap device with the probes of a vacuum probestation ($p \approx 5 \times 10^{-6}\,\mathrm{mbar}$) at room temperature in darkness. Gate-dependent measurements via the Si substrate as global back gate suffered from substantial leakage currents from the substrate to the source contact (electrical reference point), most likely because of the very thin SiO_2 layer (8 nm). That is why all *I-V* measurements were conducted in a floating gate configuration.
One sample chip comprised 150 electrode pairs. Four out of 9 nanogap sample chips contained completely etched nanogap electrode devices. According to SEM inspection, 28 gap devices in total were completely etched down to the buried oxide with gap electrode distances in the order of $l = 200\,\mathrm{nm}$ - 1 µm and 8 of them were electrically insulating and therefore taken into further consideration for the evaluation of the *I-V* characteristics of PAanthrac SAMs.
All nanogap samples were first electrically pre-characterized by measuring the *I-V* characteristics of all empty nanogap electrode devices right after their fabrication. Only those showing complete electrical insulating behavior for an applied voltage in the range of −1 V to 1 V, i. e., no visible increase in current and a resistance in the TΩ regime, were taken into account for the electrical characterization after SAM functionalization. After these reference measurements of the as-fabricated empty nanogap devices, all nanogap samples were functionalized with SAMs of PAanthrac and subsequently electrically characterized by *I-V* spectroscopy. In a last step, we removed the PAanthrac SAM by applying an oxygen plasma (200 W, 2 min, 1.4 mbar) and functionalized all samples again with an aliphatic SAM of PAC16 molecules and measured

their *I*-*V* characteristic as a second reference. SAMs of PAC16 are expected to be electrically less conductive because of the absence of any π-conjugated groups.

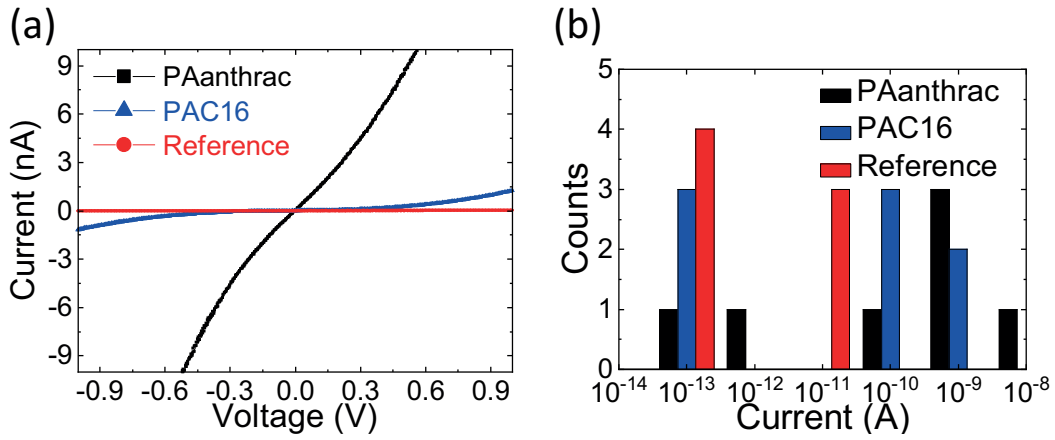

Figure 6.7 (a) *I*-*V* curves of a single nanogap device showing the bare reference measurement after gap fabrication as well as the measurements after functionalization with a PAanthrac SAM and a PAC16 respectively. (b) Histogram of the order of magnitude of the measured absolute currents at an applied voltage of $V = 0.5$ V for all studied nanogap devices and functionalization cases.

Fig. 6.7(a) shows exemplarily the *I*-*V* characteristics of one single silicon nanogap device with applied voltages in the range of -1 V to 1 V. The red curve represents the *I*-*V* curve of the empty, as-fabricated nanogap device which shows no increase in current while scanning the voltage from -1 V to 1 V. The black *I*-*V* curve represents the same device after PAanthrac functionalization. There is a clear increase in conductance and a non-linear *I*-*V* curve visible. The blue curve represents the *I*-*V* curve of the same device under consideration after SAM removal and the second functionalization step with PAC16. The conductance decreased compared to the PAanthrac case, but is slightly higher compared to the as-fabricated empty nanogap device. We measured all *I*-*V* characteristics for all nanogap devices in all SAM/reference cases. Fig. 6.7(b) shows a histogram showing the order of magnitude of the measured absolute currents at an applied voltage of $V = 0.5$ V for all studied nanogap devices and functionalization cases. Nanogap devices showed an increase in current after PAanthrac SAM deposition which varied over 5 orders of magnitude. We attribute this range over the 8 devices studied to measured differences in channel lengths l, and to possible variation in SAM local order and coupling to the electrodes.

The increased current of the PAanthrac functionalized devices becomes more evident by evaluating the *I*-*V* curves averaged over all measured nanogap devices as depicted in Fig. 6.8, which shows the averaged *I*-*V* curves for an applied bias between 0 V to 0.6 V which was taken at both positive and negative voltages. The standard error of the average data points is included as error bars. We find significantly higher conductance of the PAanthrac devices with respect to both reference systems (bare, and with PAC16 SAM). Since the less conductive PAC16 functionalized nanogap devices were measured after the PAanthrac functionalization, we conclude

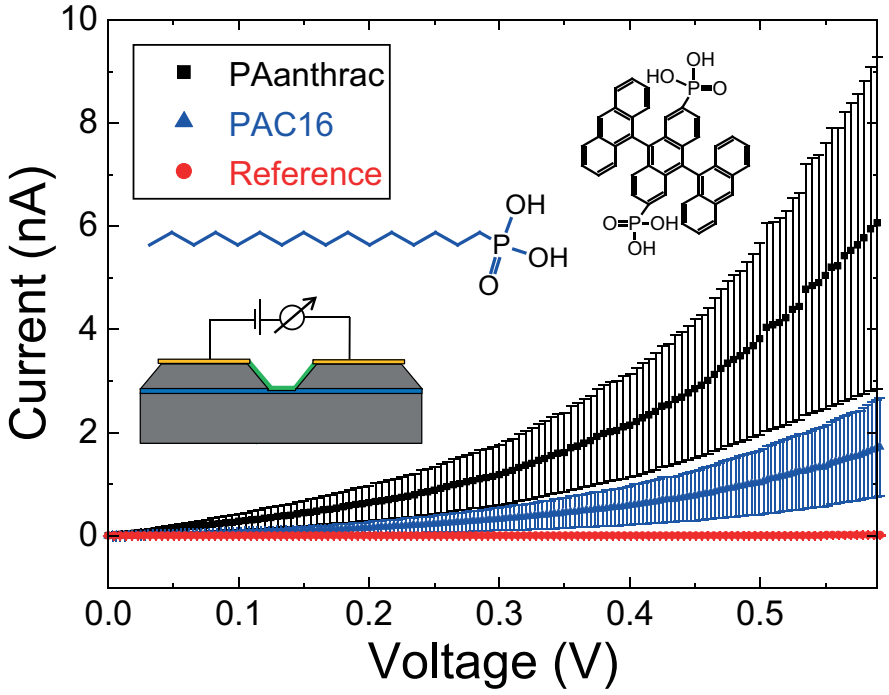

Figure 6.8 Averaged current as function of source-drain bias, for all eight measured nanogap electrode devices of different gap length l, ranging from 200 nm to 1 µm. The standard error of the average data points is included as error bars. The data show an enhanced conductance for the devices functionalized with PAanthrac SAM compared to those with PAC16 SAM and to the bare, unfunctionalized nanogap electrode devices. The average was taken over both positive and negative voltages. Inserts: Schematic of two terminal *I*-*V* measurement configuration, molecular structures of PAanthrac (black) and PAC16 (blue). Reprinted (adapted) with permission from [70]. Copyright (2016) IEEE.

that the increase in conductance originates from an enhanced charge transport because of the PAanthrac functionalization. Electrical effects originating from the functionalization process itself (e.g. treatments with organic solvents etc) can be therefore excluded. We attribute the higher average lateral conductance of the PAanthrac SAM to the aromatic substituents of the PAanthrac molecules, in particular to the possible overlap of anthracene side groups of adjacent molecules (π-stacking) as discussed in Section 6.1.2. A sketch of such overlapping anthracene side groups is depicted in Fig. 6.9.

6.1.4 Summary

In this section, we studied the electrical characteristics of silicon nanogap electrodes functionalized with a SAM of PAanthrac. The SAM quality was investigated by analyzing the SAM surface morphology. We found that our self-assembly functionalization protocol gave rise to the formation of a uniform and dense SAM as has been characterized by water CA, ellipsometry and AFM measurements. DFT simulations revealed the molecular structure of PAanthrac with its 90° tilted anthracene side groups as well as the energy levels of the corresponding HOMO and LUMO. *I*-*V* spectroscopy showed a significantly increased conductance of the Si nanogap

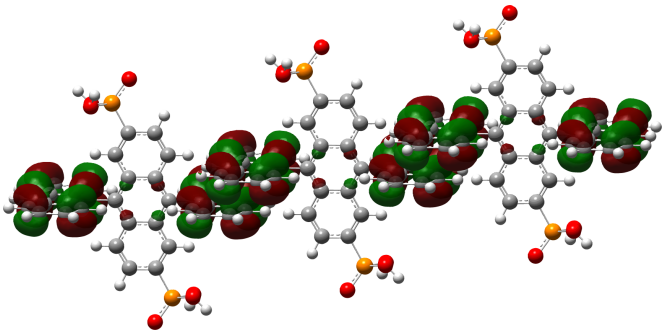

Figure 6.9 Sketch of possible molecular confirmation of PAanthrac molecules in a SAM (composed of molecules which are obtained by single molecule DFT calculations, cf. Fig. 6.5(a)), exhibiting π-stacking of their anthracene side groups which might lead to enhanced lateral conductance.

electrodes functionalized with a SAM of PAanthrac compared to the bare reference nanogap and a PAC16 SAM functionalized nanogap. We attribute this increase in lateral conductance of the PAanthrac SAM to the aromatic substituents of the PAanthrac molecules, in particular to the possible overlap of anthracene side groups of adjacent molecules (π-stacking).

6.2 Organic monolayer field effect transistor

The following Section is based on the published conference proceeding: Silicon Nanogap Electrode Engineering for Organic Monolayer Field Effect Transistors [117] (Simon Pfaehler et al., 2019 IEEE 19th International Conference on Nanotechnology (IEEE-NANO) (Macao, China). IEEE, 2019, 521–525, DOI: 10.1109/NANO46743.2019.8993870.)[2]

We used the Si nanogap electrode devices prepared by EBL and RIE (cf. Section 4.2) as test system to study the electrical properties of SAMs of the organophophonate based molecule PAphenyl in a field effect transistor (three terminal) configuration.
In the first section, finite element simulations of the electrostatics of the nanogap electrode devices are studied while the Si handle layer of the SOI sample is used as a global back gate. The following sections cover the investigation of the SAM quality on planar reference samples by means of water CA and AFM measurements and the electrical characterization of the SAM functionalized nanogap electrodes.

6.2.1 Electrostatic simulation of three terminal nanogap device

We investigated the electrostatic characteristics of the Si nanogap electrodes fabricated by EBL and RIE by finite element simulations. The SOI material which was used as the basis wafer material for the fabrication of the nanogap devices, has the benefit of a 200 nm thick buried SiO_2 layer which enabled the use of the bottom Si handle layer as a global back gate for the nanogap

[2]Reprinted (adapted) with permission from [117]. Copyright (2019) IEEE.

electrode devices. We used the software *Comsol multiphysics* 5.4 with the electrostatics module for the simulation of the electrostatic potential distribution in the nanogap channel with applied gate voltages. A single empty nanogap electrode device was modeled in air with channel length $l = 200\,\text{nm}$ and reduced width ($w = 1\,\mu\text{m}$) to minimize the calculation time. This change compared to the real device is practically not supposed to influence the obtained results, since we mainly focused our evaluation in the middle of the nanogap, far away from the edges. We used the relative permittivity values shown in Tab. 6.2 from the internal material database of Comsol. The source electrode acted as reference potential and was grounded. We neglected

material	ε_r
SiO_2	4.2
Si	11.7

Table 6.2 Relative permittivity values used in finite element simulations.

the electrostatics in the electrodes themselves, that means that the sidewalls of the nanogap were chosen to define the boundary condition for the applied source-drain voltage as well as the bottom plane of the SiO_2 layer for the applied gate potential. For a real device there is certainly a small voltage drop from the metal contact pads to the Si electrodes, but we consider this as negligible because of the degenerate doping of the Si top layer.
Fig. 6.10 shows exemplarily the 3D image of the resulting potential distribution in the simulated nanogap for an applied $V_{DS} = 1.3\,\text{V}$ and $V_{GS} = -5\,\text{V}$.

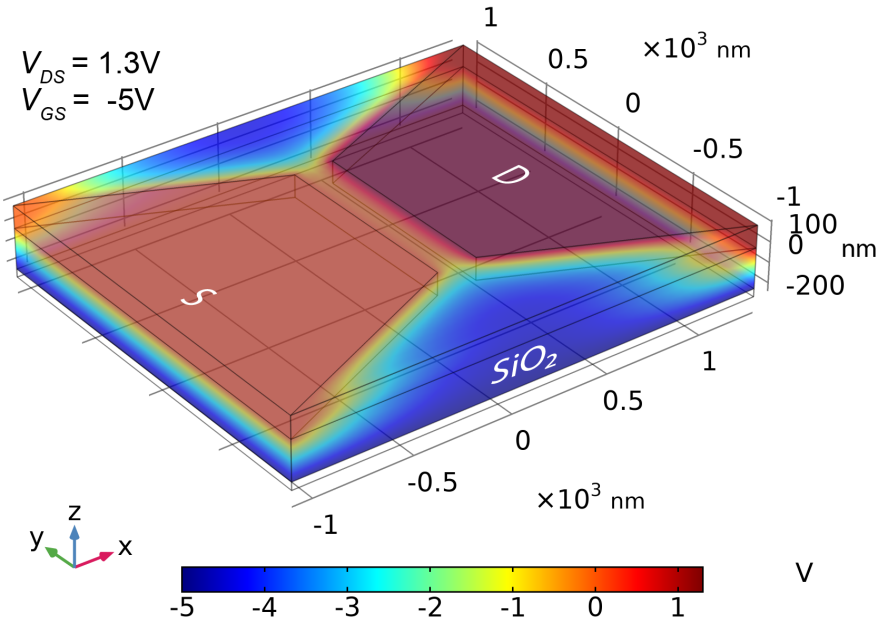

Figure 6.10 Spatial electrostatic potential distribution of the simulated nanogap for $V_{DS} = 1.3\,\text{V}$ and $V_{GS} = -5\,\text{V}$.

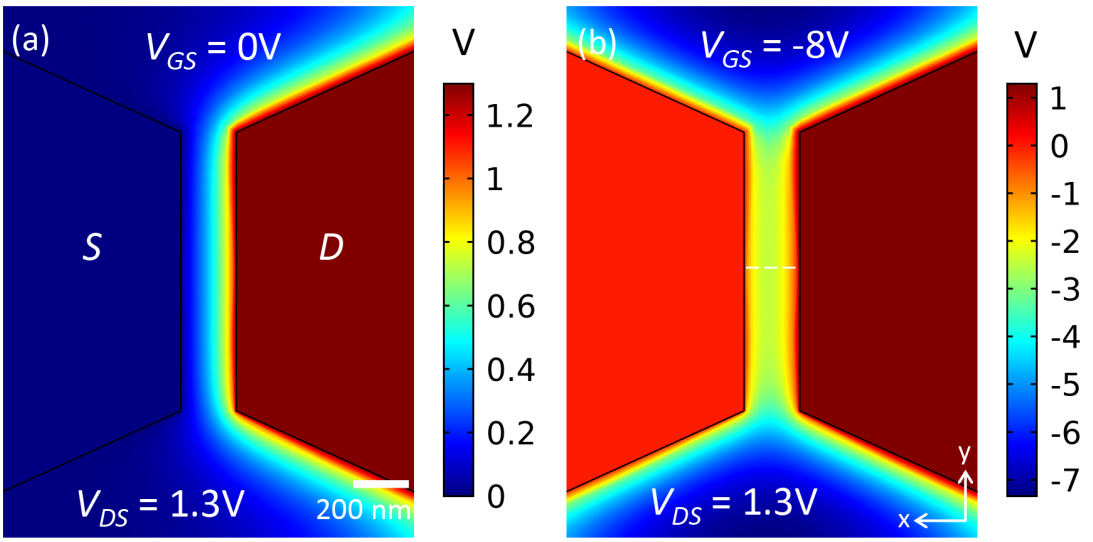

Figure 6.11 Spatial electrostatic potential distribution at the bottom of the nanogap ($z = 0$) directly at the SiO_2 interface for $V_{DS} = 1.3$ V and (a) $V_{GS} = 0$ V and (b) $V_{GS} = -8$ V.

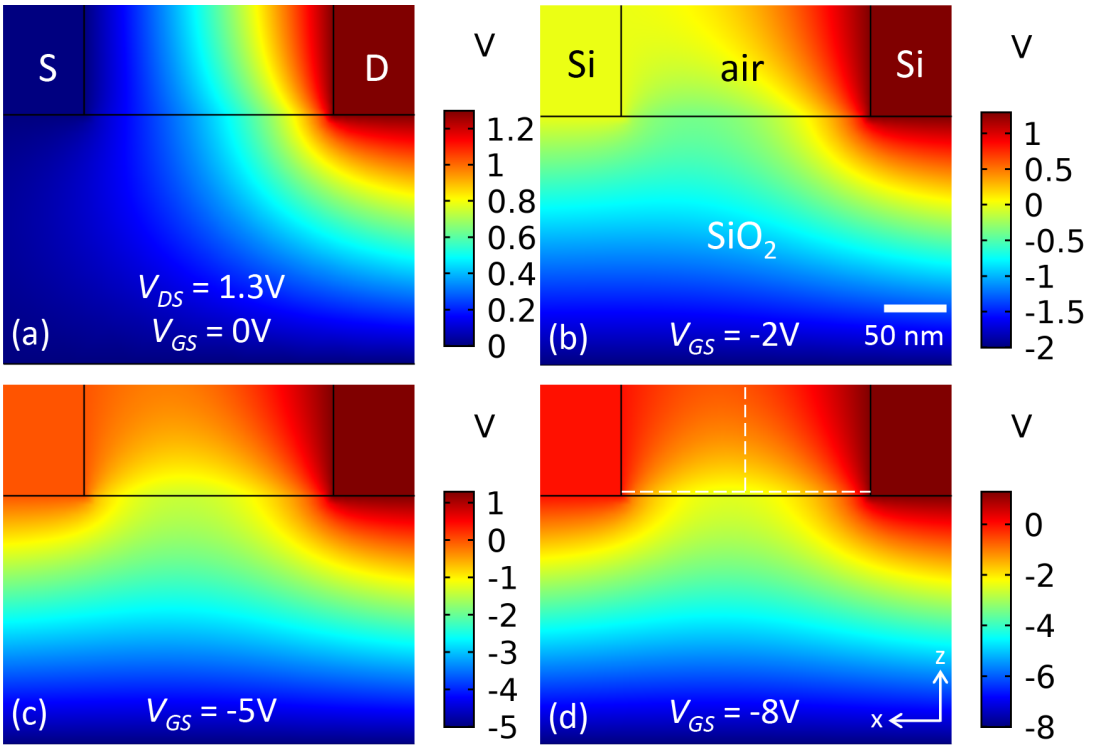

Figure 6.12 Evolution of the spatial electrostatic potential distribution in a cross sectional xz plane in the middle of the nanogap ($y = 0$) for $V_{DS} = 1.3$ V as indicated by the white dashed line in Fig. 6.11(b). (a) $V_{GS} = 0$ V, (b) $V_{GS} = -2$ V, (c) $V_{GS} = -5$ V, (d) $V_{GS} = -8$ V. Reprinted (adapted) with permission from [117]. Copyright (2019) IEEE.

Since the nanogap is afterwards functionalized with a SAM, the potential distribution in the gap at the SiO_2 interface is of interest which is depicted in Fig. 6.11 and shows the 2D plane at the bottom of the nanogap directly at the SiO_2 surface ($z = 0$, cf. Fig. 6.10 for the definition of the coordinate system). In Fig. 6.11(a) the potential is shown for $V_{GS} = 0\,\text{V}$ and in Fig. 6.11(b) for $V_{GS} = -8\,\text{V}$ while applying $V_{DS} = 1.3\,\text{V}$. As visible in the images, the potential in the gap reaches $\sim -2\,\text{V}$ to $-3\,\text{V}$ at $V_{GS} = -8\,\text{V}$.

Fig. 6.12(a)-(d) shows for the same applied $V_{DS} = 1.3\,\text{V}$ the evolution of the electrostatic potential while increasing V_{GS} from 0 V to −8 V in the crossectional xz plane in the middle of the nanogap ($y = 0$) as indicated by the white dashed line in Fig. 6.11(b). From $V_{GS} \approx -5\,\text{V}$ on, there is a rather continuous potential $< -2\,\text{V}$ at the bottom of the nanogap channel.

This is even better visible if the potential is plotted along the white dashed lines in Fig. 6.12(d) which is depicted in Fig.6.13. Fig. 6.13(b) shows the potential curves along the gap height (z) for $x = 100\,\text{nm}$ and $y = 0$, so in the middle of the channel in both, x and y. As expected, the greatest change in the potential occurs directly at the SiO_2 interface, at the bottom of the gap and is decreased to the top of the gap since the gate contact is more distant. Since we studied monolayers in the nanogap, the potential close to the SiO_2 interface is most relevant.

Fig.6.13(a) shows the potential at the SiO_2 interface in the middle of the gap ($y = z = 0$) along the channel length (x) from the source to the drain electrode for V_{GS} from 0 V to −8 V at V_{DS} = 1.3 V. The potential in the gap is continuously lowered up to $\sim -2.5\,\text{V}$ in the middle of the channel for $V_{GS} = -8\,\text{V}$. With increasing V_{GS} the slope of the potential curves becomes significantly greater which results in an increased electrical field at the electrodes. This might lead to an enhanced injection of charge carriers into the SAM.

This becomes clearer with the energy diagram of a functionalized nanogap electrode. Fig.6.14

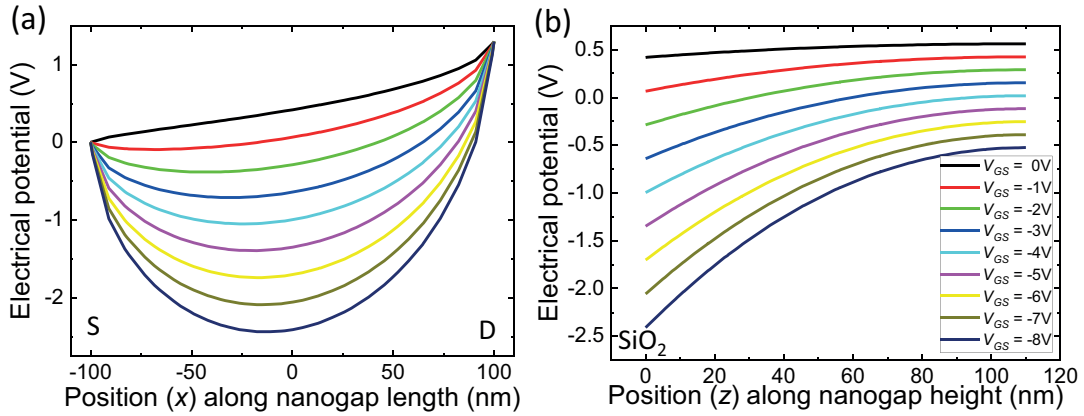

Figure 6.13 Electrostatic potential in the middle of the nanogap ($y = 0$) at $V_{DS} = 1.3\,\text{V}$ as function of V_{GS} as indicated by the white dashed lines in Fig. 6.12(d); (a) in x-direction along the nanogap length ($z = 0$) and (b) in z-direction along the nanogap height ($x = 0$). Reprinted (adapted) with permission from [117]. Copyright (2019) IEEE.

shows the proposed simplified energy diagram of a PAphenyl SAM in the nanogap electrode in

close analogy to Fig. 6.6. With the doping level of the Si electrodes, we calculate $E_V - E_F \approx$ 34 meV according to 6.1.2. The HOMO/LUMO levels are taken from [148].

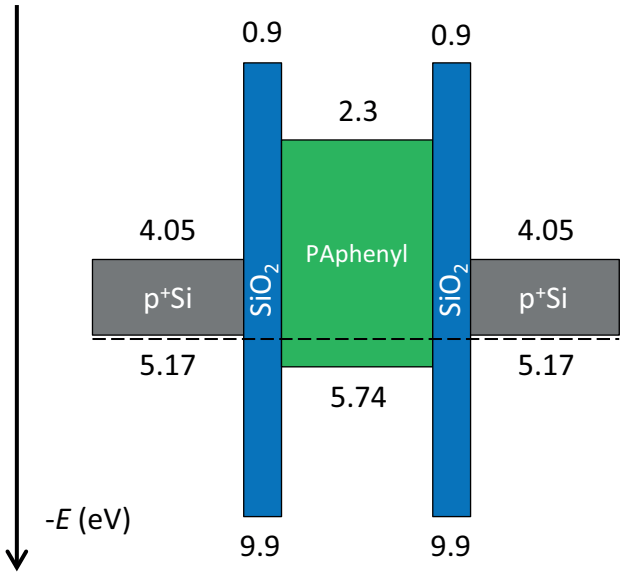

Figure 6.14 Proposed energy diagram of a functionalized nanogap electrode device with PAphenyl in equilibrium without applied voltage and with respect to the vacuum level. Energy values for Si and SiO_2 are taken from [147], HOMO/LUMO energy values are taken from [148]. Charging, interface states and band bending in Si is neglected.

Due to the alignment of the energy levels, there is a smaller offset between the HOMO level and Fermi level than between the LUMO level and the Fermi level. The HOMO offset is estimated as $\phi_{HOMO} \approx 540$ meV. Hence, the potential change at the Si electrodes due to the applied V_{GS} up to -8 V should possibly enhance the charge transport through the PAphenyl SAM. However it needs to be noted that several simplifications are considered in this picture since the HOMO/LUMO levels were determined for an isolated molecule in gas phase and not as part of a SAM which changes the energy levels. We also neglected the influence of the SiO_2 layers and any further coupling of the molecules with the Si electrodes itself.

6.2.2 Monolayer characterization

Si nanogap electrode devices fabricated by RIE and EBL were used to study the electrical properties of SAMs of PAphenyl. The SAMs were grown using the T-BAG method (cf. 3.2.6) on a wafer chip comprising an array of Si nanogap electrodes and on planar, p^+-Si/ SiO_2 reference samples for surface analysis. The detailed parameters of the functionalization process can be found in the Appendix D.2.

We first characterized the SAMs by CA measurements. SAM-functionalized samples were more hydrophobic (contact angle: $\sim 88°$) compared to the bare SiO_2 surface ($\sim 23°$) after the Piranha treatment step which is ascribed to the presence of aromatic groups, similar as discussed

in Section 6.1.1. The greater CA indicated that the SAM functionalization was successful. Ellipsometry measurements were used to determine the thickness of the SiO_2 layer of the reference sample after the Piranha treatment and before the SAM functionalization. We used the reactive index and extinction coefficient given in Tab. 6.1 to model the sample based on the obtained ellipsometry data. The reference sample was modeled as a layer stack of Air/ SiO_2/Si while Si was assumed to be opaque. We obtained a SiO_2 thickness of (1.55 ± 0.01) nm based on 5 measurements on the sample. The obtained SiO_2 thickness is close to the SiO_2 thickness measured in Section 6.1.1 ((1.39 ± 0.07) nm) and is in the expected thickness range for a native SiO_2 layer (1 nm to 2 nm).

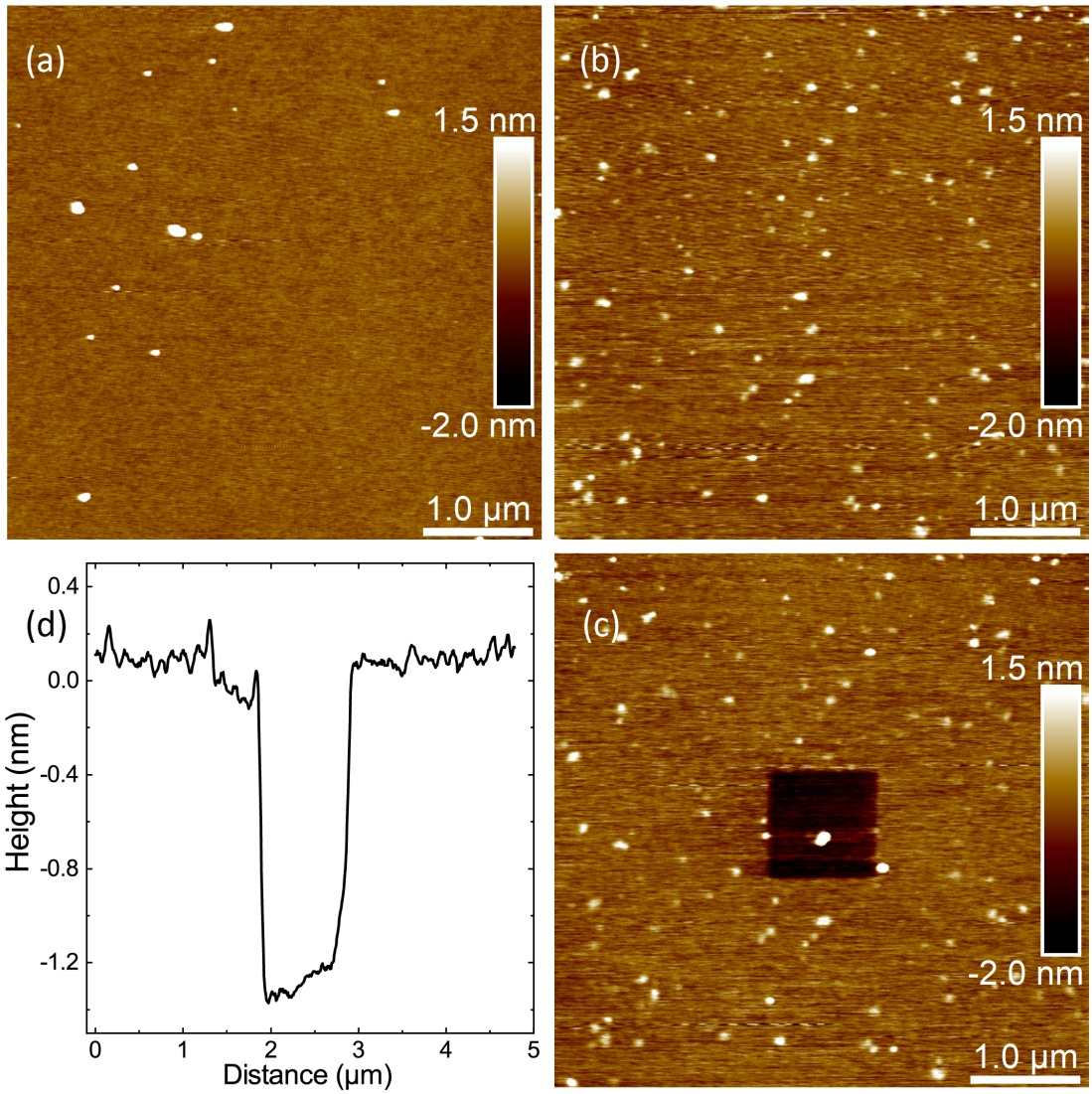

Figure 6.15 AFM images of PAphenyl SAM functionalized samples. (a) SiO_2/Si reference sample before SAM deposition. (b) PAphenyl SAM functionalized sample after second T-BAG process. (c) Same sample as in (b) after AFM scratching of a $1 \times 1\ \mu m^2$ area. (d) Averaged height profile of scratched region in (c). Reprinted (adapted) with permission from [117]. Copyright (2019) IEEE.

We characterized the SAM of PAphenyl additionally by AFM. Fig. 6.15(a) shows a tapping mode AFM image of the Si/ SiO_2 reference sample. Besides distinct small particles, visible as white spots with a height > 10 nm which we identified as unintentional contamination particles of the sample surface after sample preparation, originating possibly from the lab environment, there is a relatively smooth surface. The RMS roughness is determined as 0.2 nm based on a $1 \times 1\,\mu m^2$ scan area without contamination particles. Fig. 6.15(b)-(c) show tapping mode AFM images of the PAphenyl SAM. A small RMS roughness of 0.3 nm was measured, comparable to the bare Si/ SiO_2 reference sample which indicates also the formation of a uniform and dense SAM and agrees well with literature values for a PAphenyl SAM [148].
We used AFM nanolithography scratching to determine the thickness of the PAphenyl SAM (cf. Fig. 6.15(c)). Fig. 6.15(d) shows the obtained averaged height profile of one scratched SAM area. We measured the step height at 3 spots on the sample which determines the thickness of the PAphenyl SAM to $d = (1.22 \pm 0.34)$ nm, which is in good agreement with the expectation (estimated molecule length $\sim$ 1 nm by *ChemSketch/ACDlabs* software) as well as with literature which gives additionally the corresponding tilting angle of $\sim 32°$ for a PAphenyl SAM [148].

6.2.3 Electrical characterization of functionalized three terminal nanogap devices

We characterized the Si nanogap electrode devices functionalized with organophosphosphonate SAMs electrically by measuring their *I-V* characteristics in a 3-terminal configuration by contacting the metal pads of a single Si nanogap device with the probes of a vacuum probestation ($p \approx 5 \times 10^{-6}$ mbar) at room temperature in darkness. Thanks to the thicker SiO_2 layer of 200 nm compared to Section 6.1.3 gate-dependent measurements were possible. The global back gate was contacted via the triax sample stage.
We electrically characterized a wafer chip containing an array of 100 Si nanogap electrode devices. All nanogap devices were first electrically pre-characterized by measuring the *I-V* characteristics of all empty nanogap electrode devices right after their fabrication. Only those showing complete electrical insulating behavior, i. e., no visible increase in current and a resistance in the TΩ regime, were taken into account for the electrical characterization after SAM functionalization. 19 devices were not completely etched and discarded. After these reference measurements of the as-fabricated empty nanogap devices, all nanogap samples were functionalized with SAMs of PAphenyl and subsequently electrically characterized. While most devices did not show conductance above the noise level after SAM functionalization, two structures revealed a pronounced nonlinear increase in conductance.
Fig. 6.16(a) shows the output characteristics of one device ($l = 200$ nm, $w = 200\,\mu$m). Measured currents I_{DS} were in the nA range and were clearly dependent on the applied gate voltage V_{GS}, up to −8 V, consistent with field-effect transistor operation. The measured devices showed only small corresponding gate leakage currents I_{GS} which were 2-3 order of magnitudes less then I_{DS}. The modulation of I_{DS} was only achieved for negative V_{GS}, indicating p-type trans-

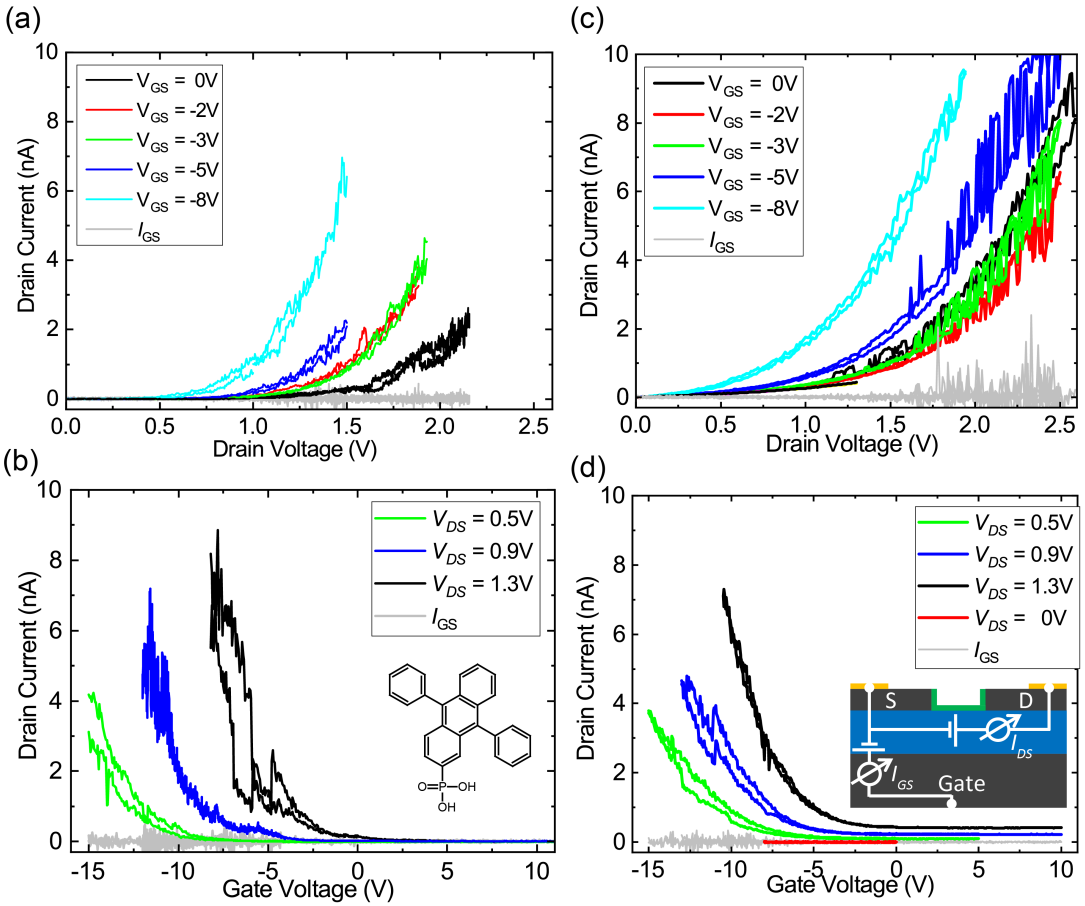

Figure 6.16 (a) Output and (b) transfer characteristic of a SAM-functionalized Si nanogap electrode device, as function of gate voltage; channel length: $l = 200\,\text{nm}$; electrode width: $w = 200\,\mu\text{m}$. I_{GS} denotes the measured gate (leakage) current. Inset (b): sketch of PAphenyl. (c) Output and (d) transfer characteristic of a SAM-functionalized Si nanogap electrode device, as function of gate voltage; channel length: $l = 200\,\text{nm}$; electrode width: $w = 100\,\mu\text{m}$. Inset: electrical measurement configuration. Reprinted (adapted) with permission from [117]. Copyright (2019) IEEE.

port in the SAM as anticipated for anthracene-based organic semiconductors. The transfer characteristics (Fig. 6.16(b)) show $I_{DS}V_{GS}$ sweeps for gate voltages down to $V_{GS} = -15\,\text{V}$ for V_{DS} between 0.5 V to 1.3 V. We observed no saturation of I_{DS} in the output characteristics for the applied V_{GS}. This might be attributed to a non-ideal electrical contact from the electrodes to the SAM [53] and additionally to short channel effects owing to the small aspect ratio of the transistor device of $l/d = 1$ (d: gate oxide thickness).

Fig. 6.16(c) and (d) shows the output and transfer characteristics of a device with $l = 200\,\text{nm}$ and $w = 100\,\mu\text{m}$. The general behavior is similar to the $w = 200\,\mu\text{m}$ device, there is a modulation of I_{DS} for negative gate voltages. Remarkably, the overall current values in the output characteristics are roughly comparable between (a) and (c). Since in (c) the electrode width is smaller, the general expectation is that also I_{DS} is smaller. A possible explanation could be that the current is not equally flowing over the whole width of the electrodes but rather

at distinct areas which would explain the missing scaling with electrode width. Also local defects in the SAM could lead to this behavior. Nevertheless, due to the clear modulation with V_{GS}, quantitative transistor parameters can be estimated using the equation for the linear region of the output characteristics (cf. Eq. 2.8). From the slope of the transfer characteristics we calculate the mobility to be $\mu \approx 1 \times 10^{-4}\,\mathrm{cm}^2/\mathrm{Vs}$ which is comparable to reported mobility values for phosphonate based SAMFETs [149, 150] but less than the highest reported values for SAMFETs [151, 152] in general. These mobility values are the first reported values for SAMs of 2-phosphono-9,10-diphenyl-anthracene to the best of our knowledge. Calculated threshold voltages vary with V_{DS} and are $V_{th} = -11.34\,\mathrm{V}$, $-8.63\,\mathrm{V}$ and $-3.96\,\mathrm{V}$ for $V_{DS} = 0.5\,\mathrm{V}$, $0.9\,\mathrm{V}$ and $1.3\,\mathrm{V}$, respectively, in case of the $w = 200\,\mu\mathrm{m}$ device and $V_{th} = -9.37\,\mathrm{V}$, $-6.89\,\mathrm{V}$ and $-6.78\,\mathrm{V}$ for $V_{DS} = 0.5\,\mathrm{V}$, $0.9\,\mathrm{V}$ and $1.3\,\mathrm{V}$ in case of the $w = 100\,\mu\mathrm{m}$ device.

It needs to be noted, that the nanogap channel lengths of $l = 200\,\mathrm{nm}$ in combination with the $200\,\mathrm{nm}$ thick SiO_2 gate insulating layer is rather too short in the context of the gradual channel approximation which is assumed in Eq. 2.8. Also the absence of the saturation regime requires care while evaluating the linear approximation of the I-V curves in the transfer characteristics. Nevertheless, we consider the order of magnitude of the obtained mobility as good first estimation for SAMs of PAphenyl.

6.2.4 Summary

In this section, we studied the electrical OFET characteristics of silicon nanogap electrodes functionalized with a SAM of PAphenyl. Finite element simulations of the empty nanogap device indicated significant electrostatic potential changes, sufficient for field effect modulation of a PAphenyl SAM in the nanogap while applying gate voltages up to $-8\,V$. The SAM quality was investigated by analyzing the SAM surface morphology. We found that our self-assembly functionalization protocol gave rise to the formation of a uniform and dense SAM as has been characterized by water CA and AFM measurements. Electrical characterization showed a clear modulation of I_{DS} with negative gate voltages up to $-8\,\mathrm{V}$ which indicates p-type transport. A first estimation of the mobility in the order of $\mu \approx 1 \times 10^{-4}\,\mathrm{Vs/cm}^2$ for SAMs of PAphenyl was obtained.

7 Conclusion & Outlook

In this work, we have presented the development and electrical characterization of all-silicon electrode devices which were employed to study the electrical transport through thin films of novel organic and hybrid organic/inorganic materials on the nanoscale. In particular, the gaps between the electrodes were filled with thin films of functionalized SiNCs and SAMs of organophosphonate molecules.

We fabricated the planar, highly doped Si nanogap electrodes from silicon-on-insulator substrates by either utilizing anisotropical etching in potassium hydroxide (KOH) solution or by the combination of electron beam lithography (EBL) and reactive ion etching (RIE). Contact separations in the range of 200 nm were realized for the KOH etched gaps and nanogaps as small as 30 nm were achieved in case of the electrodes prepared by EBL/RIE, by optimizing the EBL and etching parameters.

Nanogaps filled with SiNCs

The gaps prepared by EBL/RIE between the electrodes of height 110 nm were filled with thin films of either hexyl- (Hex-), phenyl- (Phen-) or phenylacetylene- (PA-) functionalized SiNCs (diameter 3 nm) from colloidal dispersions. A key factor to succeed in reliable measurements of these films in the high-resistance regime was a novel technique of filling the space between electrodes from solution, via a pressure-transducing PDMS membrane. This procedure led to homogeneous and dense thin films without any cracks or voids, and with precise control of the film thickness. The film composition was studied for thin films of Hex-SiNCs by X-ray photoelectron spectroscopy (XPS) measurements which showed a constant relative Si/Carbon ratio for all investigated film thicknesses and almost no oxidation of the SiNCs after film preparation. This indicated, that our PDMS membrane based coating technique is suitable to fabricate comparable thin films of SiNCs of different film thicknesses without change in film composition. The volume fraction of the Hex-SiNCs in the film was estimated as 0.73 via the Maxwell-Garnett effective medium approximation which indicated a rather dense packing of the SiNCs in the film. We derived this estimation from impedance measurements of SiNCs on planar Si samples which were modeled with an equivalent network of resistor-capacitor circuits. The corresponding relative permittivity of the Hex-SiNC thin film was determined as 4.43.

The electrical functionality of our devices was demonstrated for thin films of functionalized SiNCs of various thicknesses, filled into the 40 nm to 200 nm trenches separating the Si

electrodes. Conductance was significantly enhanced compared to untreated devices and estimated conductivity values for Hex-SiNC thin films were in the range of $1 \times 10^{-9}\,\Omega^{-1}\,\mathrm{cm}^{-1}$ to $1 \times 10^{-8}\,\Omega^{-1}\,\mathrm{cm}^{-1}$. The obtained current-voltage (I-V) characteristics showed the anticipated scaling with channel width, ranging from 5 µm to 50 µm, and with film thickness, ranging from 15 nm to 92 nm. A strongly hysteretic I-V dependence together with a successive decrease of current with time or with the number of I-V cycles can be assigned to SCLC-transport, with the functionalized SiNCs providing efficient charge trap centers. The interpretation in terms of SCLC transport was supported by numerical kinetic Monte Carlo (kMC) simulations which modeled the experimental I-V data well. For the kMC simulations, randomly distributed, energetically deep lying trap states with a trap density in the order of $1 \times 10^{17}\,\mathrm{cm}^{-3}$ in the SiNC film were assumed. Charge transport was then described by a hopping process of the charge carriers between adjacent, weakly bound SiNCs by employing the Miller-Abrahams hopping rate.

Future studies should focus on a detailed microscopic understanding of this transport including the influence of the nature of different surface bound organic molecules which can be varied over a wide range. For this purpose, temperature-dependent measurements over a large temperature range would be beneficial towards further insight in the charge transport processes through the SiNC films. A key factor is the improvement of the film quality in the case of PA-SiNCs and Phen-SiNCs. One possible starting point is the systematic study of different SiNC solvents besides toluene which might lead to an enhanced dispersion of the SiNCs. This could improve the film quality for the PDMS membrane based coating process and lead to similar homogeneous SiNC thin films in the nanogaps as it was presented for Hex-SiNCs in this work. As an alternative coating method, spray coating can be taken into account which was already demonstrated as a reliable coating technique for planar films of hydrogen terminated SiNCs [36].
In view of potential electrical device applications, it would be necessary to enhance the overall conductivity of the highly resistive SiNC thin films. One possibility is enhancing the charge carrier density via doping of the SiNCs [153–155]. In addition, the influence of the electrodes regarding doping type (n-doping, p-doping), doping level and contact resistance are interesting and necessary topics for further investigations.
In summary, we have demonstrated that all-silicon electrode devices may serve as platform for the electrical characterization of thin films of functionalized, undoped silicon nanocrystals.

Nanogaps bridged with organophosphonate SAMs

Nanogaps prepared by both fabrication methods, EBL/RIE and anisotropical etching in KOH solutions, were coated with self-assembled monolayers (SAMs) of aromatic organophosphonate molecules. The gaps prepared by KOH were coated with 2-phosphono-9,10-diphenylanthracene (PAphenyl) molecules as well as with 1-hexadecanphosphonic acid (PAC16) molecules as an aliphatic reference molecule, without any aromatic moieties. Water contact angle (CA),

atomic force microscopy (AFM) and ellipsometry characterization measurements on planar SAM coated Si/ SiO_2 samples showed uniform and dense SAMs. We used an AFM nanolithography scratching technique to measure the thickness of the SAM as (1.12 ± 0.22) nm in case of PAanthrac which was in agreement with ellipsometry. We conducted ab-initio calculations of the PAanthrac molecule in gas phase based on density functional theory (DFT) to reveal its molecular structure as well as its electronic properties. The DFT simulations showed that the anthracene side groups of the molecule are rotated by $\sim 90°$ with respect to the molecule backbone. These side groups are also the place where the highest occupied molecular orbital (HOMO) is located whereas the lowest unoccupied molecular orbital (LUMO) is mainly located at the molecule backbone. The corresponding HOMO-LUMO gap was calculated as 3.05 eV. The theoretical length of the PAanthrac molecule in gas phase was determined by DFT as 1.29 nm. Electrical I-V characterization showed a significantly increased lateral conductance of PAanthrac SAMs compared to PAC16 SAMs as well as to the empty (as-fabricated) gap. We attributed this increase in lateral conductance of the PAanthrac SAM to the aromatic substituents of the PAanthrac molecules, in particular to the possible overlap of anthracene side groups of adjacent molecules (π-π-stacking).
The gaps prepared by EBL/RIE were coated with SAMs of 2-phosphono-9,10-diphenylanthracene (PAphenyl) molecules. CA and AFM measurements on planar SAM coated Si/ SiO_2 reference samples revealed a uniform and dense monolayer with a thickness of (1.22 ± 0.34) nm. These devices were characterized electrically as field effect transistors, and the measurements were supported by finite element simulations of the electrostatic characteristics of the nanogap. Lateral conductance was greatly improved compared to an untreated device and we observed only low gate leakage currents which were at least 2-3 orders of magnitude smaller compared to the source-drain current. A distinct field-effect induced modulation of the source drain current was observed for negative gate voltages which indicated p-type transport. A first estimation of the mobility in the order of $1 \times 10^{-4}\,\mathrm{cm}^2/\mathrm{Vs}$ for SAMs of PAphenyl molecules was extracted from the measurement data.

Future studies should focus on a detailed investigation of the lateral charge transport in SAMs of aromatic organophosphonate molecules. A detailed understanding of the possible overlap of adjacent aromatic moieties of the molecules could lead to an enhanced transistor operation towards a self-assembled field effect transistor (SAMFET). For this purpose, molecules with different side groups could be of interest. Temperature-dependent measurements would be also in this case advantageous to achieve a better understanding of the microscopic nature of charge transport. Furthermore, the doping level as well as the nature of doping of the SOI substrates could be modified. This would change the corresponding work function of the electrodes and provide another parameter to engineer the electrical characteristics of the device.
The KOH based fabrication process could be used with SOI wafers incorporating a thicker buried oxide layer. This would certainly reduce the gate leakage currents and enable field-effect

measurements also for these nanogap devices. It would be interesting to see if the different geometries of the nanogap cross-section which are related to the fabrication process, influence the electronic coupling of the molecules of the SAM to the electrodes. Additionally, the exchange of KOH with tetramethylammonium hydroxide (TMAH) could lead to an improved nanogap quality, since TMAH can produce smooth sidewalls [156, 157].
In summary, we have demonstrated that our Si nanogap electrode devices fabricated by either EBL/RIE or anisotropical etching in KOH solution, can serve as an electrical base structure for the lateral electrical characterization of organophosphonate SAMs. We have additionally demonstrated field-effect transistor operation of an all-Si nanogap electrode device functionalized with an aromatic phosphonate monolayer. Possible future applications of the demonstrated devices could be, e.g., in the field of sensing applications with the surface of the SAM as active detector area.

In conclusion, we suggest our planar, all-silicon device architecture and functionalization methodology as platform for investigations of the electrical transport properties of thin films of various novel hybrid materials, in particular in the high-resistivity range. Beyond our demonstrated networks of functionalized nanocrystals and aromatic monolayers, this may include biomolecules, nanowires, carbon based nano composites and novel 2D materials.

A Functionalized SiNCs

A.1 Fabrication and characterization of functionalized SiNCs

The following Section is based on the published article: Space charge-limited current transport in thin films of alkyl-functionalized silicon nanocrystals [116] (Simon Pfaehler et al., Nanotechnology, 30(39) (2019), 395201, DOI: 10.1088/1361-6528/ab2c28)[1].

Functionalization of SiNCs

The functionalization of SiNCs is described exemplary for hexyl functionalized SiNCs [27, 116, 158]:
Freshly etched hydride-terminated SiNCs (from 300 mg Si/ SiO_2 composite) were dispersed in 2 ml dry toluene and transferred to a Schlenk flask equipped with a stir bar. The dispersion was degassed via three freeze-thaw cycles. n-hexyllithium (0.2 mmol), from 2.3 M solution in hexane) was added. Upon addition of n-hexyllithium, the color of the reaction mixture turned dark brown. The reaction mixture was stirred at room temperature for 15 hours under argon atmosphere. Functionalized SiNCs were precipitated in 5 ml 1 : 1 ethanol-methanol mixture, acidified with HCl conc. (0.2 ml) to terminate the reaction. SiNCs were centrifuged at 9000 rpm for 5 min and the sediment was redispersed in minimum amount of toluene. The precipitation-centrifugation-redispersion cycle was repeated two more times from toluene and ethanol-methanol. At the end of purification steps, functionalized Hex-SiNCs were dispersed in 2 ml toluene and filtered through a 0.45 µm PTFE syringe filter. This method assures a controlled, less dense monolayer coverage on the SiNC surface, unlike many other conventional surface functionalization techniques [159].

Characterization of functionalized SiNCs

Upon surface functionalization, presence of hexyl groups on the SiNCs' surface was observed via Fourier-Transform Infrared spectroscopy (FTIR). Fig. A.1(a) shows the observed FTIR spectrum. Presence of alkyl peaks between 2850 cm^{-1} to 2955 cm^{-1} (CH_2 and CH_3 ν-stretching) and at $\sim$ 1462 cm^{-1} and $\sim$ 1378 cm^{-1} (CH δ-deformation) is a good indication for a successful

[1] Reprinted (adapted) from [116]. Copyright (2019) IOP Publishing Ltd, Creative Commons BY 3.0 license (http://creativecommons.org/licenses/by/3.0)

reaction [77]. The spectrum also shows signals assigned for Si-H groups at ~2100 cm^{-1}, 906 cm^{-1} and 660 cm^{-1}, together with minor oxidation evidenced by the Si-O band at 1050 cm^{-1}. Transmission electron microscopy (TEM) revealed an average SiNC size (diameter) of d = (3.1 ± 0.2) nm (cf. Fig. A.1(b)). A histogram showing the size distribution is provided in Fig. A.1(c). The mean and standard deviation was calculated by measuring the size of 300 SiNCs. The FTIR spectrum was collected with a *Bruker Vertex* 70 FTIR using a Platinum ATR

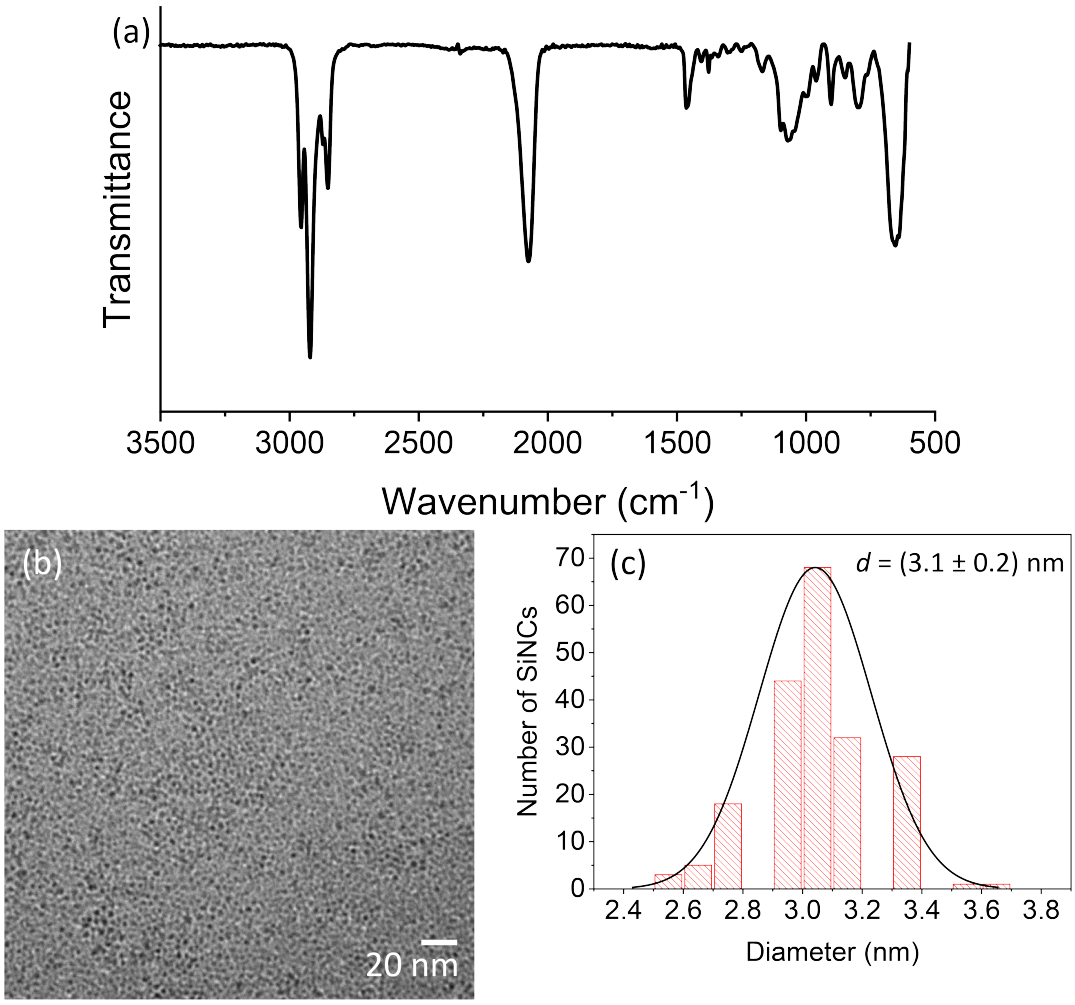

Figure A.1 (a) FTIR plot of Hex-SiNCs (in solution). (b) TEM image of drop-casted Hex-SiNC thin film. (c) Hex-SiNC size histogram, showing a Hex-SiNC diameter of d = (3.1 ± 0.2) nm.

from *Bruker*. Bright field TEM images were obtained using a *JEOL*-2012 electron microscope equipped with a LaB6 filament and operated at an acceleration voltage of 200 kV.

A.2 SEM characterization of nanogaps filled with functionalized SiNCs

Si nanogap electrode devices were filled with thin films of PA-SiNCs and Phen-SiNC as described in Section 4.3.4. Unlike the nanogap filling with Hex-SiNCs, the PA-SiNCs and Phen-SiNCs formed inferior films in the nanogap devices as can be seen in the cross-sectional SEM images of Fig. A.2 for nanogaps with $l = 100\,\mathrm{nm}$ filled with PA-SiNCs (Fig. A.2(a)) and Phen-SiNCs (Fig. A.2(b)) from $c = 20\,\mathrm{mg/ml}$ solution concentration, respectively. Possibly this originates from less dispersed solutions in case of PA-SiNCs and Phen-SiNCs compared to the nicely film forming Hex-SiNCs solutions. As a consequence, aggregates of SiNCs might have formed in the solutions which prevented homogeneous film formation.

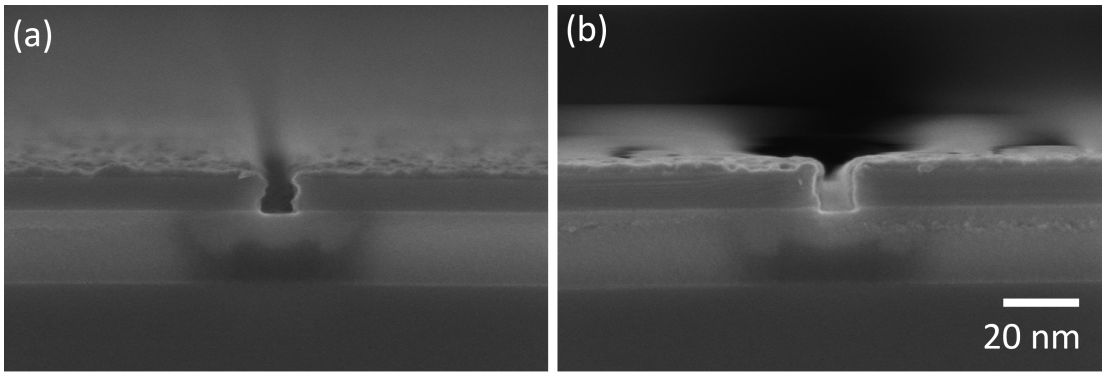

Figure A.2 Cross sectional SEM images of $l = 100\,\mathrm{nm}$ nanogaps filled with (a) PA-SiNC and (b) Phen-SiNC thin films from a $c = 20\,\mathrm{mg/ml}$ solution. Scale bar is valid for (a) and (b).

A.3 Influence of gate potential on functionalized SiNCs thin films

We used the highly p-doped Si substrate of our nanogap electrode samples as a global back gate for nanogap devices filled with SiNCs. Fig. A.3 shows the gate-dependent measurements on a nanogap device with $l = 100\,\text{nm}$ and $w = 5\,\mu\text{m}$, filled with Hex-SiNCs from a solution with $c = 20\,\text{mg/ml}$. Solid lines show the source drain current I_{DS} and dashed lines show the corresponding gate leakage current I_{GS}. First, I_{DS} was measured at an applied gate voltage $V_{\text{GS}} = 0\,\text{V}$ (black curve), then at $V_{\text{GS}} = 100\,\text{V}$ (red), $V_{\text{GS}} = -100\,\text{V}$ (green) and finally at $V_{\text{GS}} = 0\,\text{V}$ (blue) again. As apparent from the figure, there is no significant difference in the source-current visible except for $V_{\text{GS}} = -100\,\text{V}$. But in this case, the leakage current I_{GS} is about the same as I_{DS}. No significant gate-dependent effect could therefore be measured. The high leakage current is possibly rather related to the measurement circuitry for the sample, since it is not present for positive gate voltages.

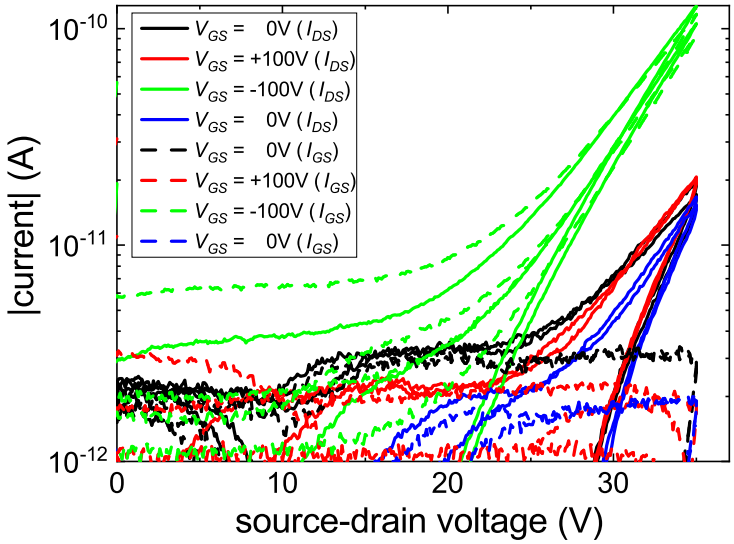

Figure A.3 Gate-dependent measurements of a nanogap device ($l = 100\,\text{nm}$, $w = 5\,\mu\text{m}$) filled with Hex-SiNCs from a $c = 20\,\text{mg/ml}$ solution.

A.4 Influence of light on current-voltage characteristics of functionalized SiNCs

We illuminated a nanogap device ($l = 100\,\text{nm}$, $w = 5\,\mu\text{m}$) filled with Hex-SiNCs from a $c = 20\,\text{mg/ml}$ solution with an ultraviolet torch light (wavelength: $\sim 450\,\text{nm}$) from *Ril Chemie* while keeping the device at a fixed bias of 35 V. The time-dependent current signal is depicted in Fig. A.4 for a series of switching the light on and off. There was a response visible of the device once the light source was switched on as well once it was switched off. The current increased about 60 % when the light was switched on. This light sensitive behavior may be worth to consider for potential sensor applications, although the overall currents are low.

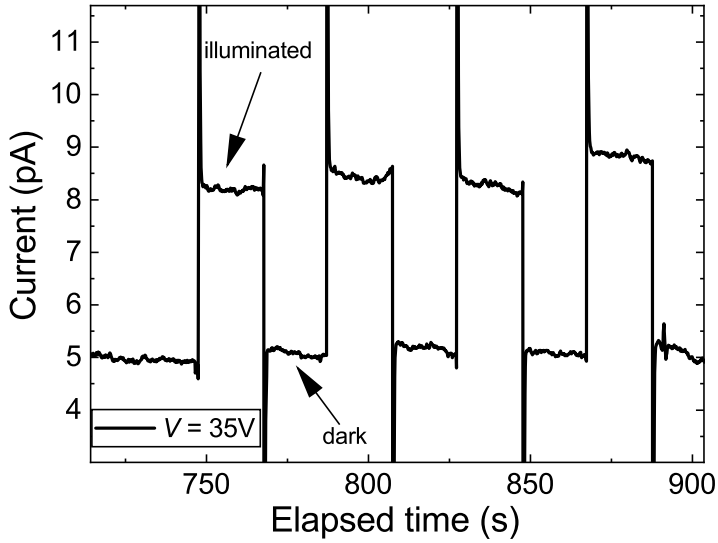

Figure A.4 Influence of UV illumination on the current of a nanogap device ($l = 100\,\text{nm}$, $w = 5\,\mu\text{m}$) at $V = 35\,\text{V}$ filled with Hex-SiNCs from a $c = 20\,\text{mg/ml}$ solution.

A.5 Influence of temperature on functionalized SiNC thin films

We measured temperature-dependent *I*-*V* curves for a nanogap device ($l = 40\,\text{nm}$, $w = 5\,\mu\text{m}$) filled with Hex-SiNCs from solution ($c = 20\,\text{mg/ml}$). For every different temperature, we used a fresh device and only the first voltage scans of the devices are presented in Fig. A.5. We increased the temperature from room temperature up to a maximum of $T = 475\,\text{K}$ and decreased the temperature finally again to room temperature. As visible in the figure, there is no clear trend with temperature visible for the measured *I*-*V* curves. One reason could be that the sample was not sufficiently in thermal contact with the stage (no thermal grease was used), thus the real temperature of the sample deviated possibly from the applied temperature. It would be interesting to measure the temperature dependency over a broader range, in particularly also at low temperatures.

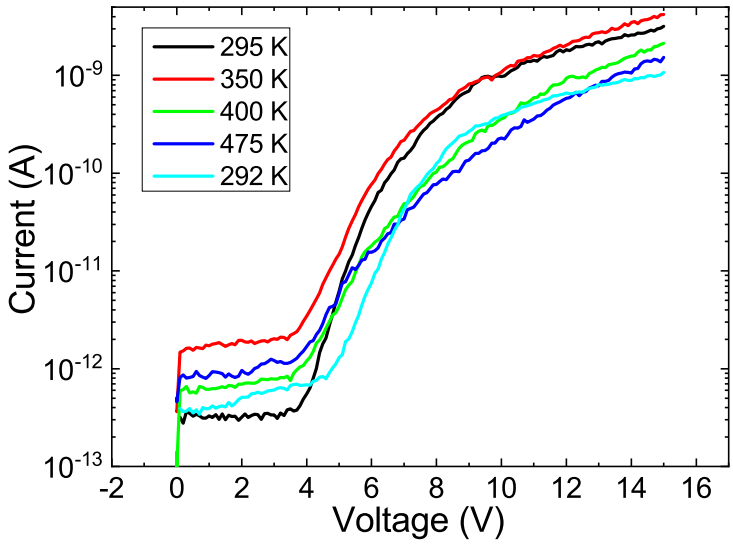

Figure A.5 Influence of temperature (first voltage scans) on a nanogap device ($l = 40\,\text{nm}$, $w = 5\,\mu\text{m}$) filled with Hex-SiNCs from solution ($c = 20\,\text{mg/ml}$).

A.6 Photoluminescence spectroscopy on planar thin films of functionalized SiNCs

We measured PL on planar Hex-SiNC thin films which were coated on fused silica glass (semiconductor grade, *Plan Optik AG*) substrates using the same PDMS technique as on the Si nanogap samples (cf., Section 4.3.4). All PL measurements were conducted in Prof. Dr. Frank Hegmann's lab at the University of Alberta (Edmonton, Canada) with the support of Mary Narreto.

All measurements were conducted with a 250 kHz pulsed excitation laser at a wavelength of 400 nm. Fig. A.6 shows the temperature series of the PL measurements for Hex-SiNC films (liquid N_2 cooling) which were conducted with a laser power of 190 µW. There is a red shift of the peak wavelength visible with increasing temperature.

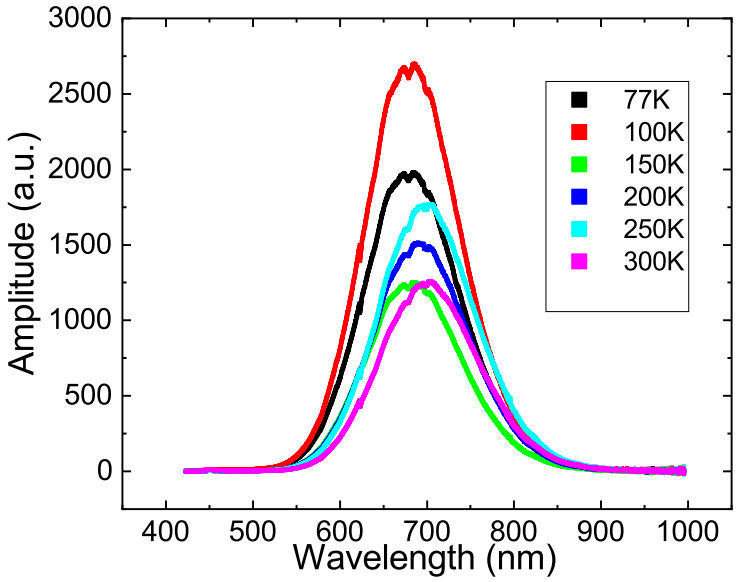

Figure A.6 PL signal of Hex-SiNC thin film as function of temperature.

We additionally conducted time resolved PL measurements at different temperatures ranging from 77 K to 300 K. For these measurements, we used a single photon avalanche detector in combination with an oscilloscope. As depicted in Fig. A.7 the general behavior is a slow decay of the PL signal, with time scales in the µs regime.

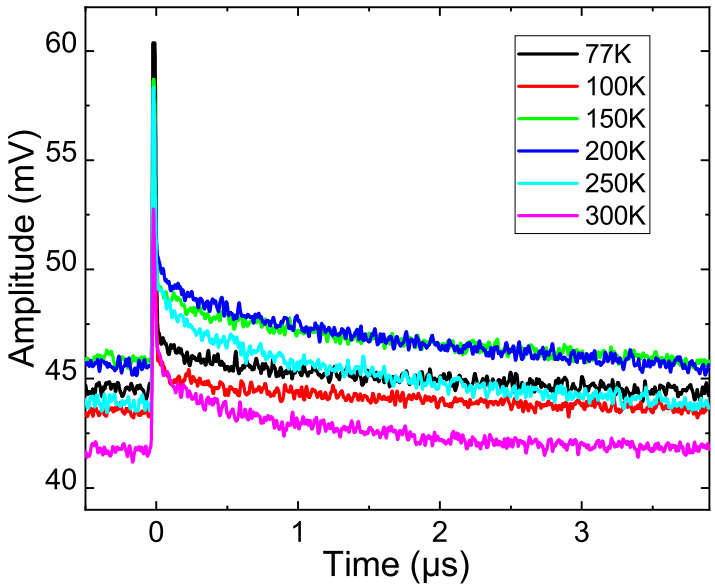

Figure A.7 Time resolved PL signal of Hex-SiNC thin film as function of temperature.

B Ferroelectric polymer PVDF-TrFE

All measurements related to PVDF-TrFE were conducted in Prof. Dr. Jillian Buriak's lab at the University of Alberta (Edmonton/Canada) with the support of Mahmoud Almadhoun.

B.1 PVDF-TrFE capacitor with shadow evaporated Au top contact

We measured a capacitor diode consisting of a shadow evaporated gold contact on top of a layer of the ferroelectric polymer PVDF-TrFE (thickness: $\sim$ 200 nm) which was spin-coated on a highly p-doped Si substrate. The device showed the typical butterfly shaped capacitance-voltage characteristics [160].

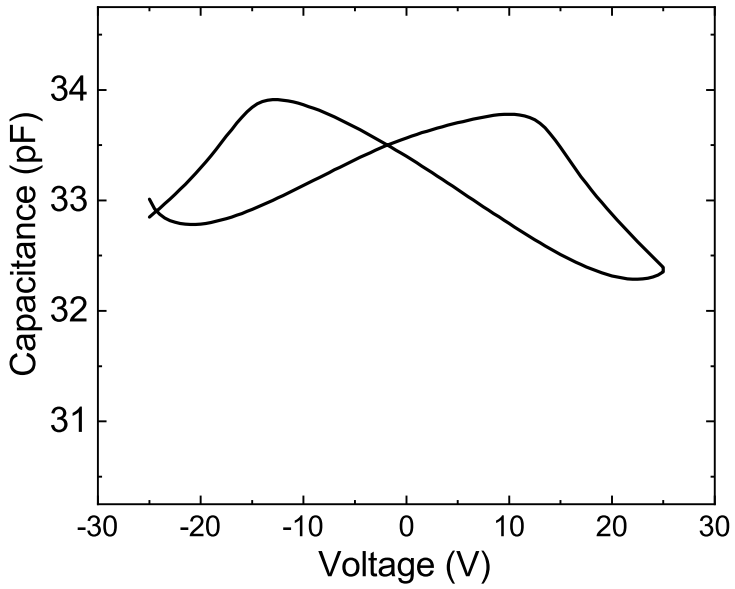

Figure B.1 Capacitance-voltage measurement of a p-Si/PVDF-TrFE/Au device with shadow evaporated Au contact of size $25 \times 25\,\mu m^2$.

B.2 PVDF-TrFE in silicon nanogap electrode device

We coated our nanogap electrode devices with the 200 nm thick PVDF-TrFE film via spin coating. One device showed a similar capacitance-voltage curve as the previously discussed capacitor diodes, as depicted in Fig. B.2. Although the curve is distorted, the characteristic butterfly shape of the ferroelectric polymer is still visible.

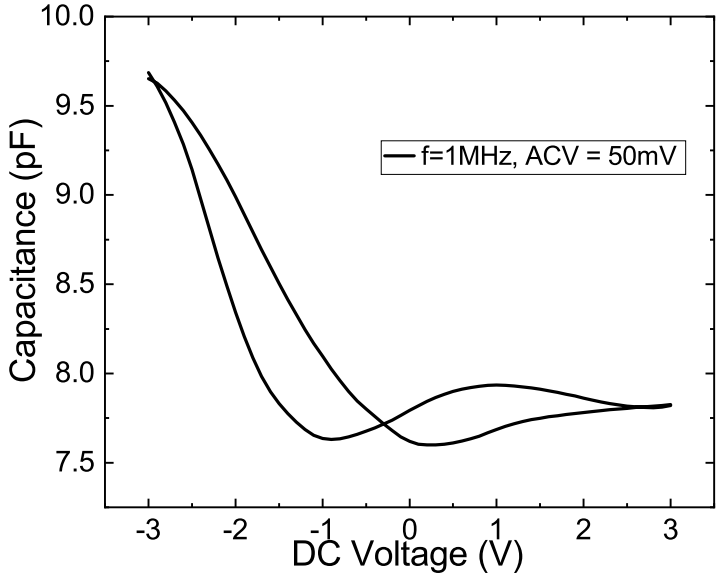

Figure B.2 Capacitance-voltage measurement of a silicon nanogap (l = 50 nm, w = 200 µm) filled with PVDF-TrFE.

C Transfer printed metal contacts on planar organophosphonate based SAMs

We used transfer printing to achieve gold top contacts on organophosphonate SAMs which were grown on aluminium-oxide/aluminium layers[1]. The detailed fabrication process is well described in [162]. Fig. C.1 shows the obtained *I-V* curves for SAMs fom alkyl organophosphonate molecules of different chain length (C4-C12) as well as for two reference samples, one aluminium oxide/Al sample without SAM and a second aluminium oxide/Al sample which was additionally immersed in ethanol (without molecules). In general, the longer the carbon chain, the lower the current which fits to the anticipation, that longer alkyl molecules should lead to a thicker tunneling barrier. However, the C8 sample is not following this trend. Possibly, the SAM quality was not sufficient, or multilayers lead to a thicker molecular film.

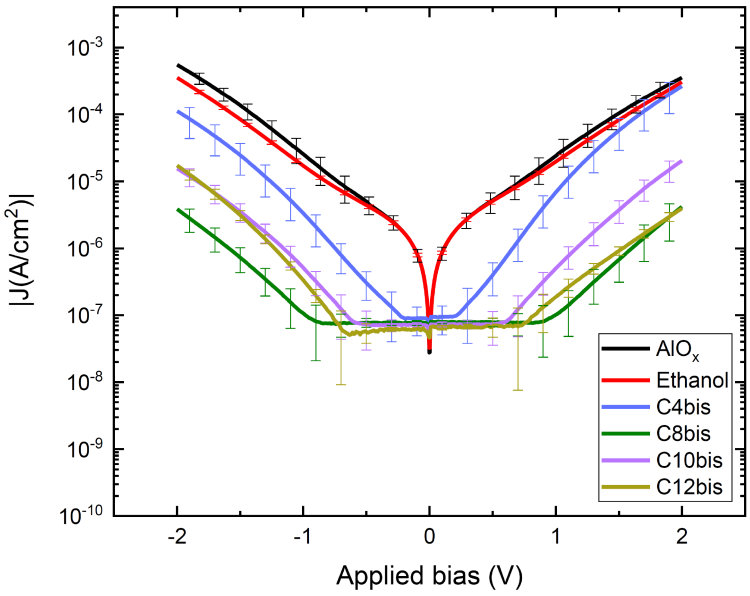

Figure C.1 *I-V* curves of transfer printed gold contacts (size: $80 \times 80\mu m^2$) on top of SAMs of alkyl organophosphonate molecules of different chain length. Apparent plateaus at low bias: measurement artifact (resolution limit).

[1]The experimental work on the transfer printed metal contacts on organophosphonate SAMs presented in this Section was obtained in collaboration with Aykut Turfanda as part of his master's thesis [161].

D Functionalization parameters for organophosphonate SAMs on silicon oxide

D.1 Nanogap samples prepared by KOH etching

Pre-cleaning of samples

The samples were pre-cleaned by immersing them successively in the following solvents while sonicating them for 5 min at 37 kHz respectively:

1. DI H_2O
2. isopropanol
3. acetone
4. isopropanol

The samples were finally dry-blown with N_2 gas.

Pre-functionalization treatments

1. Oxygen plasma (200 W, 5 min, 1.4 mbar, *100-E Technics Plasma System*)
2. Basic piranha (5 : 1 : 1 ratio of H_2O : NH_4OH : H_2O_2, 10 min, 110 °C)
3. Sonication for 10 min, immersed in DI H_2O
4. N_2 dry-blow
5. Heated in N_2 atmosphere (120 °C, 5 min)

Functionalization by T-BAG process

The following T-BAG procedure and mutilayer removal procedure was repeated twice in case of PAC16 and three times in case of PAanthrac.

- PAanthrac: 2.5 µM in tetrahydrofuran (THF)
- PAC16: 25 µM in tetrahydrofuran (THF)
- Heating the samples in N_2 atmosphere at 120 °C for 16 h

Removing multilayers

The samples were immersed in different solvents and sonicated at 37 kHz.
Samples functionalized with PAanthrac:

1. 2× ethanol/toluene (1 : 1, 10 min)
2. ethanol for 20 min

Samples functionalized with PAC16:

1. 2× ethanol, 5 min
2. DI H_2O/THF (10 : 3, 10 min)
3. DI H_2O, 10 min
4. ethanol, 20 min

The samples are then dry-blown with N_2 and heated in an oven at 120 °C for 5 min in N_2 atmosphere.

D.2 Nanogap samples prepared by RIE etching

Pre-cleaning of samples

The samples were pre-cleaned by immersing them successively in the following solvents while sonicating them for 5 min at 37 kHz respectively:

1. acetone
2. isopropanol

The samples were finally dry-blown with N_2 gas.

Pre-functionalization treatments

1. Basic piranha (5 : 1 : 1 ratio of H_2O : NH_4OH : H_2O_2, 10 min, 75 °C)
2. Thoroughly rinsing with DI H_2O
3. N_2 dry-blow

Functionalization by T-BAG process

The following T-BAG procedure and mutilayer removal procedure was repeated twice in case of PAphenyl.

- PAphenyl: 20 µM in tetrahydrofuran (THF)
- Heating the samples in N_2 atmosphere at 140 °C for 24 h

Removing multilayers

The samples were successively immersed in different solvents and sonicated at 37 kHz. If necessary, this procedure was repeated twice:

1. 2× methanol/THF (1 : 1, 5 min)
2. isopropanol for 10 min

The samples were finally dry-blown with N_2 gas.

Bibliography

[1] G. E. Moore: Cramming more components onto integrated circuits, Reprinted from Electronics, volume 38, number 8, April 19, 1965, pp.114 ff. IEEE Solid-State Circuits Society Newsletter **11**(3) (2006), 33–35. DOI: 10.1109/N-SSC.2006.4785860 (cit. on p. 1).

[2] H. Ling, S. Liu, Z. Zheng, and F. Yan: Organic Flexible Electronics. Small Methods **2**(10) (2018), 1800070. DOI: 10.1002/smtd.201800070 (cit. on p. 1).

[3] A. K. Bansal, S. Hou, O. Kulyk, E. M. Bowman, and I. D. W. Samuel: Wearable Organic Optoelectronic Sensors for Medicine. Advanced materials (Deerfield Beach, Fla.) **27**(46) (2015), 7638–7644. DOI: 10.1002/adma.201403560 (cit. on p. 1).

[4] W. Kang, C. Yan, C. Y. Foo, and P. S. Lee: Foldable Electrochromics Enabled by Nanopaper Transfer Method. Advanced Functional Materials **25**(27) (2015), 4203–4210. DOI: 10.1002/adfm.201500527 (cit. on p. 1).

[5] J.-D. Kim, Y.-J. Baek, Y. Jin Choi, C. Jung Kang, H. Ho Lee, H.-M. Kim, K.-B. Kim, and T.-S. Yoon: Investigation of analog memristive switching of iron oxide nanoparticle assembly between Pt electrodes. Journal of Applied Physics **114**(22) (2013), 224505. DOI: 10.1063/1.4846759 (cit. on p. 1).

[6] R. Wang, X. Wu, K. Xu, W. Zhou, Y. Shang, H. Tang, H. Chen, and Z. Ning: Highly Efficient Inverted Structural Quantum Dot Solar Cells. Advanced materials (Deerfield Beach, Fla.) **30**(7) (2018). DOI: 10.1002/adma.201704882 (cit. on p. 1).

[7] P. Müller-Buschbaum, M. Thelakkat, T. F. Fässler, and M. Stutzmann: Hybrid Photovoltaics - from Fundamentals towards Application. Advanced Energy Materials **7**(16) (2017), 1700248. DOI: 10.1002/aenm.201700248 (cit. on p. 1).

[8] A. Nozik: Quantum dot solar cells. Physica E: Low-dimensional Systems and Nanostructures **14**(1-2) (2002), 115–120. DOI: 10.1016/S1386-9477(02)00374-0 (cit. on p. 1).

[9] Y. Shirasaki, G. J. Supran, M. G. Bawendi, and V. Bulović: Emergence of colloidal quantum-dot light-emitting technologies. Nature Photonics **7**(1) (2013), 13–23. DOI: 10.1038/nphoton.2012.328 (cit. on p. 1).

[10] B. S. Mashford, M. Stevenson, Z. Popovic, et al.: High-efficiency quantum-dot light-emitting devices with enhanced charge injection. Nature Photonics **7**(5) (2013), 407–412. DOI: 10.1038/nphoton.2013.70 (cit. on p. 1).

[11] J. M. Caruge, J. E. Halpert, V. Wood, V. Bulović, and M. G. Bawendi: Colloidal quantum-dot light-emitting diodes with metal-oxide charge transport layers. Nature Photonics **2**(4) (2008), 247–250. DOI: 10.1038/nphoton.2008.34 (cit. on p. 1).

[12] V. I. Klimov: Optical Gain and Stimulated Emission in Nanocrystal Quantum Dots. Science **290**(5490) (2000), 314–317. DOI: 10.1126/science.290.5490.314 (cit. on p. 1).

[13] N. N. Ledentsov: Quantum dot laser. Semiconductor Science and Technology **26**(1) (2011), 014001. DOI: 10.1088/0268-1242/26/1/014001 (cit. on p. 1).

[14] S. Gao, C. Zhang, Y. Liu, et al.: Lasing from colloidal InP/ZnS quantum dots. Optics express **19**(6) (2011), 5528–5535. DOI: 10.1364/OE.19.005528 (cit. on p. 1).

[15] R. Freeman and I. Willner: Optical molecular sensing with semiconductor quantum dots (QDs). Chemical Society reviews **41**(10) (2012), 4067–4085. DOI: 10.1039/c2cs15357b (cit. on p. 1).

[16] Z. Yue, F. Lisdat, W. J. Parak, S. G. Hickey, L. Tu, N. Sabir, D. Dorfs, and N. C. Bigall: Quantum-dot-based photoelectrochemical sensors for chemical and biological detection. ACS applied materials & interfaces **5**(8) (2013), 2800–2814. DOI: 10.1021/am3028662 (cit. on p. 1).

[17] S. Silvi and A. Credi: Luminescent sensors based on quantum dot-molecule conjugates. Chemical Society reviews **44**(13) (2015), 4275–4289. DOI: 10.1039/c4cs00400k (cit. on p. 1).

[18] M. Bruchez Jr.: Semiconductor Nanocrystals as Fluorescent Biological Labels. Science **281**(5385) (1998), 2013–2016. DOI: 10.1126/science.281.5385.2013 (cit. on p. 1).

[19] B. Dubertret, P. Skourides, D. J. Norris, V. Noireaux, A. H. Brivanlou, and A. Libchaber: In vivo imaging of quantum dots encapsulated in phospholipid micelles. Science (New York, N.Y.) **298**(5599) (2002), 1759–1762. DOI: 10.1126/science.1077194 (cit. on p. 1).

[20] X. Michalet, F. F. Pinaud, L. A. Bentolila, J. M. Tsay, S. Doose, J. J. Li, G. Sundaresan, A. M. Wu, S. S. Gambhir, and S. Weiss: Quantum dots for live cells, in vivo imaging, and diagnostics. Science (New York, N.Y.) **307**(5709) (2005), 538–544. DOI: 10.1126/science.1104274 (cit. on p. 1).

[21] European Commission: Directive 2011/65/EU of the European Parliament and of the Council of 8 June 2011 on the restriction of the use of certain hazardous substances in electrical and electronic equipment. Official Journal of the European Union **54**(1) (2011), 88–110 (cit. on p. 1).

[22] J. Liu, F. Erogbogbo, K.-T. Yong, et al.: Assessing clinical prospects of silicon quantum dots: Studies in mice and monkeys. ACS Nano **7**(8) (2013), 7303–7310. DOI: 10.1021/nn4029234 (cit. on pp. 2, 5).

[23] G. Ledoux, J. Gong, F. Huisken, O. Guillois, and C. Reynaud: Photoluminescence of size-separated silicon nanocrystals: Confirmation of quantum confinement. Applied Physics Letters **80**(25) (2002), 4834–4836. DOI: 10.1063/1.1485302 (cit. on pp. 2, 5).

[24] H. Rinnert, O. Jambois, and M. Vergnat: Photoluminescence properties of size-controlled silicon nanocrystals at low temperatures. Journal of Applied Physics **106**(2) (2009), 023501. DOI: 10.1063/1.3169513 (cit. on p. 2).

[25] D. Jurbergs, E. Rogojina, L. Mangolini, and U. Kortshagen: Silicon nanocrystals with ensemble quantum yields exceeding 60%. Applied Physics Letters **88**(23) (2006), 233116. DOI: 10.1063/1.2210788 (cit. on p. 2).

[26] M. Dasog, De los Reyes, Glenda B, L. V. Titova, F. A. Hegmann, and Veinot, Jonathan G C: Size vs surface: tuning the photoluminescence of freestanding silicon nanocrystals across the visible spectrum via surface groups. ACS Nano **8**(9) (2014), 9636–9648. DOI: 10.1021/nn504109a (cit. on p. 2).

[27] A. Angı, R. Sinelnikov, A. Meldrum, J. G. C. Veinot, I. Balberg, D. Azulay, O. Millo, and B. Rieger: Photoluminescence through in-gap states in phenylacetylene functionalized silicon nanocrystals. Nanoscale (2016). DOI: 10.1039/C6NR01435F (cit. on pp. 2, 95).

[28] R. J. Clark, M. Aghajamali, C. M. Gonzalez, et al.: From Hydrogen Silsesquioxane to Functionalized Silicon Nanocrystals. Chemistry of Materials **29**(1) (2016), 80–89. DOI: 10.1021/acs.chemmater.6b02667 (cit. on pp. 2, 16).

[29] X. Cheng, S. B. Lowe, P. J. Reece, and J. J. Gooding: Colloidal silicon quantum dots: From preparation to the modification of self-assembled monolayers (SAMs) for bio-applications. Chemical Society reviews **43**(8) (2014), 2680–2700. DOI: 10.1039/c3cs60353a (cit. on p. 2).

[30] K. Dohnalová, T. Gregorkiewicz, and K. Kůsová: Silicon quantum dots: Surface matters. Journal of physics. Condensed matter : an Institute of Physics journal **26**(17) (2014), 173201. DOI: 10.1088/0953-8984/26/17/173201 (cit. on p. 2).

[31] T. Zhou, R. T. Anderson, H. Li, J. Bell, Y. Yang, B. P. Gorman, S. Pylypenko, M. T. Lusk, and A. Sellinger: Bandgap Tuning of Silicon Quantum Dots by Surface Functionalization with Conjugated Organic Groups. Nano letters **15**(6) (2015), 3657–3663. DOI: 10.1021/nl504051x (cit. on p. 2).

[32] M. Dasog, J. Kehrle, B. Rieger, and Veinot, Jonathan G C: Silicon Nanocrystals and Silicon-Polymer Hybrids: Synthesis, Surface Engineering, and Applications. Angewandte Chemie (International ed. in English) **55**(7) (2016), 2322–2339. DOI: 10.1002/anie.201506065 (cit. on p. 2).

[33] A. Zabet-Khosousi and A.-A. Dhirani: Charge transport in nanoparticle assemblies. Chemical reviews **108**(10) (2008), 4072–4124. DOI: 10.1021/cr0680134 (cit. on p. 2).

[34] T.-H. Le, K.-J. Kim, and H.-D. Jeong: Effect of Thermal Cross-Linking of 4-Ethynylstyryl Capping Groups on Electronic Coupling between Silicon Quantum Dots in Silicon Quantum Dot Solids. The Journal of Physical Chemistry C **121**(29) (2017), 15957–15969. DOI: 10.1021/acs.jpcc.7b02702 (cit. on p. 2).

[35] N. Rastgar, D. J. Rowe, R. J. Anthony, B. A. Merritt, U. R. Kortshagen, and E. S. Aydil: Effects of water adsorption and surface oxidation on the electrical conductivity of silicon nanocrystal films. Journal of Physical Chemistry C **117**(8) (2013), 4211–4218. DOI: 10.1021/jp308279m (cit. on p. 2).

[36] W. Aigner, M. Wiesinger, H. Wiggers, M. Stutzmann, and R. N. Pereira: Three-Dimensional Percolation and Performance of Nanocrystal Field-Effect Transistors. Physical Review Applied **5**(5) (2016), 2146. DOI: 10.1103/PhysRevApplied.5.054017 (cit. on pp. 2, 57, 92).

[37] W. Aigner, O. Bienek, D. Desta, H. Wiggers, M. Stutzmann, and R. N. Pereira: Optoelectronic properties and depth profile of charge transport in nanocrystal films. Physical Review B **96**(3) (2017). DOI: 10.1103/PhysRevB.96.035404 (cit. on p. 2).

[38] W. Aigner, O. Bienek, B. P. Falcão, S. U. Ahmed, H. Wiggers, M. Stutzmann, and R. N. Pereira: Intra- and inter-nanocrystal charge transport in nanocrystal films. Nanoscale **10**(17) (2018), 8042–8057. DOI: 10.1039/C8NR00250A (cit. on p. 2).

[39] M. A. Rafiq, Z. A. K. Durrani, H. Mizuta, M. M. Hassan, and S. Oda: Field-dependant hopping conduction in silicon nanocrystal films. Journal of Applied Physics **104**(12) (2008), 123710. DOI: 10.1063/1.3050332 (cit. on p. 2).

[40] M. A. Rafiq, Y. Tsuchiya, H. Mizuta, S. Oda, S. Uno, Z. A. K. Durrani, and W. I. Milne: Charge injection and trapping in silicon nanocrystals. Applied Physics Letters **87**(18) (2005), 182101. DOI: 10.1063/1.2119431 (cit. on pp. 2, 57).

[41] M. A. Rafiq, Y. Tsuchiya, H. Mizuta, S. Oda, S. Uno, Z. A. K. Durrani, and W. I. Milne: Hopping conduction in size-controlled Si nanocrystals. Journal of Applied Physics **100**(1) (2006), 014303. DOI: 10.1063/1.2209808 (cit. on p. 2).

[42] T. A. Burr, A. A. Seraphin, E. Werwa, and K. D. Kolenbrander: Carrier transport in thin films of silicon nanoparticles. Physical Review B **56**(8) (1997), 4818–4824. DOI: 10.1103/PhysRevB.56.4818 (cit. on pp. 2, 57).

[43] T. Chen, B. Skinner, W. Xie, B. I. Shklovskii, and U. R. Kortshagen: Carrier Transport in Films of Alkyl-Ligand-Terminated Silicon Nanocrystals. The Journal of Physical Chemistry C **118**(34) (2014), 19580–19588. DOI: 10.1021/jp5051723 (cit. on pp. 2, 57).

[44] W. Helfrich and W. G. Schneider: Transients of Volume–Controlled Current and of Recombination Radiation in Anthracene. The Journal of Chemical Physics **44**(8) (1966), 2902–2909. DOI: 10.1063/1.1727152 (cit. on p. 2).

[45] M. Pope, H. P. Kallmann, and P. Magnante: Electroluminescence in Organic Crystals. The Journal of Chemical Physics **38**(8) (1963), 2042–2043. DOI: 10.1063/1.1733929 (cit. on p. 2).

[46] M. Chen, L. Yan, Y. Zhao, I. Murtaza, H. Meng, and W. Huang: Anthracene-based semiconductors for organic field-effect transistors. Journal of Materials Chemistry C **6**(28) (2018), 7416–7444. DOI: 10.1039/C8TC01865K (cit. on p. 2).

[47] J. Li, Y. Zhao, H. S. Tan, et al.: A stable solution-processed polymer semiconductor with record high-mobility for printed transistors. Scientific reports **2** (2012), 754. DOI: 10.1038/srep00754 (cit. on p. 2).

[48] B. Gburek and V. Wagner: Influence of the semiconductor thickness on the charge carrier mobility in P3HT organic field-effect transistors in top-gate architecture on flexible substrates. Organic Electronics **11**(5) (2010), 814–819. DOI: 10.1016/j.orgel.2010.01.023 (cit. on p. 2).

[49] H. Sirringhaus: 25th anniversary article: Organic field-effect transistors: the path beyond amorphous silicon. Advanced materials (Deerfield Beach, Fla.) **26**(9) (2014), 1319–1335. DOI: 10.1002/adma.201304346 (cit. on p. 2).

[50] F. Dinelli, M. Murgia, P. Levy, M. Cavallini, F. Biscarini, and de Leeuw, Dago M.: Spatially Correlated Charge Transport in Organic Thin Film Transistors. Physical Review Letters **92**(11) (2004). DOI: 10.1103/PhysRevLett.92.116802 (cit. on p. 2).

[51] C. R. Kagan, A. Afzali, R. Martel, L. M. Gignac, P. M. Solomon, A. G. Schrott, and B. Ek: Evaluations and Considerations for Self-Assembled Monolayer Field-Effect Transistors. Nano Letters **3**(2) (2003), 119–124. DOI: 10.1021/nl0259075 (cit. on p. 2).

[52] Smits, Edsger C. P., Mathijssen, Simon G. J., van Hal, Paul A., et al.: Bottom-up organic integrated circuits. Nature **455**(7215) (2008), 956–959. DOI: 10.1038/nature07320 (cit. on p. 2).

[53] M. Mottaghi, P. Lang, F. Rodriguez, A. Rumyantseva, A. Yassar, G. Horowitz, S. Lenfant, D. Tondelier, and D. Vuillaume: Low-Operating-Voltage Organic Transistors Made of Bifunctional Self-Assembled Monolayers. Advanced Functional Materials **17**(4) (2007), 597–604. DOI: 10.1002/adfm.200600179 (cit. on pp. 2, 89).

[54] T. Schmaltz, A. Y. Amin, A. Khassanov, T. Meyer-Friedrichsen, H.-G. Steinrück, A. Magerl, J. J. Segura, K. Voitchovsky, F. Stellacci, and M. Halik: Low-Voltage Self-Assembled Monolayer Field-Effect Transistors on Flexible Substrates. Advanced Materials **25**(32) (2013), 4511–4514. DOI: 10.1002/adma.201301176 (cit. on p. 2).

[55] A. Ringk, W. S. Christian Roelofs, E. C. Smits, Van der Marel, Cees, I. Salzmann, A. Neuhold, G. H. Gelinck, R. Resel, de Leeuw, Dago M., and P. Strohriegl: n-Type self-assembled monolayer field-effect transistors for flexible organic electronics. Organic Electronics **14**(5) (2013), 1297–1304. DOI: 10.1016/j.orgel.2013.02.016 (cit. on p. 2).

[56] M. Halik and A. Hirsch: The Potential of Molecular Self-Assembled Monolayers in Organic Electronic Devices. Advanced Materials **23**(22-23) (2011), 2689–2695. DOI: 10.1002/adma.201100337 (cit. on p. 2).

[57] A. Cattani-Scholz: Functional Organophosphonate Interfaces for Nanotechnology: A Review. ACS applied materials & interfaces **9**(31) (2017), 25643–25655. DOI: 10.1021/acsami.7b04382 (cit. on p. 2).

[58] M. McDowell, I. G. Hill, J. E. McDermott, S. L. Bernasek, and J. Schwartz: Improved organic thin-film transistor performance using novel self-assembled monolayers. Applied Physics Letters **88**(7) (2006), 73505. DOI: 10.1063/1.2173711 (cit. on p. 3).

[59] S. A. DiBenedetto, A. Facchetti, M. A. Ratner, and T. J. Marks: Molecular Self-Assembled Monolayers and Multilayers for Organic and Unconventional Inorganic Thin-Film Transistor Applications. Advanced Materials **21**(14-15) (2009), 1407–1433. DOI: 10.1002/adma.200803267 (cit. on p. 3).

[60] H. Ma, O. Acton, D. O. Hutchins, N. Cernetic, and A. K.-Y. Jen: Multifunctional phosphonic acid self-assembled monolayers on metal oxides as dielectrics, interface modification layers and semiconductors for low-voltage high-performance organic field-effect transistors. Physical chemistry chemical physics : PCCP **14**(41) (2012), 14110–14126. DOI: 10.1039/c2cp41557g (cit. on p. 3).

[61] A. Pathak, A. Bora, K.-C. Liao, H. Schmolke, A. Jung, C.-P. Klages, J. Schwartz, and M. Tornow: Disorder-derived, strong tunneling attenuation in bis-phosphonate monolayers. Journal of physics. Condensed matter : an Institute of Physics journal **28**(9) (2016), 94008. DOI: 10.1088/0953-8984/28/9/094008 (cit. on p. 3).

[62] A. Cattani-Scholz, K.-C. Liao, A. Bora, A. Pathak, C. Hundschell, B. Nickel, J. Schwartz, G. Abstreiter, and M. Tornow: Molecular Architecture: Construction of Self-Assembled Organophosphonate Duplexes and Their Electrochemical Characterization. Langmuir **28**(20) (2012), 7889–7896. DOI: 10.1021/la301610a (cit. on pp. 3, 73, 77).

[63] A. C. Aragonès, N. Darwish, S. Ciampi, F. Sanz, J. J. Gooding, and I. Díez-Pérez: Single-molecule electrical contacts on silicon electrodes under ambient conditions. Nature communications **8** (2017), 15056. DOI: 10.1038/ncomms15056 (cit. on p. 3).

[64] C. Jia and X. Guo: Molecule-electrode interfaces in molecular electronic devices. Chemical Society reviews **42**(13) (2013), 5642–5660. DOI: 10.1039/c3cs35527f (cit. on p. 3).

[65] D. R. Strachan, D. E. Smith, M. D. Fischbein, D. E. Johnston, B. S. Guiton, M. Drndić, D. A. Bonnell, and A. T. Johnson: Clean electromigrated nanogaps imaged by transmission electron microscopy. Nano letters **6**(3) (2006), 441–444. DOI: 10.1021/nl052302a (cit. on p. 3).

[66] M. I. Schukfeh, L. Sepunaru, P. Behr, W. Li, I. Pecht, M. Sheves, D. Cahen, and M. Tornow: Towards nanometer-spaced silicon contacts to proteins. Nanotechnology **27**(11) (2016), 115302. DOI: 10.1088/0957-4484/27/11/115302 (cit. on p. 3).

[67] G. Rydzek, D. Toulemon, A. Garofalo, et al.: Selective Nanotrench Filling by One-Pot Electroclick Self-Constructed Nanoparticle Films. Small (Weinheim an der Bergstrasse, Germany) **11**(36) (2015), 4638–4642. DOI: 10.1002/smll.201500639 (cit. on pp. 3, 42).

[68] H. B. Akkerman and B. de Boer: Electrical conduction through single molecules and self-assembled monolayers. Journal of Physics: Condensed Matter **20**(1) (2008), 13001. DOI: 10.1088/0953-8984/20/01/013001 (cit. on p. 3).

[69] Y. C. Ju, S. Kim, T.-G. Seong, S. Nahm, H. Chung, K. Hong, and W. Kim: Resistance random access memory based on a thin film of CdS nanocrystals prepared via colloidal synthesis. Small (Weinheim an der Bergstrasse, Germany) **8**(18) (2012), 2849–2855. DOI: 10.1002/smll.201200488 (cit. on p. 3).

[70] S. Pfaehler, K. Keim, R. Csiki, Q. H. Nguyen, K.-C. Liao, M. Stutzmann, J. Schwartz, A. Cattani-Scholz, and M. Tornow: A nanogap electrode platform for organic monolayer-film devices. 2016 IEEE 16th International Conference on Nanotechnology (IEEE-NANO) (Sendai, Japan). IEEE, 2016, 842–844. DOI: 10.1109/NANO.2016.7751507 (cit. on pp. 3, 31, 33, 71, 81, 125).

[71] G. J. Ashwell, L. J. Phillips, B. J. Robinson, et al.: Molecular bridging of silicon nanogaps. ACS Nano **4**(12) (2010), 7401–7406. DOI: 10.1021/nn102460z (cit. on p. 3).

[72] S. W. Howell, S. M. Dirk, K. Childs, H. Pang, M. Blain, R. J. Simonson, J. M. Tour, and D. R. Wheeler: Mass-fabricated one-dimensional silicon nanogaps for hybrid organic/nanoparticle arrays. Nanotechnology **16**(6) (2005), 754–758. DOI: 10.1088/0957-4484/16/6/022 (cit. on p. 3).

[73] R. Sinelnikov, M. Dasog, J. Beamish, A. Meldrum, and J. G. C. Veinot: Revisiting an Ongoing Debate: What Role Do Surface Groups Play in Silicon Nanocrystal Photoluminescence? ACS Photonics **4**(8) (2017), 1920–1929. DOI: 10.1021/acsphotonics.7b00102 (cit. on p. 5).

[74] J. M. Buriak: Organometallic Chemistry on Silicon and Germanium Surfaces. Chemical Reviews **102**(5) (2002), 1271–1308. DOI: 10.1021/cr000064s (cit. on p. 5).

[75] R. Boukherroub, S. Morin, F. Bensebaa, and D. D. M. Wayner: New Synthetic Routes to Alkyl Monolayers on the Si(111) Surface 1. Langmuir **15**(11) (1999), 3831–3835. DOI: 10.1021/la9901478 (cit. on p. 5).

[76] J. E. Bateman, R. D. Eagling, D. R. Worrall, B. R. Horrocks, and A. Houlton: Alkylation of Porous Silicon by Direct Reaction with Alkenes and Alkynes. Angewandte Chemie International Edition **37**(19) (1998), 2683–2685. DOI: 10.1002/(SICI)1521-3773(19981016)37:19<2683::AID-ANIE2683>3.0.CO;2-Y (cit. on p. 5).

[77] I. M. D. Hohlein, A. Angi, R. Sinelnikov, J. G. C. Veinot, and B. Rieger: Functionalization of hydride-terminated photoluminescent silicon nanocrystals with organolithium reagents. Chemistry (Weinheim an der Bergstrasse, Germany) **21**(7) (2015), 2755–2758. DOI: 10.1002/chem.201405555 (cit. on pp. 5, 16, 96).

[78] L. M. Wheeler, N. R. Neale, T. Chen, and U. R. Kortshagen: Hypervalent surface interactions for colloidal stability and doping of silicon nanocrystals. Nature communications **4** (2013). DOI: 10.1038/ncomms3197 (cit. on p. 5).

[79] A. Köhler and H. Bässler: *Electronic processes in organic semiconductors: An introduction*. Weinheim: Wiley-VCH, 2015 (cit. on pp. 6–8, 13).

[80] P. Mark and W. Helfrich: Space–Charge–Limited Currents in Organic Crystals. Journal of Applied Physics **33**(1) (1962), 205–215. DOI: 10.1063/1.1728487 (cit. on p. 7).

[81] B. I. Shklovskiĭ and A. L. Éfros: Percolation theory and conductivity of strongly inhomogeneous media. Soviet Physics Uspekhi **18**(11) (1975), 845–862. DOI: 10.1070/PU1975v018n11ABEH005233 (cit. on p. 8).

[82] I. I. Fishchuk: On the theory of hopping transport in organic solids with superimposed disorder and polaron effects. Philosophical Magazine B **81**(6) (2006), 561–568. DOI: 10.1080/13642810108225451 (cit. on p. 8).

[83] Monroe: Hopping exponential band tails. Physical Review Letters **54**(2) (1985), 146–149. DOI: 10.1103/PhysRevLett.54.146 (cit. on p. 8).

[84] V. I. Arkhipov, P. Heremans, E. V. Emelianova, G. J. Adriaenssens, and H. Bässler: Weak-field carrier hopping in disordered organic semiconductors: The effects of deep traps and partly filled density-of-states distribution. Journal of Physics: Condensed Matter **14**(42) (2002), 9899–9911. DOI: 10.1088/0953-8984/14/42/305 (cit. on p. 8).

[85] A. Miller and E. Abrahams: Impurity Conduction at Low Concentrations. Physical Review **120**(3) (1960), 745–755. DOI: 10.1103/PhysRev.120.745 (cit. on p. 8).

[86] R. Waser, ed.: *Nanoelectronics and information technology: Advanced electronic materials and novel devices*. 3rd, completely revised and enlarged ed. Weinheim: Wiley-VCH, 2012 (cit. on p. 8).

[87] C. Vericat, M. E. Vela, G. Benitez, P. Carro, and R. C. Salvarezza: Self-assembled monolayers of thiols and dithiols on gold: New challenges for a well-known system. Chemical Society reviews **39**(5) (2010), 1805–1834. DOI: 10.1039/b907301a (cit. on p. 11).

[88] I. Kymissis: *Organic field effect transistors: Theory, fabrication and characterization*. New York, NY: Springer, 2009 (cit. on p. 13).

[89] C. A. Hunter and J. K. M. Sanders: The nature of .pi.-.pi. interactions. Journal of the American Chemical Society **112**(14) (1990), 5525–5534. DOI: 10.1021/ja00170a016 (cit. on p. 14).

[90] J. L. Brédas, J. P. Calbert, D. A. da Silva Filho, and J. Cornil: Organic semiconductors: A theoretical characterization of the basic parameters governing charge transport. Proceedings of the National Academy of Sciences of the United States of America **99**(9) (2002), 5804–5809. DOI: 10.1073/pnas.092143399 (cit. on pp. 14, 77, 79).

[91] T. P. Nguyen, J. H. Shim, and J. Y. Lee: Density Functional Theory Studies of Hole Mobility in Picene and Pentacene Crystals. The Journal of Physical Chemistry C **119**(21) (2015), 11301–11310. DOI: 10.1021/jp511484d (cit. on pp. 14, 77).

[92] J.-L. Brédas, D. Beljonne, V. Coropceanu, and J. Cornil: Charge-transfer and energy-transfer processes in pi-conjugated oligomers and polymers: A molecular picture. Chemical Reviews **104**(11) (2004), 4971–5004. DOI: 10.1021/cr040084k (cit. on pp. 14, 79).

[93] W. Warta, R. Stehle, and N. Karl: Ultrapure, high mobility organic photoconductors. Applied Physics A Solids and Surfaces **36**(3) (1985), 163–170. DOI: 10.1007/BF00624938 (cit. on p. 14).

[94] C. R. Martinez and B. L. Iverson: Rethinking the term "pi-stacking". Chemical Science **3**(7) (2012), 2191. DOI: 10.1039/c2sc20045g (cit. on p. 14).

[95] Howard M. Bank, Martin E. Cifuentes, Theresa E. Martin: Process for the synthesis of soluble, condensed hydridosilicon resins containing low levels of silanol. US5.010.159 (cit. on p. 16).

[96] C. M. Hessel, E. J. Henderson, and J. G. C. Veinot: Hydrogen Silsesquioxane: A Molecular Precursor for Nanocrystalline Si−SiO 2 Composites and Freestanding Hydride-Surface-Terminated Silicon Nanoparticles. Chemistry of Materials **18**(26) (2006), 6139–6146. DOI: 10.1021/cm0602803 (cit. on p. 16).

[97] P. H. Mutin, G. Guerrero, and A. Vioux: Hybrid materials from organophosphorus coupling molecules. Journal of Materials Chemistry **15**(35-36) (2005), 3761. DOI: 10.1039/b505422b (cit. on p. 16).

[98] E. L. Hanson, J. Schwartz, B. Nickel, N. Koch, and M. F. Danisman: Bonding self-assembled, compact organophosphonate monolayers to the native oxide surface of silicon. Journal of the American Chemical Society **125**(51) (2003), 16074–16080. DOI: 10.1021/ja035956z (cit. on pp. 16, 21).

[99] B. Lee, J. Hong, N. Amos, I. Dumer, D. Litvinov, and S. Khizroev: Sub-10-nm-resolution electron-beam lithography toward very-high-density multilevel 3D nanomagnetic information devices. Journal of Nanoparticle Research **15**(6) (2013), 1688. DOI: 10.1007/s11051-013-1665-7 (cit. on p. 18).

[100] Moers Jürgen and S. Okazaki: Advanced optical and particle beam lithography. Nanoelectronics and information technology. Ed. by R. Waser. Weinheim: Wiley-VCH, 2012, 199–218 (cit. on p. 18).

[101] M. Shearn, X. Sun, M. David, A. Yariv, and A. Scherer: Advanced Plasma Processing: Etching, Deposition, and Wafer Bonding Techniques for Semiconductor Applications. Semiconductor Technologies. Ed. by J. Grym. Vukovar, Croatia: InTech, 2010. DOI: 10.5772/8564 (cit. on p. 19).

[102] S. Franssila: *Introduction to microfabrication, second edition*. 2nd ed. Chichester, West Sussex, U.K.: John Wiley & Sons, 2010 (cit. on p. 20).

[103] G. Kovacs, N. I. Maluf, and K. E. Petersen: Bulk micromachining of silicon. Proceedings of the IEEE **86**(8) (1998), 1536–1551. DOI: 10.1109/5.704259 (cit. on p. 20).

[104] K. Keim: Molecular Functionalization and Electrical Characterization of Silicon Nanogap Electrodes Prepared by Anisotropic Etching. Master thesis. Munich: Technical University of Munich, 2015 (cit. on pp. 20, 31, 71).

[105] K. Kristiansen: Scanning electron microscope with energy- and wavelength-dispersive spectrometry. Surface characterization. Ed. by D. Brune. Oslo, Weinheim, and New York: Scandinavian Science Publisher, 1997, 111–128 (cit. on p. 22).

[106] I. Olefjord: X-ray photoelectron spectroscopy. Surface characterization. Ed. by D. Brune. Oslo, Weinheim, and New York: Scandinavian Science Publisher, 1997 (cit. on p. 23).

[107] J. F. Watts: X-ray photoelectron spectroscopy. Vacuum **45**(6-7) (1994), 653–671. DOI: 10.1016/0042-207X(94)90107-4 (cit. on p. 23).

[108] J. H. Scofield: Hartree-Slater subshell photoionization cross-sections at 1254 and 1487 eV. Journal of Electron Spectroscopy and Related Phenomena **8**(2) (1976), 129–137. DOI: 10.1016/0368-2048(76)80015-1 (cit. on p. 23).

[109] L. Mattsson: Scanning probe microscopy. Surface characterization. Ed. by D. Brune. Oslo, Weinheim, and New York: Scandinavian Science Publisher, 1997, 77–81 (cit. on p. 23).

[110] L. G. Rosa and J. Liang: Atomic force microscope nanolithography: Dip-pen, nanoshaving, nanografting, tapping mode, electrochemical and thermal nanolithography. Journal of physics. Condensed matter : an Institute of Physics journal **21**(48) (2009), 483001. DOI: 10.1088/0953-8984/21/48/483001 (cit. on p. 24).

[111] K. E. Bean: Anisotropic etching of silicon. IEEE Transactions on Electron Devices **25**(10) (1978), 1185–1193. DOI: 10.1109/T-ED.1978.19250 (cit. on p. 31).

[112] A. Heuberger: *Mikromechanik: Mikrofertigung mit Methoden der Halbleitertechnologie*. Berlin Heidelberg: Springer, 1991 (cit. on pp. 34, 35).

[113] H. Camon and Z. Moktadir: Atomic scale simulation of silicon etched in aqueous KOH solution. Sensors and Actuators A: Physical **46**(1-3) (1995), 27–29. DOI: 10.1016/0924-4247(94)00854-B (cit. on p. 35).

[114] E. D. Palik, O. J. Glembocki, I. Heard, P. S. Burno, and L. Tenerz: Etching roughness for (100) silicon surfaces in aqueous KOH. Journal of Applied Physics **70**(6) (1991), 3291–3300. DOI: 10.1063/1.349263 (cit. on p. 36).

[115] M. A. Gos lvez and R. M. Nieminen: Surface morphology during anisotropic wet chemical etching of crystalline silicon. New Journal of Physics **5** (2003), 100. DOI: 10.1088/1367-2630/5/1/400 (cit. on p. 36).

[116] S. Pfaehler, A. Angı, D. Chryssikos, A. Cattani-Scholz, B. Rieger, and M. Tornow: Space charge-limited current transport in thin films of alkyl-functionalized silicon nanocrystals. Nanotechnology **30**(39) (2019), 395201. DOI: 10.1088/1361-6528/ab2c28 (cit. on pp. 36, 45, 47, 48, 51, 52, 58, 95, 125).

[117] S. Pfaehler, A. Pathak, K.-C. Liao, J. Schwartz, and M. Tornow: Silicon Nanogap Electrode Engineering for Organic Monolayer Field Effect Transistors. 2019 IEEE 19th International Conference on Nanotechnology (IEEE-NANO) (Macao, China). IEEE, 2019, 521–525. DOI: 10.1109/NANO46743.2019.8993870 (cit. on pp. 37–40, 82, 84, 85, 87, 89, 125).

[118] L. V. Govor, G. H. Bauer, and J. Parisi: A simple method for filling nanogap electrodes with polymer. The Review of Scientific Instrutments **80**(3) (2009), 033902. DOI: 10.1063/1.3095548 (cit. on p. 42).

[119] Z. C. Holman and U. R. Kortshagen: A flexible method for depositing dense nanocrystal thin films: Impaction of germanium nanocrystals. Nanotechnology **21**(33) (2010), 335302. DOI: 10.1088/0957-4484/21/33/335302 (cit. on p. 43).

[120] S. Weis, R. Körmer, M. P. M. Jank, M. Lemberger, M. Otto, H. Ryssel, W. Peukert, and L. Frey: Conduction mechanisms and environmental sensitivity of solution-processed silicon nanoparticle layers for thin-film transistors. Small (Weinheim an der Bergstrasse, Germany) **7**(20) (2011), 2853–2857. DOI: 10.1002/smll.201100703 (cit. on pp. 43, 57).

[121] M. S. Kang, A. Sahu, D. J. Norris, and C. D. Frisbie: Size-dependent electrical transport in CdSe nanocrystal thin films. Nano Letters **10**(9) (2010), 3727–3732. DOI: 10.1021/nl102356x (cit. on p. 43).

[122] R. D. Deegan, O. Bakajin, T. F. Dupont, G. Huber, S. R. Nagel, and T. A. Witten: Capillary flow as the cause of ring stains from dried liquid drops. Nature **389**(6653) (1997), 827–829. DOI: 10.1038/39827 (cit. on p. 43).

[123] S. S. Cohen: Contact resistance and methods for its determination. Thin Solid Films **104**(3-4) (1983), 361–379. DOI: 10.1016/0040-6090(83)90577-1 (cit. on p. 56).

[124] K.-H. Müller, G. Wei, B. Raguse, and J. Myers: Three-dimensional percolation effect on electrical conductivity in films of metal nanoparticles linked by organic molecules. Physical Review B **68**(15) (2003), 377. DOI: 10.1103/PhysRevB.68.155407 (cit. on p. 57).

[125] H. Fu, K. V. Reich, and B. I. Shklovskii: Hopping conductivity and insulator-metal transition in films of touching semiconductor nanocrystals. Physical Review B **93**(12) (2016). DOI: 10.1103/PhysRevB.93.125430 (cit. on p. 57).

[126] R. N. Pereira, S. Niesar, W. B. You, A. F. da Cunha, N. Erhard, A. R. Stegner, H. Wiggers, M.-G. Willinger, M. Stutzmann, and M. S. Brandt: Solution-Processed Networks of Silicon Nanocrystals: The Role of Internanocrystal Medium on Semiconducting Behavior. The Journal of Physical Chemistry C **115**(41) (2011), 20120–20127. DOI: 10.1021/jp205984m (cit. on p. 57).

[127] A. Rose: Space-Charge-Limited Currents in Solids. Physical Review **97**(6) (1955), 1538–1544. DOI: 10.1103/PhysRev.97.1538 (cit. on p. 57).

[128] M. A. Lampert: Simplified Theory of Space-Charge-Limited Currents in an Insulator with Traps. Physical Review **103**(6) (1956), 1648–1656. DOI: 10.1103/PhysRev.103.1648 (cit. on p. 57).

[129] N. F. Mott and R. W. Gurney: *Electronic Processes in Ionic Crystals*. 6. ed. Oxford: Clarendon Press, 1950 (cit. on p. 57).

[130] S. Furukawa, T. Kagawa, and N. Matsumoto: Estimation of localized state distribution profiles in undoped and doped a-Si: H by measuring space-charge-limited current. Solid State Communications **44**(6) (1982), 927–930. DOI: 10.1016/0038-1098(82)90306-4 (cit. on p. 57).

[131] D. S. Ginger and N. C. Greenham: Charge injection and transport in films of CdSe nanocrystals. Journal of Applied Physics **87**(3) (2000), 1361–1368. DOI: 10.1063/1.372021 (cit. on p. 58).

[132] H. Lepage, A. Kaminski-Cachopo, A. Poncet, and G. Le Carval: Simulation of Electronic Transport in Silicon Nanocrystal Solids. The Journal of Physical Chemistry C **116**(20) (2012), 10873–10880. DOI: 10.1021/jp301713v (cit. on p. 59).

[133] C. Delerue, G. Allan, and M. Lannoo: Theoretical aspects of the luminescence of porous silicon. Physical Review B **48**(15) (1993), 11024–11036. DOI: 10.1103/PhysRevB.48.11024 (cit. on p. 60).

[134] T. van Buuren, L. N. Dinh, L. L. Chase, W. J. Siekhaus, and L. J. Terminello: Changes in the Electronic Properties of Si Nanocrystals as a Function of Particle Size. Physical Review Letters **80**(17) (1998), 3803–3806. DOI: 10.1103/PhysRevLett.80.3803 (cit. on p. 61).

[135] Lannoo, Delerue, and Allan: Screening in Semiconductor Nanocrystallites and Its Consequences for Porous Silicon. Physical Review Letters **74**(17) (1995), 3415–3418. DOI: 10.1103/PhysRevLett.74.3415 (cit. on p. 61).

[136] Wang and Zunger: Dielectric constants of silicon quantum dots. Physical Review Letters **73**(7) (1994), 1039–1042. DOI: 10.1103/PhysRevLett.73.1039 (cit. on p. 61).

[137] P. Gibbon and G. Sutmann: Long-Range Interactions in Many-Particle Simulation. Quantum simulations of complex many-body systems: from theory to algorithms. Ed. by J. Grotendorst, D. Marx, and A. Muramatsu. NIC series. Jülich: NIC-Secretariat, 2002, 467–506 (cit. on p. 61).

[138] U. Wolf, V. I. Arkhipov, and H. Bässler: Current injection from a metal to a disordered hopping system. I. Monte Carlo simulation. Physical Review B **59**(11) (1999), 7507–7513. DOI: 10.1103/PhysRevB.59.7507 (cit. on p. 61).

[139] V. A. Markel: Introduction to the Maxwell Garnett approximation: Tutorial. Journal of the Optical Society of America. A, Optics, image science, and vision **33**(7) (2016), 1244–1256. DOI: 10.1364/JOSAA.33.001244 (cit. on pp. 61, 67).

[140] N. J. A. Sloane: Kepler's conjecture confirmed. Nature **395**(6701) (1998), 435–436. DOI: 10.1038/26609 (cit. on p. 68).

[141] J. G. Berryman: Random close packing of hard spheres and disks. Physical Review A **27**(2) (1983), 1053–1061. DOI: 10.1103/PhysRevA.27.1053 (cit. on p. 68).

[142] C. Powell, ed.: *NIST X-ray Photoelectron Spectroscopy Database XPS,Version 4.1, NIST Standard Reference Database 20*. Gaithersburg MD, 2000. DOI: 10.18434/T4T88K (cit. on pp. 68, 69).

[143] A. Cattani-Scholz, D. Pedone, M. Dubey, S. Neppl, B. Nickel, P. Feulner, J. Schwartz, G. Abstreiter, and M. Tornow: Organophosphonate-based PNA-functionalization of silicon nanowires for label-free DNA detection. ACS Nano **2**(8) (2008), 1653–1660. DOI: 10.1021/nn800136e (cit. on p. 73).

[144] S. H. Vosko, L. Wilk, and M. Nusair: Accurate spin-dependent electron liquid correlation energies for local spin density calculations: A critical analysis. Canadian Journal of Physics **58**(8) (1980), 1200–1211. DOI: 10.1139/p80-159 (cit. on p. 75).

[145] C. Lee, W. Yang, and R. G. Parr: Development of the Colle-Salvetti correlation-energy formula into a functional of the electron density. Physical Review B **37**(2) (1988), 785–789. DOI: 10.1103/PhysRevB.37.785 (cit. on p. 75).

[146] A. D. Becke: Density-functional exchange-energy approximation with correct asymptotic behavior. Physical Review A **38**(6) (1988), 3098–3100. DOI: 10.1103/PhysRevA.38.3098 (cit. on p. 75).

[147] S. M. Sze and K. K. Ng: *Physics of semiconductor devices*. 3rd ed. New Jersey: John Wiley & Sons, 2007 (cit. on pp. 78, 86).

[148] A. Pathak: *Structural and electronic properties of organophosphonate monolayers on alumina and silicon oxide*. 1. Auflage. Molekularelektronik. München: Verlag Dr. Hut, 2016 (cit. on pp. 86, 88).

[149] D. O. Hutchins, T. Weidner, J. Baio, B. Polishak, O. Acton, N. Cernetic, H. Ma, and A. K.-Y. Jen: Effects of self-assembled monolayer structural order, surface homogeneity and surface energy on pentacene morphology and thin film transistor device performance. Journal of Materials Chemistry C **1**(1) (2012), 101. DOI: 10.1039/c2tc00378c (cit. on p. 90).

[150] M. Novak, A. Ebel, T. Meyer-Friedrichsen, et al.: Low-Voltage p- and n-Type Organic Self-Assembled Monolayer Field Effect Transistors. Nano Letters **11**(1) (2011), 156–159. DOI: 10.1021/nl103200r (cit. on p. 90).

[151] S. Casalini, C. A. Bortolotti, F. Leonardi, and F. Biscarini: Self-assembled monolayers in organic electronics. Chemical Society Reviews **46**(1) (2017), 40–71. DOI: 10.1039/c6cs00509h (cit. on p. 90).

[152] N. Cernetic, T. Weidner, J. E. Baio, H. Lu, H. Ma, and A. K.-Y. Jen: Enhanced Performance of Self-Assembled Monolayer Field-Effect Transistors with Top-Contact Geometry through Molecular Tailoring, Heated Assembly, and Thermal Annealing. Advanced Functional Materials **25**(33) (2015), 5376–5383. DOI: 10.1002/adfm.201501263 (cit. on p. 90).

[153] Z. Zhou, Z. Zhao, Y. Yu, B. Ai, H. Mohwald, R. C. Chiechi, J. K. W. Yang, and G. Zhang: From 1D to 3D: Tunable Sub-10 nm Gaps in Large Area Devices. Advanced Materials **28**(15) (2016), 2956–2963. DOI: 10.1002/adma.201505929 (cit. on p. 92).

[154] B. L. Oliva-Chatelain, T. M. Ticich, and A. R. Barron: Doping silicon nanocrystals and quantum dots. Nanoscale **8**(4) (2016), 1733–1745. DOI: 10.1039/c5nr04978d (cit. on p. 92).

[155] M. Fujii, H. Sugimoto, and K. Imakita: All-inorganic colloidal silicon nanocrystals-surface modification by boron and phosphorus co-doping. Nanotechnology **27**(26) (2016), 262001. DOI: 10.1088/0957-4484/27/26/262001 (cit. on p. 92).

[156] K. Biswas and S. Kal: Etch characteristics of KOH, TMAH and dual doped TMAH for bulk micromachining of silicon. Microelectronics Journal **37**(6) (2006), 519–525. DOI: 10.1016/j.mejo.2005.07.012 (cit. on p. 94).

[157] J. Chen, L. Liu, Z. Li, Z. Tan, Q. Jiang, H. Fang, Y. Xu, and Y. Liu: Study of anisotropic etching of (1 0 0) Si with ultrasonic agitation. Sensors and Actuators A: Physical **96**(2-3) (2002), 152–156. DOI: 10.1016/S0924-4247(01)00786-5 (cit. on p. 94).

[158] A. Angı, M. Loch, R. Sinelnikov, J. G. C. Veinot, M. Becherer, P. Lugli, and B. Rieger: The influence of surface functionalization methods on the performance of silicon nanocrystal LEDs. Nanoscale **10**(22) (2018), 10337–10342. DOI: 10.1039/c7nr09525b (cit. on p. 95).

[159] A. Angı, R. Sinelnikov, H. H. Heenen, et al.: The influence of conjugated alkynyl(aryl) surface groups on the optical properties of silicon nanocrystals: Photoluminescence through in-gap states. Nanotechnology **29**(35) (2018), 355705. DOI: 10.1088/1361-6528/aac9ef (cit. on p. 95).

[160] M. A. Khan, U. S. Bhansali, D. Cha, and H. N. Alshareef: All-Polymer Bistable Resistive Memory Device Based on Nanoscale Phase-Separated PCBM-Ferroelectric Blends. Advanced Functional Materials **23**(17) (2013), 2145–2152. DOI: 10.1002/adfm.201202724 (cit. on p. 103).

[161] A. Turfanda: Transfer printing of metal contacts on organophosphonate self-assembled monolayers. Master thesis. Munich: Technical University of Munich, 2018 (cit. on p. 105).

[162] T. Haeberle: Metal transfer printing as an enabling technology for device fabrication. PhD thesis. Munich: Technical University of Munich, 2017 (cit. on p. 105).

List of publications

The following publications and conference contributions directly evolved from this work:

- S. Pfaehler, A. Angı, D. Chryssikos, A. Cattani-Scholz, B. Rieger, and M. Tornow: Space charge-limited current transport in thin films of alkyl-functionalized silicon nanocrystals. Nanotechnology **30**(39) (2019), 395201. DOI: 10.1088/1361-6528/ab2c28

- S. Pfaehler, A. Pathak, K.-C. Liao, J. Schwartz, and M. Tornow: Silicon Nanogap Electrode Engineering for Organic Monolayer Field Effect Transistors. 2019 IEEE 19th International Conference on Nanotechnology (IEEE-NANO) (Macao, China). IEEE, 2019, 521–525. DOI: 10.1109/NANO46743.2019.8993870

- S. Pfaehler, A. Angı, B. Rieger and M. Tornow: An all-silicon nanogap electrode platform for electronic transport studies of thin films of functionalized silicon nanocrystals. (Poster) 2018 E-MRS spring meeting (Strasbourg, France).

- S. Pfaehler, A. Angı, B. Rieger and M. Tornow: An all-silicon nanogap electrode platform for electronic transport studies of thin films of functionalized silicon nanocrystals. (Conference contribution) 2018 International Workshop (Technische Universität München) "Novel Concepts and Electronic Phenomena in Heterosystems" (Tutzing, Germany).

- S. Pfaehler, K. Keim, R. Csiki, Q. H. Nguyen, K.-C. Liao, M. Stutzmann, J. Schwartz, A. Cattani-Scholz, and M. Tornow: A nanogap electrode platform for organic monolayer-film devices. 2016 IEEE 16th International Conference on Nanotechnology (IEEE-NANO) (Sendai, Japan). IEEE, 2016, 842–844. DOI: 10.1109/NANO.2016.7751507

Acknowledgments

I am very thankful for all the great people I had the pleasure and privilege to work with during my PhD. First of all, I would like to thank my supervisor Prof. Dr. Marc Tornow for giving me the great opportunity to conduct my research work in his group. Thanks for all the support and guidance during the entire project.

Next I would like to thank all my colleagues from the molecular electronics group who made the daily life in the lab a pleasant time: Max Speckbacher, Hung Nguyen, Julian Dlugosch, Takuya Kamiyama, Domenikos Chryssikos, Daniel Reiser and Regina Hutschenreiter. Many thanks also to my former colleagues: Kai Saller, Anshuma Pathak, Achyut Bora and Arpita De.

A huge thank you to all who keep things going: Rosi Mittermeier, Katharina Blahetek, Lucia Weik and Susanne Maier.
A special thanks to my master students Kevin Keim and Aykut Turfanda.

I need to thank all current and former members from the Nanoelectronics group, especially Prof. Markus Becherer, Tobias Haeberle and Marius Loch for all the discussions and sharing their knowledge with me.

Many thanks to all my colleagues from ATUMS in Germany as well as in Canada. In particular many thanks to Prof. Frank Hegmann, Prof. Jillian Buriak and Prof. Jon Veinot for letting me visit their labs during my research stays at UofA in Canada. A huge thank you also to Mahmoud Almadhoun and Mary Narreto who helped me a lot at the UofA labs.

A special thank goes to Arzu Angı, who provided me with the SiNCs. Thanks for all the discussions, ideas and the fruitful collaboration.
A huge thanks also to Waldemar Kaiser and Prof. Alessio Gagliardi from the group of Simulation of Nanosystems for Energy Conversion. Waldemar conducted the kinetic Monte Carlo simulations for me.
I would like to thank all people from WSI and ZNN, especially Hubert Riedl, Peter Weiser and Claudia Paulus, without their help, daily lab work would have been way more difficult.

Finally, I would like to express my dearest thanks to my family and friends. Without their continuing support and friendship this work would not have been possible.